Ferroelectric and Piezoelectric Effects on the Optical Process in Advanced Materials and Devices

Yang Zhang, Wenjing Jie, Ping Chen, Weiwei Liu, and Jianhua Hao**

Prof. Y. Zhang, Prof. P. Chen, Prof. W. Liu
Institute of Modern Optics, Nankai University
Tianjin 300071, China
E-mail: yangzhang@nankai.ed.cn

Dr. W. Jie, Prof. J. Hao
Department of Applied Physics
The Hong Kong Polytechnic University
Kowloon, Hong Kong, P. R. China
E-mail: jh.hao@polyu.edu.hk

Dr. W. Jie
College of Chemistry and Materials Science
Sichuan Normal University
Chengdu 610068, China

Prof. J. Hao
The Hong Kong Polytechnic University Shenzhen Research Institute
Shenzhen 518057, China

Keywords: (ferroelectricity and piezoelectricity, lanthanide-doped phosphors, piezo-phototronics, 2D materials, PMN-PT actuators)

Abstract:

Piezoelectric and ferroelectric materials have shown great potential for control of the optical process in emerging materials. There are three ways for them to impact on the optical process in various materials. They can act as external perturbations, such as ferroelectric gating and piezoelectric strain, to tune the optical properties of the materials and devices. Second, ferroelectricity and piezoelectricity as innate attributes may exist in some optoelectronic materials, which can couple with other functional features (e.g., semiconductor transport, photoexcitation, photovoltaics) in the materials giving rise to unprecedented device

characteristics. The last way is artificially introducing optical functionalities into ferroelectric and piezoelectric materials and devices, which provides an opportunity for investigating the intriguing interplay between the parameters (e.g., electric field, temperature, strain) and the introduced optical properties. In this review, the tuning strategies, fundamental mechanisms, recent progress in ferroelectric and piezoelectric effects modulating the optical properties of a wide spectrum of materials, including lanthanide-doped phosphors, quantum dots, two-dimensional materials, wurtzite-type semiconductors, and hybrid perovskites are presented. Finally, the future outlook and challenges of this exciting field are suggested.

1. Introduction

The past decades have witnesses unprecedented advances in the fields of optoelectronics and photonics. Despite such tremendous progress, new materials and novel phenomena continue to drive innovation.Nelson, Dias, Bassett, Dunham, Verma, Miyake, Wiltzius, Rogers, Coleman, Li and Braun [1] Yet much work remains to be done to attain a comprehensive understanding and control of novel materials as well as novel phenomena observed in them. Dynamic manipulation of optical properties in emerging materials through external fields (e.g., electric field, strain, etc.) has stimulated considerable scientific activities, for elucidating the fundamental physics and/or triggering technological applications. In recent years, there is an increasing awareness of exploiting smart materials in control of or coupling with various optical and optoelectronic materials. Smart materials have the ability to respond to external stimuli, such as electric or magnetic fields, strain, temperature and moisture, in a controlled manner.[2, 3, 4] Piezoelectric and ferroelectric materials occupy an important position among the family of smart materials. Piezoelectric materials can produce electrical potential under mechanical stress. Conversely, they also response to applied electric fields with mechanical displacements. Ferroelectrics are a special class of piezoelectric materials, which have a spontaneous electric polarization that can be switched by an applied electric field. Piezoelectric and ferroelectric materials have shown enormous potential use for coupling with and control of electronic and optoelectronic properties of various materials, and have led to extremely fertile areas of research.[5, 6] There are three ways for ferroelectric and piezoelectric effects to impact on the optical processes in materials. They can act as external perturbations, such as ferroelectric gating and piezoelectric strain, to modulate the optical properties of

various materials, particularly low-dimensional materials. Second, ferroelectricity and piezoelectricity as innate attributes have been found in some optoelectronic materials, which can couple with other functional features (e.g., semiconductor transport, photoexcitation, photovoltaics) in the materials giving rise to unprecedented device characteristics.[7] The last way is artificially introducing optical functionalities into ferroelectric and piezoelectric materials, which provides an opportunity for investigating the intriguing interplay between the parameters (e.g., electric field, polarization, strain) and the introduced optical processes. Most noticeably of all, flexible and transparent optoelectronic devices are becoming increasingly important in wearable electronics, artificial intelligence, solar cells, transparent displays and so on.[8-10, 11] Emerging two-dimensional (2D) materials have played an important role in addressing the major challenges which flexible optoelectronics faces.[12, 13] Ferroelectric polarizations have been employed to modulate the transport properties of the 2D materials-based field-effect transistors (FETs).[14-16] On the whole, strain engineering can effectively tune the band structure of semiconductors, especially for low-dimensional materials due to the reduced dimensions of the materials are capable of sustaining much larger strain compared with their bulk counterparts. Strain tuning based on piezoelectric materials is particularly attractive, since piezoelectric materials can generate large linear forces under the application of an electric field. Besides, most utilized piezoelectric perovskites still possess piezoelectric tunability even at cryogenic temperature, which is helpful for the studies in quantum optics. Self-assembled semiconductor quantum dots (QDs) can be used as quantum light sources of single photons, indistinguishable photons, and entangled photons.[17] Electric-field-induced piezoelectric strain can modify the band structures of QDs in an *in-situ* and continuous manner, which has been successfully employed to erase the fine-structure splitting (FSS) of QDs.[18]

Ferroelectric and piezoelectric materials not just work as external factors. Materials that show ferroelectricity or piezoelectricity along with other characteristics lead to exciting research opportunities. For instance, the coupling effect between piezoelectricity and semiconductor properties in wurtzite-structured semiconductors, has given rise to the emerging fields of piezotronics and piezo-phototronics coined by Wang.[7] Progress in these fields undoubtedly enables developing new classes of electronics and optoelectronics with performances beyond expectation. On the other aspect of combining ferroelecricity and optoelectronics, photoferroelectricity defines a field that combines the photosensitive and ferroelectric phenomena. Giant photovoltaic effect observed in multiferroic $BiFeO_3$ (BFO) has triggered the revival of photoferroelectricity.[19] Ferroelectric photovoltaics are appealing for the

anomalous open-circuit voltage above-bandgap.[20] Beyond photovoltaics, other interesting photo-induced effects, such as photostriction effect and terahertz (THz) radiation are observed in BFO.[21, 22] Hence, much more phenomena can be expected to be observed in photo-induced effects from multiferroics. Recently, hybrid organic-inorganic perovskites (HOIPs) have received great attention along with the ever-increasing concern for solar energy. HOIPs are proceeding with an unprecedented trajectory. A certified efficiency more than 22% has been achieved in just a couple of years.[23] A possible ferroelectricity in hybrid perovskites might be relevant to the superb photovoltaic performance. However, it remains controversial whether hybrid perovskites exhibit ferroelectricity.[24, 25] Gaining a deeper understanding of the ferroelectric nature in hybrid perovskites is of significance for optimizing their performance in photovoltaics, as well as in other optoelectronic devices. There is also a prospect of coupling where inherent ferroelectricity interplays with artificially introduced functionality. For example, the light emission of lanthanide-doped ferroelectrics can be coupled with the ferroelectric polarization, which brings lots of research opportunities.[26] The study of ferroelectric and piezoelectric effects on optical properties is more than fundamental curiosity in materials. The potential coupling activities in the materials promise more freedom of designing optoelectronic and photonic devices, offering an improvement in performance and even new functions added. To the best of our knowledge, most of the recent review articles in regard to emerging materials mainly focus on their synthesis, characterizations and applications.[11, 27-30] Meanwhile, ferroelectric and piezoelectric materials as well as the related applications have been reviewed.[3-5, 31] There are also reviews associated with specific areas regarding piezo-phototronics,[7, 32] and ferroelectric photovoltaics.[33] However, there has been no a comprehensive overview of the ferroelectric and piezoelectric effects modulating the optical properties of advanced materials and devices. This Review article will focus on the ferroelectric and piezoelectric effects on the optical process of recently emerging materials (**Figure 1**). The fundamentals of piezoelectrics and ferroelectrics are briefly described first. After that, various emerging optical materials and devices will be discussed, including lanthanide ions-doped ferroelectrics, atomic-layered 2D materials, self-assembled semiconductor QDs, ferroelectric photovoltaics, and hybrid perovskites. The strategies of ferroelectric and piezoelectric control and coupling are presented in Section 4. Section 5 will highlight recent progress in this field. Finally, we will conclude with perspective.

2. Fundamentals of Piezoelectricity and Ferroelectricity

The fundamentals of piezoelectricity and ferroelectricity will be introduced prior to discussing the ferroelectric and piezoelectric effects on the optical process of functional materials.

2.1. Piezoelectricity

Piezoelectric materials can generate an electric potential under an applied strain. Or conversely, an electric field induces mechanical stress through the so-called converse piezoelectric effect. Piezoelectricity represents an intrinsic property arising from the non-centrosymmetric crystal structures. The direct piezoelectric effect determines a linear relationship between the polarization (P_i) and the strain (x_{ij}) or stress (σ_{ij}) with the Einstein notation[5]:

$$P_i = d_{ijk}\sigma_{jk} \quad (1)$$

$$P_i = e_{ijk}x_{jk} \quad (2)$$

where d_{ijk} and e_{ijk} are piezoelectric charge coefficients, respectively. Converse piezoelectric response modes are typically employed to tailor the properties of materials via piezoelectric-induced strain. The converse piezoelectric effect induces a mechanical deformation as follows in response to an applied electric field[5]:

$$x_{ij} = d_{kij}E_k \quad (3)$$

$$\sigma_{ij} = e_{kij}E_k \quad (4)$$

where E_k is the applied electric field. Nowadays, the most technologically important piezoelectric materials are the ceramics or single crystals with perovskite structure, such as Pb(Zr, Ti)O_3 (PZT) and $BaTiO_3$ (BTO). They can offer superior piezoelectric performance. PZT ceramics are the binary solid solutions of $PbZrO_3$ (PZO)and $PbTiO_3$ (PTO). The piezoelectric coefficients strongly depend on the chemical compositions, and generally achieve the largest values at the vicinity of the morphotropic phase boundary (MPB). The piezoelectric coefficients of PZT drastically increases near the MPB located at the composition with the Zr/Ti ratio of 53/47. During these years, single-crystal relaxor ferroelectric $Pb(Mg_{1/3}Nb_{2/3})O_3$-$PbTiO_3$ (PMN-PT) offers the largest currently available piezoelectric response and has been extensively utilized for strain engineering. The

piezoelectric coefficients d_{33} of PMN-PT can be up to ~2500 pC/N. Like PZT, the piezoelectric coefficients of PMN-PT are strongly enhanced at the MPB between the rhombohedral and tetragonal phases (**Figure 2**a).[34] The huge piezoelectric effect of PMN-PT can be ascribed to an electric-field induced phase transition from rhombohedral to tetragonal structure, as shown in Figure 2b.

Wurtzite-structured piezoelectric compounds represent another important class of piezoelectric materials. Both ZnO and AlN are wurtzite-structured piezoelectric compounds with small piezoelectric coefficients.[5] However, profound semiconductor and photonic characteristics enable them to be implemented in the electronic and photonic devices. Based on the coupling effect between piezoelectric polarization, semiconductor properties and optical excitation, two new fields of piezotronics and piezo-phototronics are created by Wang.[35, 36]

Piezoelectric thin-film structures are essential components for realizing integrated active microelectromechanical systems (MEMS). Various chemical or physical methods such as the sol-gel method,[37] chemical vapor deposition,[38] sputtering,[39] and pulsed laser deposition[40] have been employed to fabricate piezoelectric thin films.[41] Compared with polycrystalline thin films, epitaxial films are favored due to lower leakage current and better piezoelectric performance. Significant advances in integrating high-quality piezoelectric thin films (e.g., PZT and PMN-PT) with Si,[39, 42] can meet the requirements for chip-integrated active MEMS.

2.2. Ferroelectricity

Ferroelectric materials possess a spontaneous electric polarization that can be reversed by an applied electric field. Ferroelectric materials are an attractive class of essential components for various functional devices. Rapid advances in ferroelectric thin-film growth allow for extensive applications of ferroelectrics, including non-volatile memories,[43] tunnel junctions,[44] field-effect transistors (FET),[45] photovoltaics,[46] high dielectric and tunable microwave devices.[47] The most important ferroelectric materials share a perovskite structure (ABO_3). Ferroelectric materials have some unique characteristics, including spontaneous electric polarization, polarization reversal, and phase transition at Curie temperature T_c, where a cubic paraelectric state is evolved to a lower-symmetry ferroelectric state. BTO is often regarded as the prototypical ferroelectric (**Figure 3**a). Below 393 K, cubic BTO distorts to a ferroelectric tetragonal structure. Upon cooling to 278 K, it transforms to an orthorhombic structure. A further phase transition of BTO from orthorhombic to rhombohedral structure

occurs around 183 K (Figure 3b).[48] In ferroelectrics, the polarization vector can be switched under applied electric field. Ferroelectric crystals consist of domains, i.e., regions of aligned polarization vectors. Initially, a ferroelectric may exhibit zero macroscopic polarization due to randomly oriented domains. Figure 3c shows the hysteresis curves of polarization versus electric field (*P*-*E* loop) in ferroelectric materials. The polarization will reach the saturation regions with increasing the electric field. After poling, the remnant polarization P_r defines the value of the polarization after removing the electric field. At the coercive field E_c, the net polarization becomes zero, meaning that the volume fractions of the domains with opposite directions are equal. Along the electric field sweeps between the positive and negative directions, the hysteresis loop is formed.[49] Landau free energy curve as shown in Figure 3d indicates a bistable nature of the ferroelectric polarization, which lays the physical basis for non-volatile ferroelectric random access memory (FeRAM).

Ferroelectric materials are characterized by their asymmetry structures, which can response to variables including electric field, temperature and strain.[31] For example, epitaxial strain emerges when ferroelectric films are deposited on the substrates with lattice mismatch. In-plane strain can dramatically affect the polarization properties of the ferroelectric films.[4, 50] Besides strain, the electric field can also modulate the crystal structure. Taking tetragonal BTO as an example, the unit cell elongates along with the spontaneous polarization direction. An electric field along the direction of spontaneous polarization will further elongate the *c*-axis of the lattice, and the in-plane *a*-axis of the lattice will contract at the same time (Figure 3e).[51]

Besides inorganic materials, driven by the rapidly development of flexible electronics, organic ferroelectrics polyvinylidene fluoride (PVDF) and its copolymer with trifluoroethylene (TrFE) have attracted intensive research. The ferroelectricity in PVDF originates from molecular dipoles composed of positive hydrogen atoms and negative fluoride atoms. The low-temperature and solution processing fabrication of PVDF is highly desirable on numerous occasions. The applications of PVDF and its copolymer range from non-volatile FeRAM and ferroelectric field-effect transistor (FeFET) to photovoltaic cells and energy generators. Meanwhile, the groundbreaking work on graphene has revolutionized electronics and optoelectronics with its exceptional properties, and triggered intense research activities on 2D materials. The piezoelectricity has been experimentally observed in monolayer MoS_2.[52] Robust in-plane ferroelectricity was discovered in atomic-thick SnTe.[53] Very recently, out-of-plane piezoelectricity and ferroelectricity were discovered in van der Waals layered α-

In_2Se_3.[54] These novel findings have broaden ferroelectric horizons and led to exciting research opportunities in smart materials at nanoscale.

3. Advanced Materials and Devices for Optical Applications

In this section, we introduce several classes of advanced materials, which have been widely used for optoelectronic and photonic applications. Ferroelectric and piezoelectric effects can effectively affect the optical properties of these materials and associated devices.

3.1. Lanthanide-Doped Phosphors

Lanthanide-doped phosphors are generally composed of a host and activators. If the activators possess small absorption cross-sections, some kinds of sensitizers are co-doped, which can absorb the excitation energy and subsequently transfer the energy to the adjacent activators (**Figure 4**a). Lanthanide-doped phosphors have many advantages versus other luminescent materials (e.g., organic dyes, quantum dots), such as large Stokes shift, narrow emission spectra, high chemical stability and photostability, and low toxicity.[55] The luminescent properties of phosphors primarily depends on the activators. Meanwhile, the crystal field has an important influence on the luminescent properties of the phosphors. The most stable oxidation state of lanthanide ions are trivalent ions (Ln^{3+}). The 4*f* electrons of Ln^{3+} are shielded by the completed filled $5s^2$ and $5p^6$ orbitals, resulting in sharp and narrow emission spectra of Ln^{3+} ions. To date, the light emission of Ln^{3+}-doped phosphors have covered the spectra ranging from ultraviolet (UV) to infrared via downshifting and/or upconversion processes. The term upconversion refers to a nonlinear anti-Stokes optical process, which can convert NIR photons to UV or visible photons via multiple absorption or energy transfer. Upconversion has found its applications in diverse fields, such as lighting and display,[56] biomedical imaging,[57] biodetection,[58] solid-state laser[59] and solar cells.[60] Owing to the abundant energy levels, Ln^{3+} such as Er^{3+}, Tm^{3+}, Ho^{3+} and Pr^{3+} have been extensively studied as activators for upconversion phosphors.[61] The energy level diagrams of commonly used Ln^{3+} ions are shown in Figure 4b. However, the absorption cross-sections of most Ln^{3+} ions in near-infrared (NIR) region are relatively small. In order to improve the upconversion efficiency, Yb^{3+} ion is usually chosen as the sensitizer because of its sufficient absorption cross-section in the NIR region.[62] In addition, the sole $^2F_{7/2} \rightarrow {}^2F_{5/2}$ transition of Yb^{3+}

matches well with lots of transitions of other Ln^{3+}.[63] Figure 4c shows the energy transfer mechanisms in Er^{3+}, Tm^{3+} and Yb^{3+} co-doped systems under 980 nm laser excitation.

The host materials with varying degree of symmetry can exert different crystal fields on dopant Ln^{3+} ions.[55] The odd-parity components induced by the non-centrosymmetric lattice can perturb the parity (Laporte) forbidden, resulting in enhanced $4f$ transitions of Ln^{3+} ions. The size and valence of the host cations ought to be close to those of Ln^{3+} ions for reducing the lattice defects. Host materials with smaller phonon energy are preferred in order to inhibit the non-radiative relaxation. For instance, $NaYF_4$ with relatively small phonon energy (~ 350 cm^{-1}) has been the most used host material for Ln^{3+} ions.[27, 64] Oxide materials are another important class host materials due to their superior photo and chemical stability. Ferroelectric oxides such as BTO, PZT and $KNbO_3$ (KNO), have high dielectric constant, electro-optic and non-linear optical properties, and ferroelectric activity.[65] Alkaline earth ions (e.g., Sr^{2+}, Ca^{2+}, Ba^{2+}) and some transition metal ions (e.g., Zr^{4+}, Ti^{4+}) exhibit close ionic size to Ln^{3+} ions. The recent realization of Ln^{3+}-doped ferroelectric materials has unlocked a realm of possibilities for ferroelectric-optic multifunctional materials.[66]

The ability to tune the luminescent properties of the phosphors is very useful for their applications in optoelectronic devices.[67, 68] As noted, lanthanide-doped phosphors comprise dopant ions and a crystalline host. A straightforward approach is to change the concentration and combination of the dopant ions.[69] Liu's group has demonstrated that the emitted color of the Er^{3+}, Tm^{3+} and Yb^{3+} tri-doped phosphors can be subtly tuned from visible to NIR by fine modulating the combinations of dopant ions.[70] Meanwhile, the luminescent properties can be rendered by tailoring the local crystal field through varying the hosts. For instance, the upconversion efficiency of $NaYF_4$:Yb/Er nanocrystals with hexagonal symmetry is much higher compared with the their cubic counterparts.[71] Surface modification or surface passivation is mainly used for manipulating luminescence of nanoscale phosphors. Through introducing an inert shell around each nanocrystal, the core-shell structure strongly enhances the light emission of $NaYF_4$:Yb/Er nanocrystals.[72] The inert shell can decrease the surface defects and ligands and thus suppress the associated non-radiative decays. Significant advances in synthetic methods towards more complicate core-shell nanostructures give rise to new opportunities for emission modulation. Capobianco *et al.* have proposed an active-core/active-shell nanostructure and gained more intense upconversion luminescence.[73] Liu and coworkers reported that tunable upconversion emissions can be achieved through a sublattice-induced energy migration-mediated upconversion (EMU) effect.[74] Plasmonic nanostructures made of noble metals can control light within nanoscale confined region and

provide strongly enhanced electromagnetic (EM) fields in their vicinity. Plasmonic enhanced upconversion emissions have been found in a series of Ln^{3+}-doped nanocrystals.[75] It should be pointed out that all the aforementioned methods require irreversible and *ex-situ* treatments, which are unfavorable to observe the host symmetry-associated dynamic processes. Furthermore, inhomogeneities and defects introduced during the synthesis will interfere the investigation of the pure crystal field effect on the luminescent properties. Therefore, the *in-situ* and real-time tuning methods should be particularly appealing not only in academic sense, but also for technological purpose. Compared with chemical methods, physical approaches, including using electric and magnetic fields, strain, and ionizing radiations, can realize flexible tuning the luminescence of lanthanide-doped phosphors.[65, 68, 76] The lattice symmetry of ferroelectrics can be modified by various physical stimuli, including electric field, mechanical strain, and temperature. Thus, lanthanide-doped ferroelectrics promise a platform to investigate the structure symmetry related luminescent processes.[26, 77, 78]

3.2. 2D Materials

Ever since the discovery of graphene in 2004,[79] 2D materials, including graphene, transition metal dichalcogenides (TMDs) and other 2D semiconductors have attracted much attention from communities of physics, chemistry, materials, biology, and many multidiscipline fields. 2D materials possess fascinating electrical, optical and mechanical features,[80] and exhibit great potential applications in future electronic and optoelectronic devices from both scientific and technological viewpoints.[81] 2D materials could be incorporated with versatile functional materials, including ferroelectric and piezoelectric materials.

3.2.1. Graphene

Graphene consists of a single layer of sp^2 hybridized carbon atoms arranged like a honeycomb lattice. The unique lattice of graphene can be decomposed into two triangular Bravais sublattices, the A and B sublattices. The associated band structure is characterized by two energy bands intersecting at the two inequivalent corners (K and K′ reciprocal points) in the Brillouin zone. The linear dispersion relation indicates that carriers in graphene are Dirac fermions. The carrier mobilities of graphene are found to be up to 10^6 cm^2 $V^{-1}s^{-1}$.[82] Graphene also shows remarkable optical properties. Monolayer graphene exhibits a linear absorbance of ~ 2.3% in the visible range. Only a negligible fraction (< 0.1%) of the incident

light is reflected by monolayer graphene.[83] Therefore, graphene exhibits a high transparency over a broad spectrum. Taking advantage of low sheet resistance R_s, graphene is regarded as a candidate for transparent conductors in photovoltaic devices,[84] light-emitting diodes (LEDs),[85] and touch screens.[86] On the other hand, graphene can absorb ~2.3% of incident light across a broadband spectrum despite being only a single atomic layer thick (~0.33 nm). An effective absorption coefficient of single layer graphene can be calculated to be ~ 7×10^5 cm^{-1}.[87] Such a large absorption coefficient indicates strong light-matter interactions occurring in graphene, which suggests that great potential applications of graphene in photodetectors[88] and optical modulators.[89]

3.2.2. 2D Materials beyond Graphene

Beyond graphene, a large number of graphene-like 2D materials with a weak van der Waals (vdW) interlayer interaction have been discovered and formed a big 2D family.[29] TMDs typically with a MX_2 (M = Mo, W; X = S, Se) stoichiometry, occupy an important role in the 2D family. As a representative of TMDs, molybdenum disulfide (MoS_2) exhibits intriguing optical properties thanks to the existence of a tunable and also suitable bandgap.[8] Bulk MoS_2 has an indirect bandgap of 1.2 eV. When the thickness of MoS_2 decreases down to monolayer, it becomes a semiconductor with a direct bandgap of 1.8 eV.[90] Exfoliated MoS_2 was ever transferred onto SiO_2 and HfO_2 to fabricate high-performance FETs.[91] Additionally, MoS_2 has been conjugated with $MoTe_2$ to form a heterojunction for photovoltaic applications.[92] Besides TMDs, 2D III-VI semiconductors, InX and GaX (X = S, Se and Te), have shown large and tunable optical bandgaps, dramatic nonlinear photonic effect and strong photoresponse, making them potentially useful for optoelectronic devices.[93] For example, 2D GaSe crystals have drawn attention due to their unique structure without a centrosymmetric center in a single layer and promising applications in nonlinear optical properties.[94] In the unit layer of GaSe, the atoms are stacked by the strong covalent bonded interaction in the sequence of Se–Ga–Ga–Se.[95] Such new reported materials with a suitable bandgap of 2.1 eV have been developed towards to Si-integrated FETs and photodetectors.[96] Black phosphorus (BP) attracts substantial research interest due to its widely tunable bandgap from monolayer about 2.3 eV to bulk 0.3 eV.[28] Single-layer BP, namely phosphorene, exhibits strong light-matter interactions and excellent electronic transport properties.[97] In contrast to the semi-metallic graphene, phosphorene is a semiconductor with a non-vanishing direct bandgap.

Meanwhile, the optical conductivities of 2D BP are strongly associated with the number of layers, which is highly preferred for semiconducting photonic devices.[98]

3.3. Semiconductor Quantum Dots

III-V semiconductor QDs (e.g., GaAs, InGaAs) are proven excellent quantum emitters, which can generate single photons, indistinguishable photons, and entangle photon pairs. Unlike other quantum light sources based on spontaneous parametric down-conversion (SPDC) and four-wave mixing (FWM) processes, QDs can be triggered by both optical and electrical pulse.[18] Self-assembled QDs can be obtained through the Stranski-Krastanow (SK) method. Some fluctuations of the properties in each individual QD are produced during the growth process. As a result, the post-growth treatment is indispensable to meet the stringent requirements for quantum photonics, particularly where independent QDs are involved.[99] For instance, the exchange interaction of QDs gives rise to the exciton eigenstates being linearly polarized with an energy difference defined as the fine-structure splitting (FSS). In order to efficiently produce entangled photon pairs, precise control of the FSS between the bright excitonic states is necessary. Some strategies including post annealing, applying magnetic,[100] electric,[101, 102] and strain fields[103] have been utilized to eliminate the FSS of QDs. Among them, vertical electric fields via the so called "giant Stark effect" (GSE) is regarded as an effective and versatile tuning knob for eliminating the FSS.[101] However, it is impossible for the electrical stimulation to pump the QDs and trigger the GSE simultaneously. Hence, some other "tuning knobs" are still desirable for more freedom of device design. Mechanical stress has demonstrated the feasibility of controlling the FSS as well as the emission energy of QDs. Elastic stress fields based on piezoelectric elements as alternative manners have gained increasing interest. Seidl *et al.* firstly introduced quasi-uniaxial stress based on PZT actuators to reduce the FSS of InGaAs/GaAs QDs.[104] Then, Schmidt *et al.* utilized single-crystal PMN-PT to replace PZT ceramics as the piezoelectric actuators. Nanomembranes containing self-assembled QDs were transferred onto the PMN-PT actuators. Thanks to the exceptional piezoelectric coefficients of PMN-PT, a broader adjusting range for both FSS and photon energy has been acquired.[105]

Silicon photonics is an emerging technology integrating active or passive photonic and electronic components on a single silicon-based chip. Silicon photonics technology is in the ascendant in recent years. Semiconductor QDs integrated with PMN-PT actuators are proven to be an effective electrical-controllable nonclassical light source. The realization of

integrating this hybrid quantum photonic component with a silicon platform offers great potential for chip-integrated quantum computing and communication devices. In the past few years, there have been several demonstrations of integrating the hybrid strain-tunable quantum light sources with silicon components, which promise possibilities in both fundamental research and real applications.[106, 107]

3.4. Photoferroelectric Oxides

The term photoferroelectric refers to materials that combine the photoelectric response and ferroelectric properties of materials. In recent years, photoferroelectric research focuses on the ferroelectric photovoltaics. For p-n junction solar cells, the magnitude of open-circuit voltage depends on the quasi-Fermi energy difference of the photogenerated carriers.[46] As a result, the open-circuit voltage can not exceed the bandgap of the absorber material. Unlike conventional solar cells, under illumination, the open-circuit voltage of ferroelectric photovoltaics can be many orders of magnitude higher than the bandgap of the ferroelectric materials.[108] Unfortunately, the short-circuit current of ferroelectric photovoltaics is extremely low. Overall, ferroelectric materials show ultralow power conversion efficiency (PCE). Therefore, ferroelectric photovoltaics have remained bleak for decades.[109] Until recent years, there is a renaissance of ferroelectric photovoltaics since a giant photovoltaic effect was observed in multiferroic $BiFeO_3$ (BFO) thin films.[19] The above bandgap open-circuit voltage is a prominent feature of ferroelectric photovoltaics, unambiguously indicating a fundamentally different mechanism for ferroelectric photovoltaics. The actual mechanism underlying anomalous photovoltaic effect of ferroelectric is somewhat mystifying to scientists. Photovoltaic effect is ubiquitous in ferroelectric materials, which is associated with many factors, such as remnant polarizations, crystal symmetry, defects and impurities, and ferroelectric/electrode interface. Theory and experiment show that the bulk photovoltaic effect is responsible for the anomalous photovoltaic effect observed in ferroelectric materials. Meanwhile, some parameters such as domain walls, depolarization field, Schottky barrier junction, and defects can effectively render the performance of ferroelectric photovoltaics.[33] The ballistic and shift mechanisms have been proposed to explain the bulk photovoltaic effect.[110] In the ballistic mechanism, the photo-excited non-thermalized carriers in a non-centrosymmetric crystal have an asymmetric momentum distribution, which results in a net current.[111] The shift mechanism ascribes the transfer of photogenerated charges to the quantum mechanical process arising from the asymmetry of the quantum wave packets.[112]

The past few years have witnessed some process on ferroelectric photovoltaics. Most ferroelectric oxides, such as BTO and PZT, have wide bandgaps (~3.3 eV) corresponding to the spectrum in the UV region. Therefore, only a small fraction of the solar energy can be absorbed and put to use. Recently, the bandgap of ferroelectric materials has been artificially engineered to improve the conversion efficiency. A tunable bandgap from 1.1 to 3.8 eV has been realized in ferroelectric $[KNbO_3]_{1-x}[BaNi_{1/2}Nb_{1/2}O_{3-\delta}]_x$ (KBNNO) solid solutions.[113] The bandgap of multiferroic Bi_2FeCrO_6 (BFCO) was tuned down to 1.43 eV. A multi-absorber system based on BFCO has gained a high efficiency of up to 8.1%.[114] Apart from bandgaps, Schottky barriers formed at the ferroelectric/electrode interfaces can also influence the performance of ferroelectric solar cells. Both n-type Cu_2O cathode and amorphous silicon (a-Si) were used to improve the conductivity of PZT based cells.[115, 116] Considerable effort has been devoted to ferroelectric photovoltaics from microscopic view. The improved PCE of BFO thin films was found to be associated with domain walls,[19] which aroused great interest on photoferroelectrics as well as on domain wall electronics.[33]

Currently, multiferroic BFO is the most studied photoferroelectric material, in which the ferroelectric, ferromagnetic and ferroelastic orders interact with each other.[117] The coupling between three ferroic orders promises greater design freedom of photoferroelectric devices, not just limited in photovoltaics. When subjected to light, BFO has demonstrated many exotic phenomena, such as femtosecond laser induced THz radiation,[22] and photostriction responses.[21] Therefore, the efforts to investigate the photo-induced effects in ferroelectrics or multiferroics, may endow future electronic and optoelectronic devices with more new functionalities.

3.5 HOIPs

Solar photovoltaic cells can directly convert sunlight into electricity. They are perhaps the most common form of clean and renewable energy. To date, about 90% of current solar panels are based on crystalline silicon. However, the high cost of silicon solar cells with respect to fossil fuels still limits the further development. Therefore, great attention has already turned toward a number of emerging photovoltaic concepts, including organic photovoltaics, copper indium gallium selenide (CIGS), perovskite cells, and quantum-dot photovoltaics.[30, 118] These cutting-edge photovoltaic technologies bring benefits of low-cost, flexibility, easy fabrication, and even better performance. Among them, HOIPs have brought revolutionary impacts on photovoltaic community. Hybrid perovskite photovoltaic cells are

cheap and easy to assemble. Hybrid perovskite solar cell made its debut with only a PCE of 3.8% in 2009.[119] By 2016, the efficiency has been pushed to a certified value of 22.1%.[23] This unprecedented trajectory has urged worldwide pursuit for new efficiency records. HOIPs have a similar perovskite structure (ABX_3) as their oxide counterparts, with the oxygen anions replaced by a halide ion ($X = I^-$, Br^-, and Cl^-). In halide perovskites of present interest, the larger cation A is an organic molecular, generally methylammonium ($CH_3NH_3^+$ or MA) or formamidinium ($(NH_2)_2CH^+$ or FA), and cation B is usually Pb atoms. Perovskites formed with other divalent atoms (e.g. Sn) exhibit lower bandgaps, but generally lower stability.[120] HOIPs have ideal electric and optical characteristics for photovoltaics and other optoelectronics, including favorable direct bandgap, strong solar absorption, long carrier diffusion lengths, and modest carrier mobilities, etc.[121] Furthermore, the simple and solution-processed fabrication makes them appealing for developing low-cost and large-area device applications. Methylammonium lead iodide ($CH_3NH_3PbI_3$ or $MAPbI_3$) as an archetypal hybrid perovskite, possesses a strong absorption coefficient in the solar spectrum, allowing for reducing the required thickness of perovskite absorbers. Thinner perovskite layers are beneficial to collecting the photogenerated charge carriers. The absorption coefficient of $MAPbI_3$ (~ 10^5 cm^{-1}) is among the most efficient photovoltaic absorbers, which is attributed to its direct bandgap and the strong spin-orbit coupling effect. At room temperature, $MAPbI_3$ exhibits an experimental optical gap of ~1.6 eV, approaching the ideal 1.4 eV.[122] The exciton banding energy (E_B) is defined as the energy required to dissociate excitons into free charge carriers. In order to improve the PCE, a small E_B is preferred for efficient charge carrier separation. Recently, the E_B value of $MAPbI_3$ has been determined to be around 16 meV through the high-field magneto-absorption method at low temperature. Experiments also show that the E_B will falls to only a few meV in the room temperature.[123] As a result of such low E_B values, $MAPbI_3$ is regarded as a non-excitonic material. The valence band of $MAPbI_3$ is dominated by I 5*p* states, mixed with part contribution from Pb 6*s* states. While, the conduction band is mainly composed of Pb 6*p* states. A strong spin-orbit coupling is induced by the heavy atoms in $MAPbI_3$, which cause the conduction band to fall by about 1 eV.[124] The spin-orbit coupling effect also leads to a reduction of the effective masses of the carriers, which partially accounts for the high mobility and long diffusion lengths of the carriers propagating in halide perovskites. Mobilities of $MAPbI_3$ single crystals can be up to 105 cm^2 V^{-1} s^{-1}.[125] And an estimate mobility of 115 cm^2 V^{-1} s^{-1} has been reported in single-crystal $MAPbBr_3$.[126] The carrier diffusion length of $MAPbI_3$ polycrystalline films was found to be around 1 μm.[127] Under 1 sun illumination, the diffusion lengths for both electrons and holes

in single-crystal $MAPbI_3$ reach a length of more than 175 μm. [125] The long diffusion lengths help to increase the collection probability of photogenerated carriers.

From a scientific perspective, it is intriguing to ponder the reasons behind the superb photovoltaic performance in hybrid perovskites. There are also some puzzled photovoltaic phenomena observed in perovskites. One is the anomalous hysteresis behavior in the current-voltage curves.[128] Moreover, both photovoltages and photocurrents of the devices can be inverted by changing the polarity of $MAPbI_3$ films.[129] There are two possible reasons for understanding the unusual phenomena, namely ferroelectricity and ion migration. Many evidences support that ion migration mechanism being responsible for the hysteresis and switching characteristics, as a consequence of redistribution of ionic species.[130] While, the prospect of ferroelectricity in hybrid perovskites is adored by many researchers.[131] It is postulated that ferroelectricity exists in hybrid perovskites, which assists charge carriers separation, suppresses charge carriers recombination and facilitates charge carriers extraction. Furthermore, ferroelectric domains observed in halide perovskites were found to promote charge separation.[132] Nevertheless, there is still no consensus as to the ferroelectricity of halide perovskites. Theoretical predictions have suggested that the ferroelectricity of halide perovskites originates from the dynamics of the polar organic cations in the lattice.[132, 133] Several experimental groups have claimed that they observed ferroelectric domain in $MAPbI_3$ using piezoresponse force microscopy (PFM).[134, 135] However, credible hallmarks of ferroelectricity, such as appreciable stable remnant polarization and reliable polarization-electric field (*P*-*E*) loops are still not observed in $MAPbI_3$ at room temperature. Very recently, Rakita *et al.* have proved that single-crystal tetragonal $MAPbI_3$ at 204 K ferroelectric.[25] Although there has been some experimental evidences endorsing ferroelectricity in the perovskites, arguments against ferroelectricity are proposed in other studies.[24] Therefore, the existence of ferroelectricity of halide perovskites remains an open question, needed to be clarified.

To date, studies and applications regarding HOIPs have been not limited in photovoltaics. The exceptional attributes of HOIPs, such as long diffusion lengths, tunable absorption range, low defect density and high PL quantum yield, have enabled them to find broad applications in other optoelectronic devices, including photodetectors and light-emitting devices.[136, 137] The advantages of perovskites to achieve high efficiency in solar cell, in principle are also favorable for their application in photodetectors. High performance photodetectors for visible light range made from solution-processed hybrid perovskites have been reported.[138, 139] Owing to the heavy Pb and Br atoms, halide perovskites have large absorption cross-sections

for X-rays. The recently reported X-ray detectors made from solution-processes hybrid perovskites have shown very high sensitivity.[137, 140] The requirements for materials used in light-emitting devices are different from solar cells and photodetectors. Some remarkable features of HOIPs, such as impressive charge-transport properties, low trap density and high PL quantum yield ensure the feasibility of HOIPs-based light-emitting applications.[141]

4. Strategies of Ferroelectric and Piezoelectric Control/Coupling

In this section, we will present some strategies of ferroelectric and piezoelectric effects impacting on the optical properties of functional materials and devices.

4.1. Strain Engineering based on Piezoelectric Actuators

Strain engineering based on piezoelectric actuators has been utilized to modulate the physical properties of various materials, such as ferromagnets, superconductors, quantum dots and 2D semiconductor materials.[103, 142, 143] As mentioned above, single-crystal relaxor ferroelectric PMN-PT, endowed with giant piezoelectric strain and with piezoelectric tunability at cryogenic temperatures, has advanced to the forefront of strain engineering.[144] The (001)-oriented PMN-PT single crystal is generally cut into rectangular plates with thicknesses between 200 to 500 μm. Before use, the PMN-PT should be polarized with a large poling electric field along the (001) direction. If applying an electric field on the PMN-PT in the poling direction (also the thickness direction), the lattice of the PMN-PT will elongate along the direction of the electric field, resulting in an isotropic biaxial strain perpendicular to the electric field.

In order to obtain larger substrate-induced strain, both thin-film growth and layer material transfer should be meticulously processed to form good coherency between the thin-film or 2D material with the PMN-PT substrate. The integration of grapheme-like 2D atomic-thick crystals onto a PMN-PT actuator always involves the interaction with the supporting substrate by vdW forces. 2D-layered materials including graphene and TMDs can be transferred onto the PMN-PT via mechanical exfoliation, or traditional wet transfer method for large-area 2D crystals grown by chemical vapor deposition (CVD).[143] GaAs nanomembranes containing self-assembled QDs are bonded onto PMN-PT substrate by gold thermo-compression method.[18]

Single-crystal PMN-PT has a good lattice match with conventional dielectrics, such as $SrTiO_3$ (STO), BTO, and BFO. Some most utilized conductive oxides, including $SrRuO_3$ (SRO), $La_xSr_{1-x}MnO_3$ (LSMO) and $La_xCa_{1-x}MnO_3$ (LCMO), also have small lattice mismatch with PMN-PT. Therefore, PMN-PT is an ideal piezoelectric substrate for epitaxial oxide heterostructures. MEMS incorporating piezoelectric thin films can obtain large strain with a small voltage.[34] The past few years have witnessed significant advances in the growth of high-quality piezoelectric thin films, as well as in their integration into MEMS.[39] The breakthroughs of integration of epitaxial PMN-PT films with Si platform enable the realization of monolithic MEMS devices with dramatically reduced operation voltages and dimensions.

4.2. Methods based on Piezo-Phototronics

Wurtzite-structured semiconductors, such as ZnO, GaN and InN exhibit a non-central symmetry. A piezoelectric potential can be produced in the crystal when the crystal suffers a mechanical strain. The coupling between piezoelectric polarization and electronic transport in piezoelectric semiconductors gives rise to piezotronics, in which the piezopotential generated in the crystal can serve as a "gate" to modulate the charge carrier transport behavior at the interface or junction.[145] The piezotronic effect has been extensively used in the fields of nanoelectronics, optoelectronics, sensors, logic devices, and energy harvesting.[7, 35] The piezoelectric polarization can also effectively modulate the optoelectronic process. The three-way coupling among piezoelectricity, photonic excitation and semiconductor properties is referred to as the piezo-phototronic effect (**Figure 5**a). The piezo-phototronic effect can effectively improve the performance of light-emitting devices, photodetectors and photovoltaics.[146-148] Wurtzite-type semiconductors in the form of one-dimensional (1D) nanowire are ideal materials for piezotronics and piezo-phototronics due to their intriguing characteristics. 1D nanowires can sustain large mechanical deformation and are almost fatigue free under cyclic stretches. In addition, 1D piezoelectric nanowires are extremely sensitive to small mechanical disturbances.[32] Currently, ZnO nanowire is the first choice for both piezotronics and piezo-phototronics devices. As shown in Figure 5b, the Zn^{2+} cations and O^{2-} anions are tetrahedrally coordinated in the wurtzite-structured ZnO. The centers of positive and negative ions coincide with each other in the absence of stress. A stress along with the *c*-axis direction can cause the lattice distortion. The relative shift of the charge centers gives rise to an electronic dipole moment. The piezoelectric potential can be regarded as the sum of all

aligned dipole moments in the crystal upon straining as shown in Figure 5c. The presence of the piezopotential has great influence on optical processes, such as the generation, separation, diffusion and recombination of charge carriers in various optoelectronic devices. Therefore, the piezopotential is referred to as the fundamental concept of the piezo-phototronic effect.[149] Many optoelectronic applications can be enabled or enhanced by the use of the piezo-phototronic effect. Here, we attempt to introduce the effect by discussing the piezo-phototronic effect impacting optical processes of the photodetectors made from piezoelectric semiconductors.[150] Photodetectors are used to measure photon flux or illumination power by converting the collected light energy into electrical signal. The working principle of photodetectors is associated with the generation of electron-hole pairs, separation and collection of charge carriers by either a Schottky barrier or a p-n junction.[151] For the photodetectors based on Schottky contact, the Schottky barrier formed at metal-semiconductor junctions is crucial for the detection sensitivity. If there is no strain, the Schottky barrier height depends on the difference between the work function of the metal and the electron affinity of the semiconductor. When a piezoelectric semiconductor (such as ZnO) is under strain, the electric charges accumulate at the metal-semiconductor interface manipulate the local Schottky barrier height. Under a compressive strain, negative electric charges created at the interface give rise to a negative piezopotential, which will increase the Schottky barrier height. A higher Schottky barrier can separate, transport and collect the photogenerated electrons and holes more effectively (Figure 5d). Conversely, a positive piezopotential is introduced under a tensile strain, which reduces the Schottky barrier height (Figure 5e). A lower Schottky barrier means a smaller separating force for the photogenerated carriers. Thus, the sign and magnitude of the applied strain can regulate the sensitivity of the photodetectors via the piezo-phototronic effect.[152] As to photodetectors containing p-n junction, light absorbed in the depletion region creates electron-hole pairs, which are swept from the junction by the built-in electric field. Similar to modifying the height of the Schottky barrier by the piezopotential, the width of the depletion region also can be modulated by external strain.[153] Under a compressive strain, negative electric charges will aggregate at the interface of the n-type semiconductor side. Therefore, electrons in the n-type semiconductor are repelled from the interface. As a result, the depletion region will move to the n-type semiconductor side, corresponding to a smaller effective series resistance for charge injection to the contact (Figure 5f). Conversely, positive electric charges upon tensile straining will drag the depletion region towards to the p-type semiconductor side, resulting in an increased effective series resistance.[7] Moreover, the negative charges create a bump in the local band

near the interface, which can suppress the electron-hole recombination and promote photogenerated carriers separation processes. In contrast, positive electric charges induce a dip formed in the band structure, which also restrains the separation of the photogenerated electron-hole pairs (Figure 5g).[152] Therefore, external strain can effectively modulate the performance of the photodetectors made of piezoelectric semiconductors via the piezo-phototronic effect.

4.3. Ferroelectric Host Coupling

In inorganic lanthanide-doped phosphors, the optical properties are determined by the deliberately doped lanthanide ions, as well as the surrounding crystal structure. Selection of appropriate host materials is essential to endow lanthanide-doped phosphors with desirable luminescent spectra and enhanced light emission.[27] The variation of the host symmetry can modulate the light emission from the lanthanide-doped phosphors. According to Laporte's parity selection rule of electrical dipole (ED) radiation, *f-f* ED transitions of free Ln^{3+} ions are not allowed. Once the Ln^{3+} ions are embedded in a non-centrosymmetric host lattice, the mixing of odd-parity configurations from the host crystal-field somewhat relaxes the selection rules. Therefore, a lower-symmetry host in principle can exert more uneven parity into the 4*f* electronic wavefunctions, giving rise to the ED transitions of Ln^{3+} ions with a higher probability. The Judd-Ofelt (J-O) theory is devoted to the theoretical prediction of the spectroscopic properties of Ln^{3+} ions,[154] in which the spontaneous emission probability A_{ed} for an ED transition between the initial J manifold $|[S,L]J\rangle$ and the final J manifold $|[S',L']J'\rangle$ is determined by

$$A_{ed} = \frac{64\pi^4 e^2}{3h(2J+1)\lambda^3}\left[\frac{n(n^2+2)^2}{9}\right] S_{ed} \qquad (5)$$

where e is the electron charge, λ is the mean wavelength of the transition, n is the refractive index and h is plank constant. The ED line strength S_{ed}:

$$S_{ed} = \sum_{t=2,4,6} \Omega_t \left|\langle 4f^n[S,L]J \left\| U^{(t)} \right\| 4f^n[S',L']J' \rangle\right|^2 \qquad (6)$$

where $\langle\|U^{(t)}\|\rangle$ are reduced matrix elements of the unit tensor operators, and Ω_t (t=2,4,6) are the J-O intensity parameters, containing the parity perturbations of the crystal-field effect. There are some ED transitions of the lanthanide ions that are peculiarly sensitive to changes in

the surrounding enviroment. It was concluded that the inhomogeneity of the surrounding dielectric contributes to the so-called hypersensitive transitions.[155] Among three J-O parameters, the Ω_2 term is closely associated with the hypersensitive transitions. The magnitude of Ω_2 term is found to have a positive correlation with the asymmetry of the host lattice.[156]

The most straightforward method to vary the host symmetry is to change the host material, nevertheless, it is an *ex-situ* and irreversible manner. Host materials made from ferroelectrics are able to respond to external physical stimuli. Under an electric field, charged ions of ferroelectric materials suffer asymmetry displacement and result in a small distortion in crystal dimension. To describe the ferroelectric host coupling with the doped lanthanide ions, a system of Er^{3+} ions doped BTO is used as an example to investigate the electric-field-induced modification on the luminescence of Er^{3+} ions. Since its discovery, BTO is considered as the prototype of perovskite ferroeletrics. At room temperature, BTO belongs to a tetragonal structure, where the unit cell is elongated along the *c*-axis. It is found that Er^{3+} ion can replace Ba^{2+} or Ti^{4+} ion depending on the local Ba/Ti ratio in BTO. If Er^{3+} ion substitutes Ti^{4+} ion, Er^{3+} ion is located at the B-site and octahedrally coordinated by oxygen ions. Under an electric field, Ti^{4+} ions move along the direction of the electric field, while the O^{2-} ions are shifted against the electric field. The BTO lattices undergo electric-field-induced asymmetric structural transformation. The distortion of the host symmetry is propotional to the applied electric field, which gives rise to the modulation on the optical properties of Er^{3+} ions.

4.4. Ferroelectric Gating

As an interfacial phenomenon, electrostatic gating is particularly appealing to alter the electronic properties of 2D materials. In 2D materials-based FETs, all electrons propagate through atomically thin semiconductor channels, making it possible to uniformly gate over all electrons. Therefore, the current passing through 2D semiconductor channels can be effectively controlled by a gate voltage. Compared with conventional electrostatic gating, ferroelectric thin film is employed as a gate providing several distinct advantages. Ferroelectric gating is featured with electrically switchable non-volatile polarization states, which are employed to modify the density and type of mobile carriers in the 2D semiconductor channels.[157] Furthermore, the width of polarization domain walls in ferroelectric oxides can be down to several nanometers, enabling tuning the physical properties of 2D materials with nanoscale resolution.[158, 159] Dielectrics of traditional gate

materials, such as SiO_2, HfO_2 and Al_2O_3 exhibit a linear relationship with the electric field.[79] While, dielectric properties of ferroelectric materials show a nonlinear and hysteretic response to the electric field. In addition, ferroelectric materials exhibit ultrahigh dielectric constants. The usually used ferroelectric oxides such as BTO and PZT, exhibit a relatively large remnant polarization in the range of 50 – 100 μC/cm^2. Therefore, ferroelectric oxides as the gate promise much higher doping effects. Ferroelectric oxides exhibit much higher dielectric constants, compared with which promise much higher doping effects.[160] To date, a wide spectrum of 2D materials, including graphene, TMDs, phosphorene, have been integrated with ferroelectric materials to fabricate 2D materials/ferroelectric FETs, in which 2D materials work as semiconductor transport channels and ferroelectric materials behave as gate dielectrics.[161] The electric-field effect induced doping is determined by the gate voltage V_g and the build-in polarization field P,[160]

$$n(V_g) = ((\kappa\varepsilon_0 V_g)/d + P)/e \qquad (7)$$

Here, n is the carrier density of 2D materials, κ is the dielectric constant of the ferroelectric gate, ε_0 is the vacuum permittivity, d is the thickness of the ferroelectric film, and e is the free electron charge. As to the hysteresis relationship between the polarization and electric field, the gate voltage V_g exerting on ferroelectrics will introduce a remarkable hysteresis effect in the charging doping.[162] Once the gate voltage exceeds the coercive voltage, resistance hysteresis can be observed in ferroelectric gated graphene, which can be used to develop non-destructive readout non-volatile memory. In real ferroelectric-graphene hybrid systems, it should also pay attention to the presence of interface charges. The complex interface chemistry will compete with the ferroelectric gating effect, which may surpass designers' initial conception. However, the absence of a bandgap makes graphene less desirable for FET applications that require high ON/OFF ratios of drain currents. The gapless graphene also leads to short photocarrier lifetime, resulting in inefficient photocurrent generation.[9] TMDs are considered as promising alternatives to graphene because they possess bandgaps which are required for many applications in electronics and optoelectronics.[163] MoS_2 as a representative TMD possesses a tunable bandgap covering the range from 1.2 to 1.8 eV. One of the blockbuster exhibitions that brought attention to 2D semiconductors was the realization of FET with a high current ON/OFF ratio based on monolayer MoS_2. The TMDs-based photodetectors have shown the ability to cover the range from infrared to visible, because the TMDs possess modest bandgaps in the range of 1-2 eV. For MoS_2/FET structure

photodetectors, a suitable combination of the gate bias (V_g) and drain-source bias (V_{sd}) may lead to a ultrahigh photosensitivity.[14] In ferroelectric-gated MoS_2-based photodetectors, ferroelectric gate can be used to suppress the dark current of the MoS_2 semiconducting channel. Consequently, TMDs-based photodetectors combined with ferroelectric non-volatile gating not only reduce the power dissipation but also improve the detector sensitivity.

5. Recent Progress and Applications

The ability to control the optical properties of functional materials is highly desirable for developing high-performance optoelectronic and photonic devices. Progress in this area has been extensively explored by using diverse external or internal physical stimuli. Theory and experiment have shown that it is an effective approach to render the optical properties by the introduction of piezoelectric and ferroelectric effects. Especially with the fast development of novel materials, control and coupling of the optical processes with ferroelectric and piezoelectric materials are attracting an increasing academic curiosity. This section will demonstrate some recent progress on applying ferroelectric and piezoelectric effects to emerging materials with diverse designs and configurations, as well as their device applications, including photodetectors, photovoltaics, light sources, and light-emitting devices with unprecedented characteristics or unique functionalities.

5.1. Ferroelectric and Piezoelectric Tuning of Lanthanide-Doped Phosphors

Spectral tuning and enhancement of PL based on lanthanide-doped phosphors is particularly important for their applications.[164] In addition, some ferroelectric materials such as BTO, LNO and KNO, are potential integrated optical components due to their superb electro-optic and nonlinear optical coefficients. Owing to the abundant energy levels, color-tunable luminescence can be realized in Ln^{3+}-doped phosphors. A series of $Yb^{3+}/Er^{3+}/Tm^{3+}$ tri-doped BTO phosphors have shown broad color tunability covering three primary colors red-green-blue (RGB), as well as the white light.[165] The energy transfer from sensitizer Yb^{3+} ions to Er^{3+} and Tm^{3+} ions has great influence on the optical processes. With the rapid development of MEMS, multifunctional materials are highly desirable. In lanthanide-doped BTO, besides luminescent properties, co-existed ferroelectricity was also observed. Bismuth titanates (e.g., $Bi_4Ti_3O_{12}$), have a typical bismuth-layered perovskite structure. $Bi_4Ti_3O_{12}$ is a sort of environmentally-friendly ferroelectric materials and has good electrical and optical properties.

Bao *et al.* have synthesized a series of lanthanide ions-doped $Bi_4Ti_3O_{12}$ thin films prepared by chemical solution deposition methods, in which both strong upconversion luminescence and ferroelectricity co-exist.[166] Over these years, many scientist have put their efforts into the interplay between the luminescent behavior and ferroelectric activity, such as the polarization, phase transition and piezoelectric potential. The introduced lanthanide elements in ferroelectric materials not only exhibit strong luminescence, but also enhance the ferroelectric properties of the hosts. Wang *et al.* have shown that great enhancement of ferroelectric and piezoelectric properties was observed in Er^{3+}-doped $CaBi_4Ti_4O_{15}$.[167] They ascribed the polarization enhancement to the structural distortion resulting from Er^{3+} ions substitution for Bi^{3+} and Ca^{3+} ions, as well as the vacancies at the A site of perovskite host lattices.

It is well-known that BTO as a prototype ferroelectric will undergo successive phase transitions with changing the temperature. Er^{3+} ion is very sensitive to the change of surrounding environment. We have investigated the PL response of the Er^{3+}-doped BTO ceramics within the temperature range from 15 to 300 K.[78] Er^{3+} ion can substitute Ba^{2+} (A-site) or Ti^{4+} ion (B-site) depending on Ba/Ti ration. When the temperature passed through 150 K and 250 K, two sudden changes in the PL intensity of the Er^{3+} ion located at A-site was observed, which may arise from the phase transition induced host lattice changes. The PL intensity of the Er^{3+} ion at B-site presented different response. With the temperature decreasing from 300 K to 15 K, the electrons at the upper $^2H_{11/2}$ level was thermally quenched to the nearby lower $^4S_{3/2}$ level. Therefore, the light emission from $^2H_{11/2}$ level was strongly suppressed, while the emission from $^4S_{3/2}$ level increases remarkably. Besides thermal quenching, the enhanced light emission is also due to the lower symmetry around the Er^{3+} ion resulting from the phase transitions. Thus, Er^{3+} ion can be used as a spectroscopic probe for ferroelectric phase transition. Besides Er^{3+} ion, Pr^{3+} is another most utilized lanthanide dopant ion for many applications. Shen *et al.* have used Pr^{3+} ions to probe the polarization and phase transition of $(Ba_{0.77}Ca_{0.23})TiO_3$.[168] After poling, red light emission from the $^1D_2 \rightarrow {}^3H_4$ transition of Pr^{3+} ion is enhanced around 30%. The variation of the crystal field during poling leads to the enhancement of the red emission. Both the red and blue emission of Pr^{3+} ion show the peaks around 100 K, which is coincided with the phase transition temperature (from orthorhombic to tetragonal) of $(Ba_{0.77}Ca_{0.23})TiO_3$ ceramic. Lanthanide ions can be used to probe the ferroelectric behavior. Conversely, ferroelectric polarization can also modulate the luminescent properties of lanthanide-doped ferroelectrics. Chu *et al.* have studied the relationship between PL spectra of Er^{3+}-doped KNO with the poling electric field.[65] The polarization of KNO effectively enhanced the fine Stark splitting components of $^2H_{11/2}/^4S_{3/2}$

$\rightarrow {}^4I_{15/2}$ transitions of Er^{3+} ions. Our group has first realized the modulation of upconversion PL via electric field in epitaxial Yb^{3+}/Er^{3+}-doped BTO thin films as shown in **Figure 6**a.[26] Here, taking advantage of the benefits brought by thin-film structure, we can exert high electric field on thin films with a relatively small voltage. Figure 6b shows that the overall green emission from the ${}^2H_{11/2}/{}^4S_{3/2} \rightarrow {}^4I_{15/2}$ transitions of Er^{3+} ion is amplified 2.7 times with a bias of only 10 V. While, external electric field has hardly any influence on the red emission from the ${}^4F_{9/2} \rightarrow {}^4I_{15/2}$ transition. This is because the green emission originated from hypersensitive transition of Er^{3+} ion is more sensitive to the local field changes. It is concluded that ferroelectric polarization has a wavelength-dependent impact on different ED transitions (Figure 6c). Considering the structural symmetry of ferroelectrics is switchable, it offers an opportunity to tune the light emission in a reversible and dynamic manner. Figure 6d shows the synchronous control of the PL intensity with a sinusoidal voltage, which is obviously unrealizable with chemical approaches. Subsequently, other research groups followed this way and reported ferroelectric polarization enhanced PL from Pr^{3+}-doped ferroelectrics. Jia *et al.* reported ferroelectric polarization induced enhancement in Pr^{3+}-doped $(Bi_{0.5}Na_{0.5})TiO_3$ ceramics, which is attributed to the polarization-induced structural distortion.[169] Wang *et al.* found that the PL intensity of Pr^{3+}-doped diphase $Ba_{1-x}Ca_xTiO_3$ (x = 0.7) ceramics was enhanced up to 100% after poling.[170] Kwok *et al.* demonstrated that the PL intensity in 0.2 mol% Pr^{3+}-doped $Ba_{0.85}Ca_{0.15}Ti_{0.90}Zr_{0.10}O_3$ ferroelectric ceramics was regulated through external electric field.[171] Therefore, the electric field modulation based on ferroelectrics establishes a new avenue towards to tunable lanthanide-doped phosphors. It should be noted that transition metal ions as another important kind of activators, their optical properties can be strongly influenced by the environmental perturbations.[41, 172] Hence, the ferroelectric tuning method applied to lanthanide ions is believed to be effective for transition metal ions-doped phosphors.

Besides electric field, elastic strain can be an alternative method to tune the PL of lanthanide-doped phosphors. Epitaxial Yb^{3+}/Er^{3+}-doped BTO thin films were grown on PMN-PT by PLD. Upconversion PL in Yb^{3+}/Er^{3+}-doped BTO thin films was effectively tuned by the elastic strain arising from PMN-PT.[77] *In-situ* X-ray diffraction analysis indicates a strain-induced lattice change of the BTO host under different electric fields. Therefore, the modulation of PL is owing to the change of the host symmetry.[173] As mentioned above, crystal field has larger influence on the luminescence of transition metal ions. Transition metal ion Ni^{2+}-doped STO thin films were also grown on PMN-PT. Elastic strain not only can modulate the PL intensity, but also shift the NIR emission band more than 10 nm. Xu and co-workers have demonstrated

an intriguing series of multifunctional material, Pr^{3+}-doped $BaTiO_3$-$CaTiO_3$ ceramics, which can realized electro-mechano-optical three-parameter coupling (**Figure 7**a).[174] XRD analysis have shown that Pr^{3+}-doped [(1-x)$BaTiO_3$-$xCaTiO_3$] ceramics belong to diphasic materials for $x \geq 0.25$, in which tetragonal $Ba_{0.77}Ca_{0.23}TiO_3$ and orthorhombic $Ba_{0.1}Ca_{0.9}TiO_3$ coexist. Figure 7b shows the *P-E* loops for the ceramics with $x = 0.25$ and $x = 0.30$. Large electrostrictive strain levels were observed in the ceramics (Figure 7c), which may resulting from electric field induced non-180° domain rotation. Strong red mechanoluminescence (ML) emission can be seen by naked eyes as shown in Figure 7e. The interactions between the ionic polarization in Pr^{3+}-doped $Ba_{0.77}Ca_{0.23}TiO_3$ and the ferroelectric behavior in $Ba_{0.77}Ca_{0.23}TiO_3$ are responsible for the strong ML. The three-parameter coupling achieved in a single compound, has aroused a fresh surge of interest in multifunctional materials.[175]

5.2. Quantum Light Sources based on Self-assembled QDs

Quantum communication technologies are leaping out of the lab and launching into practical applications. III-V semiconductor QDs have attracted great attention owing to their potential use as deterministic sources of single and entangled photons. The realization of fine tuning the optical properties of QDs is a prerequisite towards to the exploitation of QDs in quantum technologies. In this section we will summarize recent results on the strain field tuning the exciton emission of QDs.

Precise control over the emission energy of QDs is a key issue in many quantum optics experiments. Single photons emitted from the QDs can be fine-tuned to the energy in resonance with the D_2 hyperfine transition of the ^{87}Rb atom. Single photons propagating through ^{87}Rb atomic vapor can be slowed down, which may lead to the realization of quantum memories.[176] Kumar *et al.* fabricated high quality GaAs/AlGaAs QDs which can generate single photons with emission wavelength around 780 nm.[177] A reversible strain-induced wavelength shift has been achieved by integrating thin nanomembranes containing QDs onto piezoelectric actuators made of PMN-PT. Owing to the huge strain provided by PMN-PT, the strain-induced energy shift of the QDs can be up to 10.5 meV, which almost covers the inhomogeneous spectral broadening of all prepared QDs. For single photon interference experiments, the emission energy and lifetime from In(Ga)As QDs have been simultaneously tuned by the application of electric and strain fields.[178] With increasing the voltage on PMN-PT from -200 V to 800 V, the emission energy of the neutral exciton is tuned up to 11 meV. While, the decay time is decreased from 1.44 ns to 0.78 nm via the strain field. The vertical

electric field can shift the emission energy about 6 meV through the GSE. More importantly, the combination of electric and strain fields allows independently tuning the lifetime, while keeping the emission energy fixed by a closed-loop feedback system.

The entangled photon pairs can be generated from self-assembled QDs through the biexciton cascade process: biexciton (XX) – exciton (X) – ground state (G).[179] Asymmetric nature of the QDs gives rise to the broken degeneracy of the bright excitonic states, which contributes to the FSS. The fidelity of the entangled photon pairs from QDs will be strongly reduced due to the presence of FSS. So-called "time reordering" scheme can realize entangled photon pairs generation, which does not need to meet the stringent requirement on the FSS.[180] However, the emission energies of exicton (X) and biexciton (XX) for the "time reordering" scheme should be identical. Ding *et al.* observed that biaxial strain originated from PMN-PT substrates can effectively tune the binding energies E_B of both charged exciton (X^+) and biexciton (XX) in InGaAs/GaAs QDs.[181] Through control of the binding energies E_B of XX by the biaxial strain, the emission energies of X and XX can be tuned to be the same, addressing the energy coincidence requirement for the "time reordering" scheme.

Some methods based on electric or strain field, or a combination of them, have been applied to suppress or erase the FSS of QDs.[182] Vertical electric field represents a powerful post-growth technology to manipulate the emission energy as well as the FSS of QDs via the GSE.[101] Meanwhile, electric field can be also used to electrically trigger light-emitting diodes containing semiconductor QDs (QLEDs), which is one major advantage of QDs over other quantum light sources. However, static electric field is not competent to electrical pump and emission energy tuning at the same time. An alternative approach to manipulate the FSS is to apply uniaxial stress. Seidl *et al.* successfully reduced the FSS of the InGaAs QD from 30 μeV to 15 μeV under an applied uniaxial stress based on a PZT stack.[104] Compared with PZT, PMN-PT is more qualified for piezoelectric actuators, which can promise larger strain tuning ability. Singh *et al.* claimed that the bright exciton states undergo an anticrossing under the applied uniaxial stress.[183] Later, this prediction was testified by experiment. Plumhof *et al.* investigated anisotropic biaxial strain impacting on the emission of neutral excitons confined in GaAs/AlGaAs and InGaAs/GaAs QDs.[184] Membranes containing QDs is placed on the side faces of the PMN-PT actuator, so that anisotropic biaxial strain can be applied on the QDs. Both the polarization and FSS are tuned by anisotropic strain. For GaAs/AlGaAs QDs under anisotropic strain, the polarization direction is rotated up to 79º, while the FSS is decreased about 70μeV. The observed anisotropic strain-induced tuning in the polarization

and FSS is ascribed to substantial changes of the hole states. Furthermore, theoretical analysis reveals that the tunability of the FSS is affected by the direction of the uniaxial strain. QLEDs are composed of a n-i-p nanomembrane structure, in which QDs are embedded for generating single photons and entangled photon pairs on demand under electrical injection. Trotta *et al.* investigated the effect of strain field on the emission properties of QLEDs.[103] As show in **Figure 8**a, QLED nanomembranes containing InGaAs QDs are transferred on gold-coated PMN-PT. A planar cavity including a Distributed Bragg Reflector (DBR) is grown on the top of the QLED nanomembrane, which is designed for extracting photons from the QLED more efficiently. The photon collection efficiency is found to be magnified about 20 times due to the presence of the cavity-enhancement design. Figure 8b shows the SEM image of the cross section of the compact device. The strain-tunable QLEDs possess two control voltages. In order to electrically trigger the photon emission from QDs, a voltage V_d is applied across the OLED diode. In the meantime, a voltage V_p is applied to the PMN-PT (corresponding to the out-of-plane electric field F_p) for generating piezoelectric strain on the QDs. Figure 8c shows the colour-coded micro-electroluminescence (μ-EL) map of the QD depending on V_d, keeping the out-of-plane electric field $F_p = 0$ kV cm^{-1}. Fixing the current flowing through the QLED at 4.2 nA cm^{-2}, the emission spectra for the exciton (X), biexciton (XX) and negatively charged exciton (X^-) changing along with F_p are shown in Figure 8d. With increasing the compressive strain, the emission lines for all the excitonic species demonstrate blue shift. While under tensile strain, all the emission lines show red shift. The controlling range for all the emission lines is more than 20 meV without degrading the spectral linewidth. Figure 8e shows the X^- emission energies from two different QDs are tuned into coincidence with the resonance of the cavity mode. Figure 8f shows that the FSS of a chosen QD is reduced down to 5 μeV under compressive strain (corresponding to $F_p \sim 40$ kV/cm). Figure 8g shows the linear relationship between the binding energy of XX transition and the electric field F_p, indicating strain can linearly modulate the biexciton binding energy, which meets the requirement for entangled photon generation through the “time reordering” scheme.

One great advantage of QLEDs as quantum emitter is the fast generation rate of single photons and entangled photon pairs on demand. QLEDs containing InGaAs QDs were transferred on the PMN-PT actuator. By injecting subnanosecond electrical pulses into the diode, single photon was triggered with a very high excitation repetition rate up to 800 MHz. Meanwhile, the emission energy of single photons can be tuned by the PMN-PT in a broad range.[185] Zhang *et al.* demonstrated a strain-tunable high-speed QLED.[182] The generation

rate for entangled photon pairs is up to 400 MHz. Uniaxial strain from PMN-PT can be used to eliminate the FSS. As a result, up to 30% of QDs allow for entangled photon emission. Meantime, the entanglement fidelity of the strain-tunable QLED can be up to 0.83. The strain-tunable QLEDs promise ideal high-speed quantum light sources for quantum technologies. As described above, elastic strain based on single-crystal PMN-PT represents an effective mean for engineering the optical properties of QDs with unrivaled precision and technological relevance. However, previous research mainly based on PMN-PT bulks with a thickness of 300 – 500 μm, which prevents the further development of chip-integrated devices. Piezoelectric actuators made from bulk materials need very high burden voltages (up to 1000V). In addition, each device can only tune one QD at one time due to the processing difficulty on bulk PMN-PT, resulting in low integration density. MEMS incorporating piezoelectric thin films can overcome the aforementioned obstacles. Arrays of piezoelectric actuators with four independent actuation legs were made of a 15-μm thick PMN-PT thin-film on Si substrate (**Figure 9**a).[106] Arrays of QDs-containing nanomembranes were then transferred onto the center region of PMN-PT actuators. Figure 9b shows the cross section of the device. The photograph of single device as well as the connections is shown in Figure 9c. Compared with single actuator, the combination of four independent actuation legs can provide ultra-flexible anisotropic strain. Previous study has shown that the efficiency of strain on the FSS is strongly associated with the direction of the applied strain. By tuning the magnitude and sign of the voltages on the four-legged device, the FSS for entangled photons with different energies have been effectively eliminated (Figure 9d). Taking advantage of thin-film structure, the burden voltage is effectively reduced. The exciton energy is tuned up to 10 nm under a voltage of 50 V. The four-legged actuator represents a powerful device for strain engineering on QDs nanomembranes, as well as other low-dimensional materials. Besides using transfer and bonding methods, PMN-PT thin films can be also monolithically integrated with the Si substrates, which could bring opportunities for on-chip quantum photonics (Figure 9g).[107] PMN-PT thin films were epitaxially grown on STO buffered Si substrates. The thickness of thin films can be reduced down to several hundred nanometers, dramatically decreasing the voltage down to several volts. Thin-film structure is beneficial to high density integration of actuators. Arrays of suspended PMN-PT actuators have been fabricated using focused ion beam (FIB) and wet chemical etching (Figure 9h). The in-plane clamping of the film as well as the residual stress are released as a result of the fabrication of the suspended bridge structures, which can exert larger in-plane biaxial stress to the QDs

nanomembranes. Such monolithically integrated PMN-PT actuators represent a ideal platform for developing on-chip quantum photonics.

5.3. Enhanced Optoelectronic Performances by the Piezo-phototronic Effect

Wurtzite-type semiconductors, including ZnO, GaN and ZnS, simultaneously possess semiconductor and piezoelectric properties, in which the three-way coupling of semiconductor properties, piezoelectricity and optical excitation gives rise to the piezo-phototronic effect. To date, the piezo-phototronic effect has been extensively used to improve the performances of various optoelectronic devices, including LEDs, photodetectors, and luminescence devices.

5.3.1. Piezo-phototronic Effect Enhanced LEDs

Light emission from LEDs is as a result of the charge carriers injection and recombination in a forward-biased p-n junction. The meaning of the piezo-phototronic effect is to add an additional freedom to modulate the performances of LEDs, and subsequently expand their functions. Semiconductor ZnO with wurtzite structure has been used to develop high-efficiency ultraviolet (UV) LEDs owing to its direct wide bandgap (~3.37 eV) and large excitonic binding energy (~60 meV).[152] Up to now, there are many reports on the heterojunction LEDs made from n-type ZnO combined with p-type semiconductors, such as GaN, Si and so on. The piezo-phototronic effect focuses on the influence of strain field on LEDs. Yang *et al.* reported that strain field can effectively improve the quantum efficiency and injection current in LEDs based on n-ZnO/p-GaN heterojunction.[186] Two reasons are responsible for the enhanced efficacy of LEDs. First, strain-induced piezopotential effectively modifies the band profile, which is beneficial for current injection. Second, the presence of piezopotential creates a trapping dip for charge carriers at the vicinity of the junction, which significantly enhances the quantum efficiency of the LEDs.

Through the piezo-phototronic effect, strain field can effectively improve the performance of piezoelectric semiconductors-based LEDs. If reverse the same process, an array of LEDs made of piezoelectric semiconductors can work as a light-emitted stress sensor. Many groups have demonstrated various stress sensors with high tactile sensitivity and resolution, which is of great importance in artificial intelligence. Previous stress sensors mainly converted mechanical stimuli into electrical signals. Pan and co-workers demonstrated an optical

readout pressure sensor using a ZnO nanowire LED array, which converts the stress input into light emission intensity.[187] The schematic of the device is illustrated in **Figure 10**a. Each n-ZnO nanowire combining with p-GaN represents a single LED pixel. Figure 10b shows the scanning electron microscopy (SEM) image of the ZnO nanowire arrays on the GaN substrate. The spatial resolution of pressure sensor depends on the centre distance between two adjacent pixels, which is measured about 4 μm, corresponding to a spatial resolution of 6,350 dpi. Figure 10c shows the schematic scenario of optical readout sensor measuring two-dimensional pressure. Figure 10d shows the optical image of the convex mould used for applying pressure. Figure 10e-g shows the light emission intensities of the sensor under different strain levels of 0, -0.06%, and -0.15%, respectively. The distribution and magnitude of the applied strain can be deduced from the contrast of light emission. An enhancement factor $E(x,y)=[I_{\varepsilon}(x,y)- I_0(x,y)]/I_0(x,y)$ is introduced for quantitative analysis. Figure 10h shows the two-dimensional contour map of the $E(x,y)$ factor derived from the light emission intensity shown in Figure 10e and 10g. As shown in Figure 10i and 10j, the the $E(x,y)$ factor of LED emission under a -0.15% strain is enhanced more than 4-fold compared with that of under a -0.06% strain, which unambiguously shows the effectiveness of pressure sensor based on the piezo-phototronic effect. Furthermore, future human-like robotics and wearable electronics need to develop flexible and adaptive pressure sensors. Flexible optical readout pressure sensors are composed of n-ZnO nanowire array with p-type PEDOT: PSS polymer.[188] These prototype optical readout pressure sensors endowed with ultrahigh spatial resolution can satisfy the requirements of artificial intelligence and wearable electronics. Silicon is the fundamental building blocks for electronics as well as the emerging silicon photonics. Taking advantage of mature semiconductor techniques, silicon photonics allow for integrating the optical and electronic components onto a single chip. Silicon-based optical readout pressure sensors were fabricated by using n-ZnO thin-film to cover the p-Si micropillar array.[189] The LEDs emission intensity of the n-ZnO/p-Si pixel can be enhanced by 120% under -0.05% compressive stains as a result of the piezo-phototronic effect. The silicon-based piezo-phototronic LED arrays is a big step toward the development of chip-integrated optical readout sensors for detecting pressure and force distributions.

5.3.2. Piezo-phototronic Effect Enhanced Photodetectors

The driving force in a photodetector to separate photogenerated electron-hole pairs depends on the characteristics of the p-n junction or Schottky junction.[153] The Schottky barrier height

determines the sensitivity of the photodetectors containing Schottky junctions. A ZnO nanowire based photodetector with a metal-semiconductor-metal (MSM) structure demonstrates ultrahigh sensitivity for UV light due to the low dark current.[36] Two back-to-back Schottky junctions suppress the dark current. More importantly, when applying a compressive strain on the ZnO nanowire, the strain-induced piezopotential can modulate the Schottky barrier height, thus influence the responsivity of the photodetector. CdSe is another wurtzite-type semiconductor with a bandgap compatible with the visible light range. The compressive strain applied on CdSe-based photodetector gives rise to the piezopotential in CdSe nanowire, which can increase the Schottky barrier height to promote the separation of photogenerated electron-hole pairs.[190] While, the redistribution of the photogenerated electrons and holes will reduce the Schottky barrier height of the device. Therefore, the electric field derived by the piezopotential can compensate the loss of the build-in electric field due to the light illumination. Recently, a flexible self-powered MSM-based GaN photoswitch was reported.[191] Upon a small strain of 1%, the UV on/off ratio of the GaN photoswitch is increased up to 154% on the basis of the piezo-phototronic effect.

For the p-n junction-based photodetectors, the strain modulation can be explained through the width change of the depletion zone and the band profile deformation.[153] ZnO/CdS nanowire heterojunctions allow UV/visible light detection.[147] Under strain, the photodetectors based on ZnO/CdS heterojunctions are achieved an enhancement of up to 718% in sensitivity. Similarly, a high-performance broad band UV/visible photodetector has been fabricated with a wide bandgap ZnO/ZnS heterojunction core/shell nanowire array.[192] The responsivity of the detector has been enhanced by three orders of magnitude under a compressive strain. Si-based photodetectors containing p-n junction can be also involved with the piezo-phototronic effect.[193] Hybrid photodetector is formed with n–type ZnO nanowire grown on p-type Si substrate with micropyramids. An enhancement of 177% in responsivity and a shorten of 87% in response time were obtained by applying a compressive strain. The combination of the expansion and shift of the depletion region, as well as the band profile bending at the vicinity of p-n junction contributes to the optimal performances of photodetectors. With similar mechanism, photodetectors made from CdSe/ZnTe core-shell structure also realize an improved photosensitivity.[194]

5.3.3. Piezo-phototronic Effect in Luminescence Applications

Light-emission devices incorporating with piezoelectric semiconductors promise the possibility to couple with strain fields through the piezo-phototronic or piezophotonic effect. The piezophotonic effect is the coupling between piezoelectric properties and photoexcitation, where the strain-induced piezopotential modulates the band structure within piezoelectric phosphors, and thus tunes/controls the relevant optical process.[195] Light emission stimulated by elastic strains can be realized with the ML phosphors. ML phosphors may be promising in a wide spectrum applications, such as artificial skins,[196] dual-mode light/ultrasound probes,[146] and wind-driven displays,[197] etc. Since the ML materials can directly convert the mechanical stimuli into optical response almost instantaneously, a dynamic pressure sensor has been fabricated with the ML phosphor ZnS:Mn particles. **Figure 11**a shows the schematic of the pressure sensor matrix (PSM).[195] The ZnS:Mn layer was sandwiched by the PET thin films. Figure 11b shows the ML intensity from the PSM device under different applied forces. The PSM device based on ML phosphors supports the instant response to external stress. A practical application of the PSM is to capture personal securer signature. As shown in Figure 11c, the force of handwritten word "piezo" corresponds to the relative intensity of the ML emission. The dynamic pressure mapping device promises prospective applications in real-time pressure sensing. The mechanism of the light emission from ZnS:Mn under mechanical stress is shown in Figure 11d. The imposed stress gives rise to piezopotential in wurtzite-structured ZnS, which tilts the bands of ZnS. Then, the detrapped electrons at the defect states can escape to the conduction band, followed with the recombination of electrons and holes non-radiatively. The released energy excites the Mn^{2+} dopant ions, and photon emission occurs when the excited Mn^{2+} ions return to the ground state.

An agile and controllable piezophotonic light emission can be realized by integrating the ML phosphors layer with piezoelectric actuators. We have realized dual-mode light and ultrasound emission from ZnS:Mn thin film grown on piezoelectric PMN-PT substrates (Figure 11e).[146] PMN-PT single crystals have been used to develop high-performance ultrasound probes owing to the superb piezoelectric response and electromechanical coupling factor. Figure 11f shows the pulse-echo waveform as well as the frequency spectrum of the PMN-PT substrate. The ML emission from ZnS:Mn triggered by PMN-PT is shown in Figure 11g. Therefore, the ZnS:Mn/PMN-PT hybrid structures are capable of simultaneous generation of luminescence and ultrasound waves. However, ZnS:Mn thin films fabricated by PLD is rigid, limiting the spread applications of ZnS based phosphors. We have further developed flexible light-emitting devices made from the composite ML phosphor-based hybrid structures, which can meet the easy and low-cost requirements. Light emission from

the flexible composites was observed upon piezoelectric straining. The ML intensity shows a linear relation with the magnitude and frequency of the applied strain.[198] One severe hindrance to develop chip-integrated ZnS:Mn/PMN-PT hybrid devices is the thickness of the PMN-PT bulks. In order to overcome this barrier, we have utilized single-crystal PMN-PT thin films bonded with silicon substrates to replace PMN-PT bulks as the actuators.[199] The use of PMN-PT thin films significantly reduces the microfabrication complexity, as well as the burden voltage. Arrays of PMN-PT actuators have been fabricated with a small footprint of 120 μm×100 μm. More importantly, each actuator can be manipulated independently, providing us the ability to control of the light emission in single pixel. Figure 11h demonstrates the addressability of the device, which can not be achieved with PMN-PT bulks. The color tunability is highly sought for light-emitting devices. Figure 11i and 11j show the continuous tuning of the ML spectra of ZnS:Cu,Al layer, and ZnS:Cu,Al/ZnS:Mn bilayer by changing the strain frequency, respectively. The corresponding CIE coordinates exhibit blue shift with increasing frequency. These results distinctly suggest the potential to develop a more compact and colorful piezophotonic light source or display with the single pixel addressability.

The classification of the phosphors can be determined by the excitation sources. For example, PL and EL phosphors are excited by electromagnetic wave and electric field, respectively. The ML phosphors aforementioned can be triggered by mechanical stress. However, it is rare to find in literature about light emission excited by magnetic field, indicating that luminescence excited with magnetic field directly is very difficult to implement in a single compound. Therefore, we have proposed a magnetic-field-induced luminescence (MIL) solution, in which light emission can be triggered by low-magnetic-field via strain-mediated coupling with piezophotonic phosphors (**Figure 12**a).[200] In our design, the MIL composite is composed of two parts, namely one is the magnetic elastomer layer formed with FE-Co-Ni alloy particles embedded in the poly(dimethylsiloxane) (PDMS), while the other part is the ML phosphors layer composed of ZnS doped with metal ions (e.g., Al, Cu) mixed with PDMS (Figure 12b). Figure 12c shows the SEM image of the interface between the elastomer layer and the ML phosphors layer. Under magnetic field, the magnetic elastomer layer can impose strain on the ML phosphors layer to generate light emission. Most recently, we have shown that by modulating the frequency of magnetic field at room temperature, ML spectra from the flexible composites of ZnS:Al,Cu phosphors can be tuned by the applied magnetic field in a real-time and *in-situ* manner (Figure 12d-f), which offers new opportunities in magnetic-optical coupling.[201] Moreover, such a novel temporal approach can be used to

modulate red-color-blue (RGB) color gamut for display and color temperature for solid state lighting in our work.

5.4. Ferroelectric Photovoltaics

The photovoltaic effect in ferroelectrics has recently attracted renewed attention. High-efficiency ferroelectric solar cells rely on the strong absorption of solar energy, the careful selection of barrier-free electrodes, effective separation and collection of photogenerated carriers. This section will review recent progress in ferroelectric photovoltaics, as well as some exotic phenomena from their interaction with photons.

In theory, ferroelectric materials with relative narrow bandgaps and high polarizations are favored for photovoltaic cells. However, many ferroelectric oxides (e.g., LNO, BTO, PZT) possess wide bandgaps (> 3 eV), meaning that only small portion of sunlight energy can be absorbed. Recently, ferroelectric photovoltaics have been intensively studied based on BFO due to its small bandgap of ~2.7 eV and large polarization (~90 $\mu C/cm^2$). Nevertheless, the present solar cells made from BFO only allow the absorption of ~20% of the sunlight. Therefore, bandgap engineering of the ferroelectric materials is significant to improve the sunlight absorption. The wide bandgaps of ferroelectric materials arise largely from the strongly localized *d*-electrons of the transition-metal atoms. Considerable effort went into narrowing the bandgaps of ferroelectric oxides through substituting the transition metal atoms. Grinberg *et al.* have shown that ferroelectric perovskites $[KNbO_3]_{1-x}[BaNi_{1/2}Nb_{1/2}O_{3-\delta}]_x$ (KBNNO) solid solutions possess a large bandgap tunability ranging from 1.1 eV to 3.8 eV. What's more, KBNNO with x = 0.1 composition exhibits a direct bandgap of 1.39 eV which meets the ideal value of 1.4 eV for semiconductor photovoltaic cells. Ferroelectric $KNbO_3$ (KNO) is mixed with $BaNi_{1/2}Nb_{1/2}O_{3-\delta}$ (BNNO) to form KBNNO. Nb ions at the B-site are replaced by the combination of Ni ions and oxygen vacancy. First-principle calculations show that the electronic structure with a narrow bandgap can be composed by a hybridized Ni 3*d* and O 2*p* states derived valence band and a Nb 4*d* states derived conduction band. The substituted Ni ions introduce electronic states in the gap of KBNNO, resulting in the narrow bandgap. Taking the advantage of the smaller bandgap values, KBNNO has demonstrated strongly enhanced absorption efficiency. Furthermore, with decreasing the bandgap, KBNNO is transferred to a semiconductor ferroelectric with an improved conductivity. Under green light illumination, the photocurrent density generated in KBNNO could reach up to 4 $\mu A\ cm^{-2}$,

almost 50 times of that in PZT. Nechache *et al.* have demonstrated that multiferroic Bi_2FeCrO_6 (BFCO) exhibits a narrow bandgap down to 1.4 eV.[108] Changing the chemical ordering of the Fe/Cr cation can alter the bandgap of BFCO via the Jahn-Teller effect. By tuning the deposition rate, both the Fe/Cr cation ordering and the ordered domain size can be tuned, resulting in each BFCO layer with different bandgaps. Photovoltaic device made of BFCO with multilayer configuration have yielded an unprecedented PCE up to 8.1%, approaching the performances of other solar cells.

The photovoltaic effect in ferroelectric materials is featured with large photovoltage above bandgap, as well as extremely small photocurrent. One effective method to enhance the photocurrent is to reduce the thickness of ferroelectric films. Compared with bulk lanthanum-doped lead zirconium titanate (PLZT), the photocurrent per unit width in PLZT thin films was found to be magnified over 100 times.[202] Qin *et al.* reported that PCE could be significantly enhanced with thickness reduction due to the improved photogenerated carriers collection. They found that a PCE of 0.29% was achieved in epitaxial PLZT thin films.[203] Further remarkably enhanced photovoltaic effect was observed in BTO thin films. Compared to the bulk BTO, PCEs of BTO thin films were strongly magnified over 10000 times.[111] It can be concluded that once the thickness of the ferroelectric films is comparable to the shift distance of the photogenerated carriers, the PCE can be significantly enhanced. Besides thickness, crystallographic orientation is another critical factor in ferroelectric photovoltaics. Ichiki *et al.* reported that the photovoltaic power output in a crystallographic (001) oriented PLZT thin film is almost 20 times larger than that of random oriented films, which was ascribed to the photovoltaic coefficients of oriented films are superior to those of random oriented films.[204] The photocurrent can be influenced by the Schottky barrier as well as the depletion region, which becomes more evident in thin-film ferroelectric photovoltaics. Through reducing the barrier height at the electrode/ferroelectric interface, a higher photovoltaic efficiency has been achieved in metal/PLZT/ITO cells.[205] Another alternative method to improve the PCE of ferroelectric solar cells is incorporating a semiconductor material into the ferroelectric solar cells to increase the conductivity of devices. The photocurrent in ITO/PZT/Pt cells is greatly enhanced by introducing a n-type semiconducting Cu_2O buffer layer.[115] Cu_2O can form an ohmic contact with the Pt electrode. The removal of the PZT/Pt Schottky barrier promotes the collection of photogenerated electrons. Furthermore, the n^+–n band structure at PZT/Cu_2O junction suppresses the photogenerated electron and hole recombination. Therefore, through the interface engineering, the photocurrent density for PZT-based solar cell is strongly enhanced from 0.04 mA/cm^2 to 4.80 mA/cm^2. An amorphous silicon (a-Si) film was inserted

into the Ag/a-Si/PZT/ITO/glass structure to increase the PCE. The a-Si film serves two purposes in the device. One is to absorb the solar energy in the visible region. The other is to form a Schottky barrier with PZT for promoting the migration of the photogenerated electrons.[116]

Domain walls have become the research hotspot in the field of photoferroelectrics since the discovery of the anomalous photovoltaic effect in BFO thin films. Yang *et al.* reported that a very large photovoltaic voltage observed in BFO thin films could be associated with domain walls.[19] The magnitude of the photovoltage was found to be in direct proportion to the number of domain walls. As shown in **Figure 13**, the photovoltaic effect is also affected by the orientation of domain walls. The photovoltaic effect can only be detected once the photocurrent measurement is perpendicular to the domain walls. If the photocurrent measurement is along the domain walls, no photovoltaic effect is observed. They supposed that the electric field in domain walls were the origin of the anomalous photovoltaic effect in BFO thin films. However, subsequent theoretical and experimental results indicated that the anomalous photovoltaic effect in BFO films should be ascribed to the bulk photovoltaic effect. Moreover, domain walls and defects can effectively render the photovoltaic effect in ferroelectrics. Seidel *et al.* reported that domain walls played a critical role in carrier generation and recombination.[206] Recently, the local photovoltaic effect in BFO consisting of pure 71º domain walls has been explored at nanoscale resolution. Local photocurrent measurement has elucidated that domain walls can improve the photocurrent as a result of high photoconductivity rather than the internal electric field.[207]

Besides the photovoltaic effect, BFO has exhibited various exotic properties interacted with photons. For instance, light-induced mechanical response has been highly pursued for sensors and actuators. Kundys *et al.* reported a substantial photostriction of BFO crystals at room temperature.[21] The illumination on BFO crystals results in a change of the crystal dimension of $\sim 10^{-5}$ within 0.1 s. The magnitude of photostriction was found to rely on the polarization of illumination and the applied magnetic field. A combination of photovoltaic and electrostrictive effects may contribute to this intriguing phenomenon. These results indicate the potentiality of BFO as optically triggered strain generators. Furthermore, Lejman *et al.* have shown that gigahertz (GHz) coherent shear phonons can be generated in BFO ceramic via the reverse piezoelectric effect.[208] Besides mechanical response, THz radiation from BFO thin films has been observed upon excitation with femtosecond laser.[22] Through measuring the amplitude of the THz radiation, the polarization states of BFO thin films can be learned.[209] These results can be used to generate THz radiation, or to probe the ultrafast

polarization dynamics of ferroelectric memories. It is anticipated the interaction between multiferroics and photons can give rise to more miraculous results.

5.5. Optoelectronic Devices based on HOIPs

In recent years, HOIPs have been subjected to extensive studies due to applications in photonics and optoelectronics. More particularly, HOIPs are soaring as the most promising candidates for the solar cell technology.[210] This section will review recent progress of HOIPs used in photovoltaics, photodetectors, and LEDs. The ferroelectric nature of hybrid perovskites as an important question remains unanswered. Here we also discuss recent development on this topic.

Affecting factors including architecture, composition, deposition process, and interface layers, have been optimized to promote the PCE of hybrid perovskite solar cells. Seok's group demonstrated that a perovskite solar cell with a certified PCE of 22.1% is achieved by introducing the iodide ions into the dripping solution.[23] The additional iodide ions would both facilitate the formation of the crystalline α- formamidinium lead iodide ($FAPbI_3$) phase and minimize the defects in the perovskite layers. The defect-engineering method is proven to be essential for obtaining high-efficiency hybrid perovskite solar cells. In order to harvest more solar energy, the hybrid perovskite materials have been integrated with Si and copper indium gallium selenide (CIGS) to fabricate tandem cells.[211] However, the complicated interconnection between sub-cells hampers the development of the multijunction tandem cells. Ergen *et al.* have proposed graded bandgap perovskite solar cells to overcome the obstacles that traditional tandem cells face. The graded bandgap perovskite solar cells are made of two perovskite materials ($CH_3NH_3SnI_3$ and $CH_3NH_3PbI_{3-x}Br_x$). A monolayer hexagonal boron nitride (h-BN) is introduced between two perovskite layers. Heavily doped GaN is chosen as the electron injection layer. The graphene aerogel in hole transport layer facilitates the hole collection.[212] The graded bandgap perovskite solar cells exhibit average PCEs up to 18.41%, which provide new ideas to improve the efficiency of solar cells. Leblebici *et al.* investigated the microstructure of perovskite crystals.[213] Some local parameters associated with the photovoltaic performances, e.g., short-circuit photocurrent, open-circuit voltage and dark drift current have been *in-situ* investigated using conducting atomic force microscopy. The photovoltaic efficiency of perovskite solar cells exhibits facet-dependent characteristic. They found that each facet of the perovskite materials can act as an individual solar cells. Therefore, the control of the microcrystal grain and facet orientation could be an effective way for further

pushing the efficiency of perovskite solar cells to the limit. In spite of impressive process, the stability of perovskite solar cells remains a severe challenge to be solved. Shin and coworkers reported that using the La^{3+}-doped $BaSnO_3$ (LBSO) electrode to replace mesoporous TiO_2 as the electron transporting layer can improve the photostability of perovskite solar cells.[214] LBSO electrode can be prepared via a superoxide colloidal solution route under mild conditions. The perovskite solar cells fabricated with LBSO electrode and $MAPbI_3$ have shown a maximum PCE up to 21.2%. More importantly, the LBSO-based solar cells can retain 93% of its initial performance after 1000 hours of exposure to sunlight.

Besides the applications in photovoltaics, perovskite-based photodetectors have made significant progress. Perovskite materials have a high quantum yield in the visible spectrum, which is particularly appealing for visible light detection. Dou *et al.* reported ultrasensitive photodetectors based on hybrid perovskite $MAPbI_{3-x}Cl_x$.[138] By introducing conjugated polymers as the hole-blocking layer, the dark current was strongly inhibited, which ensures the high detectivity. The perovskite photodetectors exhibit a large detectivity close to 10^{14} Jones, which is much higher than that of a Si photodetector in the visible range. The perovskite photodetectors also demonstrate a ultrafast photoresponse. The rise and fall times are both less than 200 ns for the perovskite photodetectors with 0.01 cm^2 size. The transient response of the detector was found to be associated with the detection areas. The slow response of detectors with larger area is attributed to the small carrier mobility of the PCBM transporting layer, as well as the RC constant of the circuit. Huang's group further developed a low noise perovskite photodetector with detection limit down to sub 1 pW cm^{-2}.[139] **Figure 14**a shows the schematic of the perovskite photodetectors. Figure 14b shows the dark current and photocurrent of the photodetectors sweeping the voltage from -2 to 1.5 V. The dark current is reduced down to 9.1 $\times 10^{-9}$ A cm^{-2} level under -2 V bias as a result of the presence of the C_{60} fullerence layer. The dark current will be suppressed once the C_{60} layer is introduced over the perovskite inhibiting the leakage current. Furthermore, the band structure of the photodetector can be modified to further eliminate the dark current. As shown in Figure 14c, both the introduced OTPD and C_{60} layers increase the carrier injection barrier heights, resulting in a ultralow dark current. The small dark current ensures the supersensitive performance of the perovskite photodetectors. Figure 14d shows the external quantum efficiency (EQE) of the photodetectors. The high EQEs for all three kinds of devices are close to 90%, indicating high responsivity of the perovskite photodetectors. The use of the suitable buffer layer enables the perovskite photodetectors with even better sensitivity.

Hybrid perovskites have been also used for X-ray detection. It has been demonstrated that a solution processed $MAPbI_3$-based X-ray detector exhibits high sensitivity and responsivity for X-ray signals.[137] Later, Huang and co-workers have achieved a X-ray detector made from monolithically integrating single-crystal $MAPbBr_3$ onto Si substrate. The X-ray detector with single-crystal perovskite is endowed with impressive sensitivity up to 2.1×10^4 μC Gy_{air}^{-1} cm^{-2}, which is more than 1000 times better over the sensitivity of commercial amorphous selenium detectors.[215] Hence, the perovskite materials will be promising candidates for ultrasensitive X-ray photodetectors.

Hybrid perovskites have been used in high-performance LEDs due to their high PL quantum yield, high color purity, tunable bandgaps and low defect density.[216] LEDs made from solution-processed hybrid perovskites were first reported in 2014.[217] Perovskites-based LEDs demonstrated EL colors tunability in a wide range through altering the chemical formulation of the perovskites. By control of the halide combinations, the optical bandgaps can be adjusted, resulting in green, red and near-infrared emissions. The peak brightness of the LEDs was around 360 cd m^{-2}, giving an EQE of 0.1%. In the past few years, perovskite-based LEDs have gained great improvement. Great effort has been devoted to the interfacial engineering of the devices to improve the EQE. By introducing a polyethyleneimine (PEI) layer covering the perovskite layer, LEDs made of $MAPbBr_3$ have demonstrated bright green emission showing a maximum luminance up to 20 000 cd m^{-2} and an EQE of 0.8%.[218] The PEI interlayer serves a double purpose. One is to cover the perovskite layer for eliminating the leakage pinhole. The other is to decrease the barrier height of cathode electrodes for electron injection. In order to further improve the efficiency of perovskite-based LEDs, Cho *et al.* reported the methods to modify the stoichiometry as well as the morphology of the perovskite active layers. Since the exciton binding energy of $MAPbBr_3$ is larger than that of $MAPbI_3$, excess MABr was added to increase the radiative recombination efficiency. Smaller grain size can confine electrons and holes so as to improve the radiative recombination. They used the nanocrystal pinning (NCP) technology to reduce the grain sizes down to 100 nm, and improve the surface roughness of the perovskite layer. The NCP-processed LEDs demonstrated an EQE up to 8.53%.[219] With the advance in the synthesis technology, Xiao *et al.* further reduced the perovskite grains down to 10 nm, and obtained a highly efficient perovskite-based LEDs with an EQE of 10.4%.[220] Therefore, perovskite-based LEDS with confined structures can effectively improve the efficiency of LEDs. LEDs made from perovskite nanocrystals could be the direction for perovskite-based LEDs.[221]

In spite of great achievement, HOIPs still encounter several important issues to be addressed. Among them, whether HOIPs truly exhibit ferroelectricity remains controversial. An interesting feature of HOIPs is that external stimuli such as temperature, pressure, and electric fields can induce a reversible phase transition. $MAPbI_3$ undergoes reversible transitions between cubic (α), tetragonal (β), and orthorhombic structures.[131] The unusual hysteresis in the current-voltage curves is also thought to be related with the presence of ferroelectricity. First principles calculations suggest the existence of ferroelectricity in $MAPbI_3$.[222] The presence of ferroelectricity will aid the separation of carriers and concomitant longer diffusion length. Materials belonging to ferroelectric should meet several stringent criteria, including the non-centrosymmetric structure, electric-field-controllable polar domains, as well as the remnant polarization. To date, the generation of the polarization in HOIPs is attributed to the rotation of MA^+ ions. Some groups have observed ferroelectric domains in $MAPbI_3$ from experiments. Kutes *et al.* firstly observed ferroelectric domains in β-$MAPbI_3$ perovskite thin films using piezoelectric force microscopy (PFM).[134] And the ferroelectric domains can be reversed by dc biases. Polarization in $MAPbI_3$ films is further verified by piezo-phase hysteresis loops. At room temperature tetragonal $MAPbI_3$ exhibits poor polarization retention, only persists in one second.[223] However, Kim *et al.* reported the retention time in $MAPbI_3$ could be 60 min. They observed spontaneous polarization in $MAPbI_3$ in the absence of electric field. The retention time of the polarization is found to be associated with the perovskite crystal size. The observed much longer retention time is attributed to the increased ferroelectric domain size. [224] Ferroelectric materials are featured with stable *P-E* hysteresis loop. Hybrid perovskites such as $MAPbI_3$ can be regarded as narrow bandgap semiconductors. Hence, detecting the *P-E* loops in HOIPs via conventional methods remains challenging (**Figure 15**a). Very recently, Rakita *et al.* have provided the *P-E* hysteresis loops of tetragonal $MAPbI_3$ derived by investigating the imaginary part of the dielectric response.[25] The observed pyroelectricity is a direct evidence for the polarity of $MAPbI_3$. Figure 15b shows the dielectric response of a $MAPbI_3$ crystal. In semiconducting ferroelectrics, the dielectric response is dominated by the imaginary part. By integrating the imaginary part of the permittivity (ε_{im}) over the bias electric field, *P-E* hysteresis loop can be obtained as shown in Figure 15c. The innovation of their method is to use ε_{im} instead of the real part of the permittivity ε_{re} to investigate the dielectric response. Ordered periodic stacks were observed after chemical etching as shown in Figure 15d, confirming the existence of polar domains. The observed second harmonic generation (SHG) indicates the absence of an inversion symmetry (Figure 15e,f). All these evidences experimentally confirm that tetragonal $MAPbI_3$

is ferroelectric. However, up to now, reliable remnant polarization has not yet been experimentally observed in $MAPbI_3$ at room temperature. Therefore, despite recent progress, more work is still needed to clarify the ferroelectricity in perovskites. Recent theoretical studies have shown that ferroelectric domains can effectively influence the photovoltaic behavior of HOIPs. For examples, Monte Carlo simulations have shown that the presence of ferroelectric nanodomains can reduce carrier recombination losses.[225] Later, first-principles calculations reveal that ferroelectric domain walls can reduce the bandgaps significantly, as well as promote the charge separation.[132, 226] A density-functional-based tight-binding (DFTB) model coupled to nonequilibrium Green's function method further confirms that ferroelectric domain walls improve the conductance of perovskites owing to the reduced bandgap. Furthermore, the charge carriers recombination is strongly suppressed due to the separation of carrier transport paths.[227]

There are also many interesting observations in HOIPs interacting with photons. For example, Wang *et al.* reported strong interaction between polarization and light in $MAPbI_3$ films.[228] The polarization was observed to be switched by light illumination caused by ionic motions and photovoltaic field. Another intriguing phenomenon of the light-matter interaction in HOIPs is that $MAPbBr_3$ demonstrated significant photostriction under visible light illumination.[229] Under illumination, the photovoltaic effect induced electric field can reorient the MA cations. The reorientation of MA cations in $MAPbBr_3$ contributes to the lattice distortions via the translation-rotation coupling, resulting in the significant photostriction. These results suggest that the indepth exploration of HOIPs can give rise to unpredictable device characteristics.

5.6. Ferroelectric/Piezoelectric Effect on 2D Materials

2D materials are generally needed to combine with some bulk functional materials which can provide the mechanical support to the 2D materials. Moreover, the functional materials also can improve the original properties and excite brand new properties through the interface coupling effect or even construct electronic and optoelectronic devices and significantly broaden the spectrum of applications.[162] For example, SiO_2 was firstly reported to be integrated with graphene as the gate dielectric layer to provide an electric field doping for graphene to fabricate the FETs.[79] Until now, the applications of 2D materials have been explored from the basic FETs to phototransistors, then to a wide range of potential applications in optoelectronics.[13]

5.6.1 Graphene on Ferroelectrics

Graphene was reported to couple with ferroelectric PZT thin films by Zhu *et al*.[161] A non-volatile memory was achieved in graphene/ferroelectric FETs (GFeFETs).[230] The transport performances of graphene have been effectively modulated by the nonlinear ferroelectric polarization.[231] It should be noted that strain engineering in graphene is extensively studied because of the possibility of opening a bandgap to graphene. Ferroelectric materials also possess the piezoelectric effect due to the non-centrosymmetric crystal structure. Strain engineering based on piezoelectric materials has been used to tune the physical properties of graphene.[232] Furthermore, it is feasible to achieve n-type graphene through ferroelectric polarization reversal.[233] Graphene as top electrodes can effectively switch the polarization direction of the PZT. In turn, the polarization of the PZT can change the type and density of carriers of the graphene. Besides, the conductivity and carrier doping level of large-area graphene can be improved by integrating graphene with organic ferroelectric PVDF-TrFE.[234] The integrated heterostructure graphene/PVDF on polyethylene terephthalate (PET) substrates exhibits good optical transparency and mechanical flexibility. For the sheet resistance (R_s) measurements, about 10 μm PVDF-TrFE film was spin coated onto graphene after transferring on SiO_2. The initial R_s of graphene is about 1440 Ω/squr. After fully polarizing the ferroelectric polymer, 120 Ω/squr of R_s can be achieved. Considering the flexibility of both graphene and the ferroelectric polymer, the hybrid materials can be regarding as promising flexible and transparent electrodes for electronic and optoelectronic devices. Nevertheless, the absence of a bandgap makes pristine graphene less desirable for photodetectors. Hybrid perovskites (e.g., $MAPbI_3$) possess intriguing optical properties for optoelectronic applications. Photodetectors composed of pristine graphene and $MAPbI_3$ perovskite have shown an ultrahigh photosensitivity.[235] **Figure 16**a shows the schematic design of the hybrid photodetector. Figure 16b shows the optical image of the perovskite layer covering the graphene. Figure 16c shows the drain current of the hybrid device as a function of the gate voltage under different illumination wavelengths. Figure 16d displays the photocurrent of the photodetector at $V_G = 0$ V changing along with the illumination wavelength. The photocurrent of the hybrid photodetector demonstrates a significant decline over 800 nm, which corresponds to the absorption cut-off wavelength of the perovskite-graphene hybrid structure. The hybrid photodetector demonstrates a high photoresponsivity in broad spectra range. The performances of the novel photodetector, including the

photoresponsivity, the effective quantum efficiency and the photodetectivity are shown in Figure 16e. The superb photoresponses of the hybrid photodetector arise from the presence of graphene inhibiting the fast recombination of the photo-excite pairs in $MAPbI_3$ layer.
The vertical graphene heterostructure FETs represent an alternative conceptual graphene-based FETs. The vertical integration of graphene with inorganic semiconductors, oxide semiconductors and other 2D layered materials have demonstrated substantially improved on/off rations (>10^4), overcoming one massive obstacle faced by graphene-based FETs.[236] Such vertical layered architectures have already shown great potential for field-effect tunneling transistors and optoelectronic devices.[237] In order to further improve the performance of the vertical graphene heterostructure FET, inspired by ferroelectric tunnel junction, Yuan *et al.* used an ultrathin ferroelectric BFO film as the tunnel barrier layer. Ultrahigh current on/off ratio of 7×10^7 was realized through switching the ferroelectric polarization of the BFO film in this novel vertical structured FET at room temperature.[159] Such tunnel graphene-based FETs open up a new avenue for ferroelectric materials as building blocks for 2D electronics.

5.6.2 TMDs on Ferroelectrics

Follow the roadmap of graphene, 2D materials have been reported to be integrated with ferroelectric/piezoelectric materials in order to achieve novel performance. First non-volatile memory composed of MoS_2 integrated with ferroelectric PVDF was reported by Lee *et al*. in 2012.[238] Similarly, non-volatile memories have been achived with other TMDs, such as p-type WSe_2.[239] The WSe_2/PZT FETs demontrate high ON/OFF ratio (> 10^4) and low switching voltages (< 2.5 V). Yui *et al.* have investigated piezoelectric strain effects on the PL of CVD-grown MoS_2 layers sheets.[143] Monolayer MoS_2 has been directly grown on periodically poled $LiNbO_3$ (LNO) substrate by the CVD method.[16] It was reported that monolayer MoS_2 prefers to grow on the ferroelectric surface where the polarization pointing to “up” with respect to the surface. The prepared the MoS_2 layers were well templated by the ferroelectric LNO polarization pattern without further need of lithography. Furthermore, both electrical and optical dual operation can be achieved based on MoS_2/PZT FETs.[240] As schematically shown in **Figure 17**a, ferroelectric PZT thin film was employed to serve as the gate dielectric in the FET structure. The MoS_2/PZT phototransistors demonstrate unique advantages compared to its graphene counterparts, such as high ON/OFF ratio and the dual operation mode, i.e., writing or erasing both in electrical and optical modes. The electrically

writing or erasing behavior is shown in Figure 17b. The hysteresis transport properties can be achieved for MoS_2 sample due to the ferroelectric non-volatile attributes. After 5 min, a high conductivity (ON state) can be achieved if a negative gate voltage (-6 V) was previously applied. Conversely, a low conductivity (OFF state) can be realized if a positive gate voltage (+6 V) was applied. The ON/OFF ratio recorded initially is up to 10^4. After 10000 s, this value reduces down to 22 due to the dissipation of the interfacial charges. Furthermore, when the fabricated MoS_2/PZT FET is exposed to a visible light, the photogenerated charge carriers in MoS_2 form an electric field, which could in turn modify the polarization state of the underlying PZT thin film. As shown in Figure 17c, both the ON and OFF states can be erased by the illumination light. After 5 min light illumination, the ON and OFF states can't be distinguished. The indistinguishable states is reserved until the illumination light is tuned off, suggesting that the stored data in MoS_2/PZT memories can be erased optically.
The stable remnant polarization of ferroelectric materials can provide a non-volatile and large gate voltage for 2D materials. Ultrasensitive photodetector bases on MoS_2/PVDF phototransistor has been reported.[14] Figure 17d demonstrates the schematic of top gated MoS_2/PVDF phototransistor. The hybrid photodetecor exhibits ultrahigh photosensitivity as a result of the high doping provided by ferroelectric PVDF. Figure 17e shows the photocurrent evolution with a rapid rising and falling response and finally reaching a steady state. The rise and decay times can be confirmed to be less than 2 ms. The photoresponse of the ferroelectric gating MoS_2 based photodetector illuminated by the laser with wavelengths ranging from 500 to 1550 nm is shown in Figure 17f. Typically, photoresponse spectra of a MoS_2 based photodetector is in the range from visible to near-infrared (850 nm) by considering the band gap of MoS_2 (1.2 to 1.8 eV). However, the hybrid photodetector can detecte laser illumination with wavelengths up to 1550 nm, which is attributed to the ferroelctric field induced band profile modification of the MoS_2 layers. Therefore, the stratagy of coupling 2D materials with the ultrahigh electrostatic field provided by ferroelectric materials provides new avenue to develop high performance hybrid optoelectronic devices.

5.6.3 Piezoelectric MoS_2-based Photodetectors

The recent observed piezoelectricity in monolayer MoS_2 enables a broad spectrum of new applications.[52] By utilizing the observed piezoelectricity, Wu *et al.*demonstrated the first experimental observation of piezo-phototronic effect in monolayer MoS_2 and used it in strain-gated adaptive photodetection.[241] **Figure 18**a shows the optical image of the two-terminal

device based on monolayer MoS_2 on flexible PET substrate. Figure 18b displays the photoresponse for monolayer MoS_2 under the illumination intensity from 0 (dark state) to 4.297 mW/cm^2 without strain. The rectification characteristics indicate the asymmetry of the two Schottky barriers. Figure 18c demonstrates the photocurrent by applying different strain provided by stretching or bending the underlying PET polymer. It is found that the strain dependence of the photocurrent is more significant at low illumination intensity. This is because high illumination intensity generates high free carrier density, which will screen the strain-induced piezopotential. Piezoelectricity was observed in monolayer MoS_2 due to the non-centrosymmetric structure. The piezo-phototronic effect impacting on monolayer MoS_2-based photodetector is similar to its influence on wurtzite-type semiconductors. As shown in Figure 18d, strain-induced piezopotential can modify the Schottky barrier heights, which have great influence on the separation and transport of photo-generated carriers. Taking into account 2D materials' superior mechanical strength and optical properties, these atomically thin 2D semiconductors could offer an opportunity for developing flexible nano-optoelectro-mechanical systems.

6. Summary and Outlook

In summary, the cutting-edge topic of ferroelectric and piezoelectric control and coupling of the optical processes in advanced materials and devices has been comprehensively reviewed. Strain engineering based on giant piezoelectric single-crystal PMN-PT, allows for modulating the optical properties of Ln^{3+} or transition metal ion doped phosphors, 2D materials and semiconductor QDs in an *in-situ* and reversible manner. Emission energy, binding energy as well as the FSS from QDs emitters have been effectively tuned by the strain generated from PMN-PT, which is highly desirable for quantum optics. Beyond working as external perturbations, piezoelectricity intrinsically existed in wurtzite-type semiconductors with non-symmetrical structure gives rise to the piezo-phototronic and piezophotonic effects, which have been extensively to improve the performances of photodetectors, solar cells and light emitting devices. By manipulating the strain and piezopotential of the composite phosphors, some new concept of devices, such as MIL based sensor and display can be conceived and realized. As an important class of smart materials, ferroelectrics with variable crystal symmetry provide unique responses to external perturbations including electric field, strain and temperature. The host environments expert a strong crystal field on the luminescent activators. The electric-field-induced luminescence modulation in metal ion-doped

ferroelectric thin-films provides an ideal platform to *in-situ* and dynamically investigate crystal field impacting on the optical processes of luminescent ions. Ferroelectric materials endowed with photoresponse properties are defined as photoferroelectrics. In the photoferroelectric research field, the PCE of ferroelectric photovoltaics can be optimized through meticulous engineering with the bandgaps, electrode interfaces, as well as domain walls,. In addition, the multiple degrees of freedom in multiferroic BFO mean more exotic phenomenon interact with photon can be observed, such as giant photostriction as well as THz radiation. Layered materials integrated with functional materials not only can improve the intrinsic properties, but also introduce new properties through the interface coupling effect. Considerable effort has been devoted to the integration of 2D materials with ferroelectrics to fabricate novel electronic and optoelectronic devices. Strong piezoelectricity has been observed from monolayer MoS_2, which indicates great potential use of the piezo-phototronic effect in the 2D new platform. HOIPs have been regarded as the most promising photovoltaic candidates owing to their outstanding properties, including large absorption coefficient, range, long diffusion length, modest carrier mobility as well as the simple and low-cost assembling process. To date, the PCE of perovskite solar cell has passed the 22% milestone. Furthermore, HOIPs have been also employed for high-performance photodetectors and LEDs. The possible existence of ferroelectricity in HOIPs is suggested to facilitate the separation of electrons and holes, resulting in the superb photovoltaic performance. However, there has been no stable remnant polarization detected in $MAPbI_3$ at room temperature. More experimental work is still needed for supporting the evidence of ferroelectricity in perovskites and its potential interplay with the optoelectronic properties.

Despite encourage progress, there are still many issues to be addressed. Development in this field needs further understanding of the fundamental physics. Some interactions between ferroelectric and optical processes as aforementioned are still open questions. For instance, the explanation of modulation of the Ln^{3+}-doped ferroelectrics is based on the semi-empirical J-O theory. Theoretical model deduced using first-principles density-functional theory should be created for Ln^{3+}-doped ferroelectrics. The existence of piezoelectricity and ferroelectricity in emerging optoelectronic materials is not just a theoretical issue. Although the coupling between piezoelectricity, ferroelectricity and optoelectronic properties in these materials promises exciting device characteristics, a great challenge to be faced is how to enhance the coupling efficiency in diverse hybrid systems. Another barrier toward flexible and transparent optoelectronics is the brittle nature of conventional ferroelectric oxide. Therefore, more attention should be paid on polymer-based ferroelectrics and piezoelectric materials with

improved performance. Considering their superior flexibility and mechanical strength, recent findings of piezoelectricity and ferroelectricity in 2D materials are expected to become increasingly important in developing ultrathin and flexible devices. HOIPs have risen up as a class of important optoelectronic materials owing to their exceptional attributes. One principal challenge associated with HOIPs is their stability. Yang *et al.* have summarized five ways to improve the stability of hybrid perovskite cells.[242] With continuous effort, the stability of perovskites is expected to improve in near future. In conclusion, both ferroelectric and piezoelectric effects provide useful tools to control and modulate the optical properties of various materials and devices. It is anticipated that a convergence of ferroelectric and piezoelectric effects, with emerging optoelectronic materials will lead to exciting discoveries and promising applications.

Acknowledgements

This work was supported by the grants from Research Grant Council of Hong Kong (GRF No. PolyU 153031/15P) and NSFC (No. 11474241 and No. 61604100).

Received: ((will be filled in by the editorial staff))
Revised: ((will be filled in by the editorial staff))
Published online: ((will be filled in by the editorial staff))

References

[1] E. C. Nelson, N. L. Dias, K. P. Bassett, S. N. Dunham, V. Verma, M. Miyake, P. Wiltzius, J. A. Rogers, J. J. Coleman, X. Li, P. V. Braun, Nat. Mater. 2011, 10, 676.
[2] P. M. Rørvik, T. Grande, M.-A. Einarsrud, Adv. Mater. 2011, 23, 4007; R. J. Zeches, M. D. Rossell, J. X. Zhang, A. J. Hatt, Q. He, C. H. Yang, A. Kumar, C. H. Wang, A. Melville, C. Adamo, G. Sheng, Y. H. Chu, J. F. Ihlefeld, R. Erni, C. Ederer, V. Gopalan, L. Q. Chen, D. G. Schlom, N. A. Spaldin, L. W. Martin, R. Ramesh, Science 2009, 326, 977.
[3] L. W. Martin, A. M. Rappe, Nat. Rev. Mater. 2016, 2, 16087.
[4] D. G. Schlom, L.-Q. Chen, C.-B. Eom, K. M. Rabe, S. K. Streiffer, J.-M. Triscone, Annu. Rev. Mater. Res. 2007, 37, 589.
[5] C.-B. Eom, S. Trolier-McKinstry, MRS Bull. 2012, 37, 1007.
[6] N. Setter, D. Damjanovic, L. Eng, G. Fox, S. Gevorgian, S. Hong, A. Kingon, H. Kohlstedt, N. Y. Park, G. B. Stephenson, I. Stolitchnov, A. K. Taganstev, D. V. Taylor, T. Yamada, S. Streiffer, J. Appl. Phys. 2006, 100, 051606.
[7] W. Wu, Z. L. Wang, Nat. Rev. Mater. 2016, 1, 16031.
[8] Q. H. Wang, K. Kalantar-Zadeh, A. Kis, J. N. Coleman, M. S. Strano, Nat Nano 2012, 7, 699.
[9] F. Bonaccorso, Z. Sun, T. Hasan, A. C. Ferrari, Nat. Photon. 2010, 4, 611.
[10] K. F. Mak, J. Shan, Nat Photon 2016, 10, 216; S. Shahi, Nat. Photon. 2010, 4, 506.

[11] N. O. Weiss, H. Zhou, L. Liao, Y. Liu, S. Jiang, Y. Huang, X. Duan, Adv. Mater. 2012, 24, 5782.
[12] K. S. Novoselov, V. I. Fal′ ko, L. Colombo, P. R. Gellert, M. G. Schwab, K. Kim, Nature 2012, 490, 192; K. F. Mak, J. Shan, Nat. Photon. 2016, 10, 216; X. Yu, K. Sivula, ACS Energy Lett. 2016, 1, 315.
[13] F. H. L. Koppens, T. Mueller, P. Avouris, A. C. Ferrari, M. S. Vitiello, M. Polini, Nat. Nanotechnol. 2014, 9, 780.
[14] X. Wang, P. Wang, J. Wang, W. Hu, X. Zhou, N. Guo, H. Huang, S. Sun, H. Shen, T. Lin, M. Tang, L. Liao, A. Jiang, J. Sun, X. Meng, X. Chen, W. Lu, J. Chu, Adv. Mater. 2015, 27, 6575.
[15] W. Y. Kim, H.-D. Kim, T.-T. Kim, H.-S. Park, K. Lee, H. J. Choi, S. H. Lee, J. Son, N. Park, B. Min, Nat. Commun. 2016, 7, 10429.
[16] A. Nguyen, P. Sharma, T. Scott, E. Preciado, V. Klee, D. Sun, I. H. Lu, D. Barroso, S. Kim, V. Y. Shur, A. R. Akhmatkhanov, A. Gruverman, L. Bartels, P. A. Dowben, Nano Lett. 2015, 15, 3364.
[17] P. Michler, A. Kiraz, C. Becher, W. V. Schoenfeld, P. M. Petroff, L. Zhang, E. Hu, A. Imamoglu, Science 2000, 290, 2282; C. Santori, D. Fattal, J. Vučković, G. S. Solomon, Y. Yamamoto, Nature 2002, 419, 594; N. Akopian, N. H. Lindner, E. Poem, Y. Berlatzky, J. Avron, D. Gershoni, B. D. Gerardot, P. M. Petroff, Phys. Rev. Lett. 2006, 96, 130501.
[18] A. Rastelli, F. Ding, J. D. Plumhof, S. Kumar, R. Trotta, C. Deneke, A. Malachias, P. Atkinson, E. Zallo, T. Zander, A. Herklotz, R. Singh, V. Křápek, J. R. Schröter, S. Kiravittaya, M. Benyoucef, R. Hafenbrak, K. D. Jöns, D. J. Thurmer, D. Grimm, G. Bester, K. Dörr, P. Michler, O. G. Schmidt, Phys. Status Solidi B 2012, 249, 687.
[19] S. Y. Yang, SeidelJ, S. J. Byrnes, ShaferP, C. H. Yang, M. D. Rossell, YuP, Y. H. Chu, J. F. Scott, J. W. Ager, L. W. Martin, RameshR, Nat. Nanotechnol. 2010, 5, 143.
[20] J. Kreisel, M. Alexe, P. A. Thomas, Nat. Mater. 2012, 11, 260.
[21] B. Kundys, M. Viret, D. Colson, D. O. Kundys, Nat. Mater. 2010, 9, 803.
[22] K. Takahashi, N. Kida, M. Tonouchi, Phys. Rev. Lett. 2006, 96, 117402.
[23] W. S. Yang, B.-W. Park, E. H. Jung, N. J. Jeon, Y. C. Kim, D. U. Lee, S. S. Shin, J. Seo, E. K. Kim, J. H. Noh, S. I. Seok, Science 2017, 356, 1376.
[24] T. Chen, W.-L. Chen, B. J. Foley, J. Lee, J. P. C. Ruff, J. Y. P. Ko, C. M. Brown, L. W. Harriger, D. Zhang, C. Park, M. Yoon, Y.-M. Chang, J. J. Choi, S.-H. Lee, Proc. Natl. Acad. Sci. USA 2017, 114, 7519.
[25] Y. Rakita, O. Bar-Elli, E. Meirzadeh, H. Kaslasi, Y. Peleg, G. Hodes, I. Lubomirsky, D. Oron, D. Ehre, D. Cahen, Proc. Natl Acad. Sci. USA 2017, 114, E5504.
[26] J. Hao, Y. Zhang, X. Wei, Angew. Chem. Int. Ed. 2011, 50, 6876.
[27] F. Wang, X. Liu, Chem. Soc. Rev. 2009, 38, 976.
[28] Z. Yang, J. Hao, Small Methods, DOI: 10.1002/smtd.201700296.
[29] S. Manzeli, D. Ovchinnikov, D. Pasquier, O. V. Yazyev, A. Kis, Nat. Rev. Mater. 2017, 2, 17033.
[30] J. Huang, Y. Yuan, Y. Shao, Y. Yan, Nat. Rev. Mater. 2017, 2, 17042.
[31] M. Dawber, K. M. Rabe, J. F. Scott, Rev. Mod. Phys. 2005, 77, 1083.
[32] W. Wu, C. Pan, Y. Zhang, X. Wen, Z. L. Wang, Nano Today 2013, 8, 619.
[33] C. Paillard, X. Bai, I. C. Infante, M. Guennou, G. Geneste, M. Alexe, J. Kreisel, B. Dkhil, Adv. Mater. 2016, 28, 5153.
[34] S.-H. Baek, M. S. Rzchowski, V. A. Aksyuk, MRS Bull. 2012, 37, 1022.
[35] Z. L. Wang, J. Song, Science 2006, 312, 242.
[36] Q. Yang, X. Guo, W. Wang, Y. Zhang, S. Xu, D. H. Lien, Z. L. Wang, ACS Nano 2010, 4, 6285.
[37] Q. Zhang, R. W. Whatmore, J. Phys. D: Appl. Phys. 2001, 34, 2296.
[38] K. Lefki, G. J. M. Dormans, J. Appl. Phys. 1994, 76, 1764.

[39] S. H. Baek, J. Park, D. M. Kim, V. A. Aksyuk, R. R. Das, S. D. Bu, D. A. Felker, J. Lettieri, V. Vaithyanathan, S. S. N. Bharadwaja, N. Bassiri-Gharb, Y. B. Chen, H. P. Sun, C. M. Folkman, H. W. Jang, D. J. Kreft, S. K. Streiffer, R. Ramesh, X. Q. Pan, S. Trolier-McKinstry, D. G. Schlom, M. S. Rzchowski, R. H. Blick, C. B. Eom, Science 2011, 334, 958.
[40] Y. Zhang, T. Kämpfe, G. Bai, M. Mietschke, F. Yuan, M. Zopf, S. Abel, L. M. Eng, R. Hühne, J. Fompeyrine, F. Ding, O. G. Schmidt, Thin Solid Films 2016, 607, 32.
[41] Y. Zhang, J. Hao, J. Mater. Chem. C 2013, 1, 5607.
[42] S. Abel, T. Stöferle, C. Marchiori, C. Rossel, M. D. Rossell, R. Erni, D. Caimi, M. Sousa, A. Chelnokov, B. J. Offrein, J. Fompeyrine, Nat. Commun. 2013, 4, 1671.
[43] J. F. Scott, C. A. Paz de Araujo, Science 1989, 246, 1400.
[44] E. Y. Tsymbal, A. Gruverman, Nat. Mater. 2013, 12, 602.
[45] J. Hoffman, X. Pan, J. W. Reiner, F. J. Walker, J. P. Han, C. H. Ahn, T. P. Ma, Adv. Mater. 2010, 22, 2957.
[46] Y. Yuan, Z. Xiao, B. Yang, J. Huang, J. Mater. Chem. A 2014, 2, 6027.
[47] X. X. Xi, H.-C. Li, W. Si, A. A. Sirenko, I. A. Akimov, J. R. Fox, A. M. Clark, J. Hao, J. Electroceram. 2000, 4, 393; J. Hao, W. Si, X. X. Xi, R. Guo, A. S. Bhalla, L. E. Cross, Appl. Phys. Lett. 2000, 76, 3100; J. H. Hao, J. Gao, Z. Wang, D. P. Yu, Appl. Phys. Lett. 2005, 87, 131908.
[48] D. Fu, M. Itoh, in *Ferroelectric Materials - Synthesis and Characterization*, (Ed: A. P. Barranco), InTech, Rijeka 2015, Ch. 05.
[49] C. Zhou, Y. Chai, Adv. Electron. Mater. 2017, 3, 1600400.
[50] K. J. Choi, M. Biegalski, Y. L. Li, A. Sharan, J. Schubert, R. Uecker, P. Reiche, Y. B. Chen, X. Q. Pan, V. Gopalan, L. Q. Chen, D. G. Schlom, C. B. Eom, Science 2004, 306, 1005.
[51] T. Ryoko, F. Desheng, I. Mitsuru, D. Masahiro, K. Shin-ya, J. Phys.: Condens. Matter 2009, 21, 215903.
[52] W. Wu, L. Wang, Y. Li, F. Zhang, L. Lin, S. Niu, D. Chenet, X. Zhang, Y. Hao, T. F. Heinz, J. Hone, Z. L. Wang, Nature 2014, 514, 470; H. Zhu, Y. Wang, J. Xiao, M. Liu, S. Xiong, Z. J. Wong, Z. Ye, Y. Ye, X. Yin, X. Zhang, Nat. Nanotechnol. 2014, 10, 151.
[53] K. Chang, J. Liu, H. Lin, N. Wang, K. Zhao, A. Zhang, F. Jin, Y. Zhong, X. Hu, W. Duan, Q. Zhang, L. Fu, Q.-K. Xue, X. Chen, S.-H. Ji, Science 2016, 353, 274.
[54] Y. Zhou, D. Wu, Y. Zhu, Y. Cho, Q. He, X. Yang, K. Herrera, Z. Chu, Y. Han, M. C. Downer, H. Peng, K. Lai, Nano Lett. 2017, 17, 5508.
[55] F. Wang, X. Liu, Acc. Chem. Res. 2014, 47, 1378.
[56] M. Shang, C. Li, J. Lin, Chem. Soc. Rev. 2014, 43, 1372.
[57] H. Dong, S.-R. Du, X.-Y. Zheng, G.-M. Lyu, L.-D. Sun, L.-D. Li, P.-Z. Zhang, C. Zhang, C.-H. Yan, Chem. Rev. 2015, 115, 10725; D. Yang, P. a. Ma, Z. Hou, Z. Cheng, C. Li, J. Lin, Chem. Soc. Rev. 2015, 44, 1416.
[58] M.-K. Tsang, W. Ye, G. Wang, J. Li, M. Yang, J. Hao, ACS Nano 2016, 10, 598.
[59] Y. Liu, Y. Lu, X. Yang, X. Zheng, S. Wen, F. Wang, X. Vidal, J. Zhao, D. Liu, Z. Zhou, C. Ma, J. Zhou, J. A. Piper, P. Xi, D. Jin, Nature 2017, 543, 229.
[60] X. Huang, S. Han, W. Huang, X. Liu, Chem. Soc. Rev. 2013, 42, 173.
[61] S. Heer, O. Lehmann, M. Haase, H.-U. Güdel, Angew. Chem. Int. Ed. 2003, 42, 3179; F. Wang, X. Xue, X. Liu, Angew. Chem. Int. Ed. 2008, 47, 906.
[62] J. Wang, T. Ming, Z. Jin, J. Wang, L.-D. Sun, C.-H. Yan, Nat. Commun. 2014, 5, 5669.
[63] G. Bai, M.-K. Tsang, J. Hao, Adv. Func. Mater. 2016, 26, 6330.
[64] G. Wang, Q. Peng, Y. Li, Chem. – Eur. J. 2010, 16, 4923; Z. Chen, G. Wu, H. Jia, K. Sharafudeen, W. Dai, X. Zhang, S. Zeng, J. Liu, R. Wei, S. Lv, G. Dong, J. Qiu, J. Phys. Chem. C 2015, 119, 24056.
[65] S.-Y. Chu, C.-H. Wen, S.-L. Tyan, Y.-G. Lin, Y.-D. Juang, C.-K. Wen, J. Appl. Phys. 2004, 96, 2552.

[66] Y. Liu, W. A. Pisarski, S. Zeng, C. Xu, Q. Yang, Opt. Express 2009, 17, 9089.
[67] B. Zhou, B. Shi, D. Jin, X. Liu, Nat. Nanotechnol. 2015, 10, 924.
[68] G. Bai, M.-K. Tsang, J. Hao, Adv. Opt. Mater. 2015, 3, 431.
[69] B. Liu, C. Li, P. Yang, Z. Hou, J. Lin, Advanced Materials 2017, 29, 1605434.
[70] F. Wang, X. Liu, J. Am. Chem. Soc. 2008, 130, 5642.
[71] F. Wang, Y. Han, C. S. Lim, Y. Lu, J. Wang, J. Xu, H. Chen, C. Zhang, M. Hong, X. Liu, Nature 2010, 463, 1061.
[72] H.-X. Mai, Y.-W. Zhang, L.-D. Sun, C.-H. Yan, J. Phys. Chem. C 2007, 111, 13721.
[73] F. Vetrone, R. Naccache, V. Mahalingam, C. G. Morgan, J. A. Capobianco, Adv. Func. Mater. 2009, 19, 2924.
[74] F. Wang, R. Deng, J. Wang, Q. Wang, Y. Han, H. Zhu, X. Chen, X. Liu, Nat. Mater. 2011, 10, 968.
[75] N. Liu, W. Qin, G. Qin, T. Jiang, D. Zhao, Chem. Commun. 2011, 47, 7671; D. M. Wu, A. García-Etxarri, A. Salleo, J. A. Dionne, J. Phys. Chem. Lett. 2014, 5, 4020.
[76] Y. Liu, D. Wang, J. Shi, Q. Peng, Y. Li, Angew. Chem. Int. Ed. 2013, 52, 4366.
[77] Z. Wu, Y. Zhang, G. Bai, W. Tang, J. Gao, J. Hao, Opt. Express 2014, 22, 29014.
[78] Y. Zhang, J. Hao, C. L. Mak, X. Wei, Opt. Express 2011, 19, 1824.
[79] K. S. Novoselov, A. K. Geim, S. V. Morozov, D. Jiang, Y. Zhang, S. V. Dubonos, I. V. Grigorieva, A. A. Firsov, Science 2004, 306, 666.
[80] S. V. Morozov, K. S. Novoselov, M. I. Katsnelson, F. Schedin, D. C. Elias, J. A. Jaszczak, A. K. Geim, Phys. Rev. Lett. 2008, 100, 016602; A. A. Balandin, S. Ghosh, W. Bao, I. Calizo, D. Teweldebrhan, F. Miao, C. N. Lau, Nano Lett. 2008, 8, 902; C. Lee, X. Wei, J. W. Kysar, J. Hone, Science 2008, 321, 385.
[81] A. K. Geim, K. S. Novoselov, Nat. Mater. 2007, 6, 183; A. K. Geim, Science 2009, 324, 1530.
[82] F. Bonaccorso, Z. Sun, T. Hasan, A. C. Ferrari, Nature Photonics 2010, 4, 611.
[83] R. R. Nair, P. Blake, A. N. Grigorenko, K. S. Novoselov, T. J. Booth, T. Stauber, N. M. R. Peres, A. K. Geim, Science 2008, 320, 1308.
[84] X. Wang, L. Zhi, N. Tsao, Ž. Tomović, J. Li, K. Müllen, Angew. Chem. Int. Ed. 2008, 47, 2990.
[85] P. Matyba, H. Yamaguchi, G. Eda, M. Chhowalla, L. Edman, N. D. Robinson, ACS Nano 2010, 4, 637.
[86] S. Bae, H. Kim, Y. Lee, X. Xu, J.-S. Park, Y. Zheng, J. Balakrishnan, T. Lei, H. Ri Kim, Y. I. Song, Y.-J. Kim, K. S. Kim, B. Ozyilmaz, J.-H. Ahn, B. H. Hong, S. Iijima, Nat. Nanotechnol. 2010, 5, 574.
[87] K. F. Mak, L. Ju, F. Wang, T. F. Heinz, Solid State Commun. 2012, 152, 1341.
[88] F. Xia, T. Mueller, Y.-m. Lin, A. Valdes-Garcia, P. Avouris, Nat. Nanotechnol. 2009, 4, 839.
[89] M. Liu, X. Yin, E. Ulin-Avila, B. Geng, T. Zentgraf, L. Ju, F. Wang, X. Zhang, Nature 2011, 474, 64.
[90] K. F. Mak, C. Lee, J. Hone, J. Shan, T. F. Heinz, Phys. Rev. Lett. 2010, 105, 136805.
[91] RadisavljevicB, RadenovicA, BrivioJ, GiacomettiV, KisA, Nat. Nanotechnol. 2011, 6, 147.
[92] A. Pezeshki, S. H. H. Shokouh, T. Nazari, K. Oh, S. Im, Adv. Mater. 2016, 28, 3216.
[93] Z. Yang, W. Jie, C.-H. Mak, S. Lin, H. Lin, X. Yang, F. Yan, S. P. Lau, J. Hao, ACS Nano 2017, 11, 4225; W. Feng, W. Zheng, W. Cao, P. Hu, Adv. Mater. 2014, 26, 6587.
[94] W. Jie, X. Chen, D. Li, L. Xie, Y. Y. Hui, S. P. Lau, X. Cui, J. Hao, Angew. Chem. Int. Ed. 2015, 54, 1185.
[95] D. J. Late, B. Liu, H. S. S. R. Matte, C. N. R. Rao, V. P. Dravid, Adv. Func. Mater. 2012, 22, 1894.

[96] D. J. Late, B. Liu, J. Luo, A. Yan, H. S. S. R. Matte, M. Grayson, C. N. R. Rao, V. P. Dravid, Adv. Mater. 2012, 24, 3549; P. Hu, L. Wang, M. Yoon, J. Zhang, W. Feng, X. Wang, Z. Wen, J. C. Idrobo, Y. Miyamoto, D. B. Geohegan, K. Xiao, Nano Lett. 2013, 13, 1649.
[97] H. Liu, Y. Du, Y. Deng, P. D. Ye, Chem. Soc. Rev. 2015, 44, 2732.
[98] R. Gusmão, Z. Sofer, M. Pumera, Angew. Chem. Int. Ed. 2017, 56, 8052.
[99] R. Trotta, E. Zallo, C. Ortix, P. Atkinson, J. D. Plumhof, J. van den Brink, A. Rastelli, O. G. Schmidt, Phys. Rev. Lett. 2012, 109, 147401.
[100] A. J. Hudson, R. M. Stevenson, A. J. Bennett, R. J. Young, C. A. Nicoll, P. Atkinson, K. Cooper, D. A. Ritchie, A. J. Shields, Phys. Rev. Lett. 2007, 99, 266802.
[101] A. J. Bennett, M. A. Pooley, R. M. Stevenson, M. B. Ward, R. B. Patel, A. B. de la Giroday, N. Sköld, I. Farrer, C. A. Nicoll, D. A. Ritchie, A. J. Shields, Nat. Phys. 2010, 6, 947.
[102] B. D. Gerardot, S. Seidl, P. A. Dalgarno, R. J. Warburton, D. Granados, J. M. Garcia, K. Kowalik, O. Krebs, K. Karrai, A. Badolato, P. M. Petroff, Appl. Phys. Lett. 2007, 90, 041101.
[103] R. Trotta, P. Atkinson, J. D. Plumhof, E. Zallo, R. O. Rezaev, S. Kumar, S. Baunack, J. R. Schröter, A. Rastelli, O. G. Schmidt, Adv. Mater. 2012, 24, 2668.
[104] S. Seidl, M. Kroner, A. Högele, K. Karrai, R. J. Warburton, A. Badolato, P. M. Petroff, Appl. Phys. Lett. 2006, 88, 203113.
[105] F. Ding, R. Singh, J. D. Plumhof, T. Zander, V. Křápek, Y. H. Chen, M. Benyoucef, V. Zwiller, K. Dörr, G. Bester, A. Rastelli, O. G. Schmidt, Phys. Rev. Lett. 2010, 104, 067405.
[106] Y. Chen, J. Zhang, M. Zopf, K. Jung, Y. Zhang, R. Keil, F. Ding, O. G. Schmidt, Nat. Commun. 2016, 7, 10387.
[107] Y. Zhang, Y. Chen, M. Mietschke, L. Zhang, F. Yuan, S. Abel, R. Hühne, K. Nielsch, J. Fompeyrine, F. Ding, O. G. Schmidt, Nano Lett. 2016, 16, 5785.
[108] NechacheR, HarnageaC, LiS, CardenasL, HuangW, ChakrabarttyJ, RoseiF, Nat. Photon. 2015, 9, 61.
[109] K. T. Butler, J. M. Frost, A. Walsh, Energy Environ. Sci. 2015, 8, 838.
[110] J. E. Spanier, V. M. Fridkin, A. M. Rappe, A. R. Akbashev, A. Polemi, Y. Qi, Z. Gu, S. M. Young, C. J. Hawley, D. Imbrenda, G. Xiao, A. L. Bennett-Jackson, C. L. Johnson, Nat. Photon. 2016, 10, 611.
[111] A. Zenkevich, Y. Matveyev, K. Maksimova, R. Gaynutdinov, A. Tolstikhina, V. Fridkin, Phys. Rev. B 2014, 90, 161409.
[112] L. Z. Tan, F. Zheng, S. M. Young, F. Wang, S. Liu, A. M. Rappe, Npj Comput. Mater. 2016, 2, 16026; M. Nakamura, S. Horiuchi, F. Kagawa, N. Ogawa, T. Kurumaji, Y. Tokura, M. Kawasaki, Nat. Commun. 2017, 8, 281.
[113] I. Grinberg, D. V. West, M. Torres, G. Gou, D. M. Stein, L. Wu, G. Chen, E. M. Gallo, A. R. Akbashev, P. K. Davies, J. E. Spanier, A. M. Rappe, Nature 2013, 503, 509.
[114] R. Nechache, C. Harnagea, S. Li, L. Cardenas, W. Huang, J. Chakrabartty, F. Rosei, Nat. Photon. 2014, 9, 61.
[115] D. Cao, C. Wang, F. Zheng, W. Dong, L. Fang, M. Shen, Nano Lett. 2012, 12, 2803.
[116] F. Zheng, Y. Xin, W. Huang, J. Zhang, X. Wang, M. Shen, W. Dong, L. Fang, Y. Bai, X. Shen, J. Hao, J. Mater. Chem. A 2014, 2, 1363.
[117] H. Huang, Nat. Photon. 2010, 4, 134.
[118] M. A. Green, S. P. Bremner, Nat Mater 2017, 16, 23; Q. Gan, F. J. Bartoli, Z. H. Kafafi, Adv. Mater. 2013, 25, 2385; G. H. Carey, A. L. Abdelhady, Z. Ning, S. M. Thon, O. M. Bakr, E. H. Sargent, Chem. Rev. 2015, 115, 12732; Y. Cao, Y. Saygili, A. Ummadisingu, J. Teuscher, J. Luo, N. Pellet, F. Giordano, S. M. Zakeeruddin, J. E. Moser, M. Freitag, A. Hagfeldt, M. Grätzel, Nat. Commun. 2017, 8, 15390.
[119] A. Kojima, K. Teshima, Y. Shirai, T. Miyasaka, J. Am. Chem. Soc. 2009, 131, 6050.

[120] N. K. Noel, S. D. Stranks, A. Abate, C. Wehrenfennig, S. Guarnera, A.-A. Haghighirad, A. Sadhanala, G. E. Eperon, S. K. Pathak, M. B. Johnston, A. Petrozza, L. M. Herz, H. J. Snaith, Energy Environ. Sci. 2014, 7, 3061.
[121] T. M. Brenner, D. A. Egger, L. Kronik, G. Hodes, D. Cahen, Nat. Rev. Mater. 2016, 1, 15007.
[122] S. De Wolf, J. Holovsky, S.-J. Moon, P. Löper, B. Niesen, M. Ledinsky, F.-J. Haug, J.-H. Yum, C. Ballif, J. Phys. Chem. Lett. 2014, 5, 1035.
[123] A. Miyata, A. Mitioglu, P. Plochocka, O. Portugall, J. T.-W. Wang, S. D. Stranks, H. J. Snaith, R. J. Nicholas, Nat. Phys. 2015, 11, 582.
[124] J. Even, L. Pedesseau, J.-M. Jancu, C. Katan, J. Phys. Chem. Lett. 2013, 4, 2999.
[125] Q. Dong, Y. Fang, Y. Shao, P. Mulligan, J. Qiu, L. Cao, J. Huang, Science 2015, 347, 967.
[126] D. Shi, V. Adinolfi, R. Comin, M. Yuan, E. Alarousu, A. Buin, Y. Chen, S. Hoogland, A. Rothenberger, K. Katsiev, Y. Losovyj, X. Zhang, P. A. Dowben, O. F. Mohammed, E. H. Sargent, O. M. Bakr, Science 2015, 347, 519.
[127] Z. Xiao, Q. Dong, C. Bi, Y. Shao, Y. Yuan, J. Huang, Adv. Mater. 2014, 26, 6503.
[128] D. A. Egger, E. Edri, D. Cahen, G. Hodes, J. Phys. Chem. Lett. 2015, 6, 279.
[129] Y. Yuan, J. Chae, Y. Shao, Q. Wang, Z. Xiao, A. Centrone, J. Huang, Adv. Energy Mater. 2015, 5, 1500615.
[130] J. Beilsten-Edmands, G. E. Eperon, R. D. Johnson, H. J. Snaith, P. G. Radaelli, Appl. Phys. Lett. 2015, 106, 173502.
[131] R. Ding, X. Zhang, X. W. Sun, Adv. Func. Mater. 2017, 27, 1702207.
[132] S. Liu, F. Zheng, N. Z. Koocher, H. Takenaka, F. Wang, A. M. Rappe, J. Phys. Chem. Lett. 2015, 6, 693.
[133] J. M. Frost, K. T. Butler, F. Brivio, C. H. Hendon, M. van Schilfgaarde, A. Walsh, Nano Lett. 2014, 14, 2584.
[134] Y. Kutes, L. Ye, Y. Zhou, S. Pang, B. D. Huey, N. P. Padture, J. Phys. Chem. Lett. 2014, 5, 3335.
[135] H. Rohm, T. Leonhard, M. J. Hoffmann, A. Colsmann, Energy Environ. Sci. 2017, 10, 950.
[136] Q. Chen, N. De Marco, Y. Yang, T.-B. Song, C.-C. Chen, H. Zhao, Z. Hong, H. Zhou, Y. Yang, Nano Today 2015, 10, 355.
[137] S. Yakunin, M. Sytnyk, D. Kriegner, S. Shrestha, M. Richter, G. J. Matt, H. Azimi, C. J. Brabec, J. Stangl, M. V. Kovalenko, W. Heiss, Nat. Photon. 2015, 9, 444.
[138] L. Dou, Y. Yang, J. You, Z. Hong, W.-H. Chang, G. Li, Y. Yang, Nat. Commun. 2014, 5, 5404.
[139] Y. Fang, J. Huang, Adv. Mater. 2015, 27, 2804.
[140] W. Pan, H. Wu, J. Luo, Z. Deng, C. Ge, C. Chen, X. Jiang, W.-J. Yin, G. Niu, L. Zhu, L. Yin, Y. Zhou, Q. Xie, X. Ke, M. Sui, J. Tang, Nat. Photon. 2017, 11, 726.
[141] Z.-K. Tan, R. S. Moghaddam, M. L. Lai, P. Docampo, R. Higler, F. Deschler, M. Price, A. Sadhanala, L. M. Pazos, D. Credgington, F. Hanusch, T. Bein, H. J. Snaith, R. H. Friend, Nat. Nanotechnol. 2014, 9, 687; E. Yassitepe, Z. Yang, O. Voznyy, Y. Kim, G. Walters, J. A. Castañeda, P. Kanjanaboos, M. Yuan, X. Gong, F. Fan, J. Pan, S. Hoogland, R. Comin, O. M. Bakr, L. A. Padilha, A. F. Nogueira, E. H. Sargent, Adv. Func. Mater. 2016, 26, 8757; G. Xing, N. Mathews, S. S. Lim, N. Yantara, X. Liu, D. Sabba, M. Grätzel, S. Mhaisalkar, T. C. Sum, Nat. Mater. 2014, 13, 476.
[142] K. Cai, M. Yang, H. Ju, S. Wang, Y. Ji, B. Li, K. W. Edmonds, Y. Sheng, B. Zhang, N. Zhang, S. Liu, H. Zheng, K. Wang, Nat. Mater. 2017, 16, 712; Z. Lin, C. Mei, L. Wei, Z. Sun, S. Wu, H. Huang, S. Zhang, C. Liu, Y. Feng, H. Tian, H. Yang, J. Li, Y. Wang, G. Zhang, Y. Lu, Y. Zhao, Sci. Rep. 2015, 5, 14133.

[143] Y. Y. Hui, X. Liu, W. Jie, N. Y. Chan, J. Hao, Y.-T. Hsu, L.-J. Li, W. Guo, S. P. Lau, ACS Nano 2013, 7, 7126.
[144] Y. Chen, Y. Zhang, L. Zhang, F. Ding, O. G. Schmidt, Nano Energy 2017, 31, 239.
[145] Y. Zhang, Y. Liu, Z. L. Wang, Adv. Mater. 2011, 23, 3004.
[146] Y. Zhang, G. Gao, H. L. W. Chan, J. Dai, Y. Wang, J. Hao, Adv. Mater. 2012, 24, 1729.
[147] Z. Wang, R. Yu, C. Pan, Y. Liu, Y. Ding, Z. L. Wang, Adv. Mater. 2015, 27, 1553.
[148] Y. Zhang, Y. Yang, Z. L. Wang, Energy Environ. Sci. 2012, 5, 6850.
[149] Z. Gao, J. Zhou, Y. Gu, P. Fei, Y. Hao, G. Bao, Z. L. Wang, J. Appl. Phys. 2009, 105, 113707.
[150] Z. L. Wang, Adv. Mater. 2012, 24, 4632.
[151] Z. L. Wang, Nano Today 2010, 5, 540.
[152] C. Pan, M. Chen, R. Yu, Q. Yang, Y. Hu, Y. Zhang, Z. L. Wang, Adv. Mater. 2016, 28, 1535.
[153] X. Han, M. Chen, C. Pan, Z. L. Wang, J. Mater. Chem. C 2016, 4, 11341.
[154] B. R. Judd, Phys. Rev. 1962, 127, 750.
[155] C. K. Jørgensen, B. R. Judd, Mol. Phys. 1964, 8, 281.
[156] S. Tanabe, T. Ohyagi, N. Soga, T. Hanada, Phys. Rev. B 1992, 46, 3305.
[157] Y. Zheng, G.-X. Ni, C.-T. Toh, M.-G. Zeng, S.-T. Chen, K. Yao, B. Özyilmaz, Appl. Phys. Lett. 2009, 94, 163505.
[158] B. Radisavljevic, A. Kis, Nat. Mater. 2013, 12, 815; J. Wang, H. Fang, X. Wang, X. Chen, W. Lu, W. Hu, Small 2017, 13, 1700894.
[159] S. Yuan, Z. Yang, C. Xie, F. Yan, J. Dai, S. P. Lau, H. L. W. Chan, J. Hao, Adv. Mater. 2016, 28, 10048.
[160] H. Xia, J. Phys.: Condens. Matter 2016, 28, 103003.
[161] X. Hong, A. Posadas, K. Zou, C. H. Ahn, J. Zhu, Phys. Rev. Lett. 2009, 102, 136808.
[162] W. Jie, J. Hao, Nanoscale 2014, 6, 6346.
[163] Q. H. Wang, K. Kalantar-Zadeh, A. Kis, J. N. Coleman, M. S. Strano, Nat. Nanotechnol. 2012, 7, 699.
[164] S. Zeng, M.-K. Tsang, C.-F. Chan, K.-L. Wong, J. Hao, Biomater. 2012, 33, 9232; F. Wang, D. Banerjee, Y. Liu, X. Chen, X. Liu, Analyst 2010, 135, 1839.
[165] Y. Zhang, J. Hao, J. Appl. Phys. 2013, 113, 184112.
[166] G. Ding, F. Gao, G. Wu, D. Bao, J. Appl. Phys. 2011, 109, 123101; F. Gao, G. Wu, H. Zhou, D. Bao, J. Appl. Phys. 2009, 106, 126104.
[167] D. Peng, X. Wang, C. Xu, X. Yao, J. Lin, T. Sun, J. Am. Ceram. Soc. 2013, 96, 184.
[168] P. Zhang, M. Shen, L. Fang, F. Zheng, X. Wu, J. Shen, H. Chen, Appl. Phys. Lett. 2008, 92, 222908.
[169] X. Tian, Z. Wu, Y. Jia, J. Chen, R. K. Zheng, Y. Zhang, H. Luo, Appl. Phys. Lett. 2013, 102, 042907.
[170] H. Zou, D. Peng, G. Wu, X. Wang, D. Bao, J. Li, Y. Li, X. Yao, J. Appl. Phys. 2013, 114, 073103.
[171] H. L. Sun, X. Wu, T. H. Chung, K. W. Kwok, Sci. Rep. 2016, 6, 28677.
[172] K. E. Knowles, H. D. Nelson, T. B. Kilburn, D. R. Gamelin, J. Am. Chem. Soc. 2015, 137, 13138.
[173] G. Bai, Y. Zhang, J. Hao, Sci. Rep. 2014, 4, 5724.
[174] X. Wang, C. N. Xu, H. Yamada, K. Nishikubo, X. G. Zheng, Adv. Mater. 2005, 17, 1254.
[175] D. Tu, C.-N. Xu, A. Yoshida, M. Fujihala, J. Hirotsu, X.-G. Zheng, Adv. Mater. 2017, 29, 1606914.
[176] N. Akopian, L. Wang, A. Rastelli, O. G. Schmidt, V. Zwiller, Nat. Photon. 2011, 5, 230.

[177] S. Kumar, R. Trotta, E. Zallo, J. D. Plumhof, P. Atkinson, A. Rastelli, O. G. Schmidt, Appl. Phys. Lett. 2011, 99, 161118.
[178] B. Höfer, J. Zhang, J. Wildmann, E. Zallo, R. Trotta, F. Ding, A. Rastelli, O. G. Schmidt, Appl. Phys. Lett. 2017, 110, 151102.
[179] O. Benson, C. Santori, M. Pelton, Y. Yamamoto, Phys. Rev. Lett. 2000, 84, 2513.
[180] J. E. Avron, G. Bisker, D. Gershoni, N. H. Lindner, E. A. Meirom, R. J. Warburton, Phys. Rev. Lett. 2008, 100, 120501.
[181] F. Ding, R. Singh, J. D. Plumhof, T. Zander, V. Křápek, Y. H. Chen, M. Benyoucef, V. Zwiller, K. Dörr, G. Bester, A. Rastelli, O. G. Schmidt, Phys. Rev. Lett. 2010, 104, 067405.
[182] J. Zhang, J. S. Wildmann, F. Ding, R. Trotta, Y. Huo, E. Zallo, D. Huber, A. Rastelli, O. G. Schmidt, Nat. Commun. 2015, 6, 10067.
[183] R. Singh, G. Bester, Phys. Rev. Lett. 2010, 104, 196803.
[184] J. D. Plumhof, V. Křápek, F. Ding, K. D. Jöns, R. Hafenbrak, P. Klenovský, A. Herklotz, K. Dörr, P. Michler, A. Rastelli, O. G. Schmidt, Phys. Rev. B 2011, 83, 121302.
[185] J. Zhang, F. Ding, E. Zallo, R. Trotta, B. Höfer, L. Han, S. Kumar, Y. Huo, A. Rastelli, O. G. Schmidt, Nano Lett. 2013, 13, 5808.
[186] Q. Yang, W. Wang, S. Xu, Z. L. Wang, Nano Lett. 2011, 11, 4012.
[187] C. Pan, L. Dong, G. Zhu, S. Niu, R. Yu, Q. Yang, Y. Liu, Z. L. Wang, Nat. Photon. 2013, 7, 752.
[188] R. Bao, C. Wang, L. Dong, R. Yu, K. Zhao, Z. L. Wang, C. Pan, Adv. Func. Mater. 2015, 25, 2884.
[189] X. Li, M. Chen, R. Yu, T. Zhang, D. Song, R. Liang, Q. Zhang, S. Cheng, L. Dong, A. Pan, Z. L. Wang, J. Zhu, C. Pan, Adv. Mater. 2015, 27, 4447.
[190] L. Dong, S. Niu, C. Pan, R. Yu, Y. Zhang, Z. L. Wang, Adv. Mater. 2012, 24, 5470.
[191] M. Peng, Y. Liu, A. Yu, Y. Zhang, C. Liu, J. Liu, W. Wu, K. Zhang, X. Shi, J. Kou, J. Zhai, Z. L. Wang, ACS Nano 2016, 10, 1572.
[192] S. C. Rai, K. Wang, Y. Ding, J. K. Marmon, M. Bhatt, Y. Zhang, W. Zhou, Z. L. Wang, ACS Nano 2015, 9, 6419.
[193] Z. Wang, R. Yu, X. Wen, Y. Liu, C. Pan, W. Wu, Z. L. Wang, ACS Nano 2014, 8, 12866.
[194] S. C. Rai, K. Wang, J. Chen, J. K. Marmon, M. Bhatt, S. Wozny, Y. Zhang, W. Zhou, Adv. Electron. Mater. 2015, 1, 1400050.
[195] X. Wang, H. Zhang, R. Yu, L. Dong, D. Peng, A. Zhang, Y. Zhang, H. Liu, C. Pan, Z. L. Wang, Adv. Mater. 2015, 27, 2324.
[196] C. N. Xu, T. Watanabe, M. Akiyama, X. G. Zheng, Appl. Phys. Lett. 1999, 74, 1236.
[197] S. M. Jeong, S. Song, K.-I. Joo, J. Kim, S.-H. Hwang, J. Jeong, H. Kim, Energy Environ. Sci. 2014, 7, 3338.
[198] L. Chen, M.-C. Wong, G. Bai, W. Jie, J. Hao, Nano Energy 2015, 14, 372.
[199] Y. Chen, Y. Zhang, D. Karnaushenko, L. Chen, J. Hao, F. Ding, O. G. Schmidt, Adv. Mater. 2017, 29, 1605165.
[200] M.-C. Wong, L. Chen, M.-K. Tsang, Y. Zhang, J. Hao, Adv. Mater. 2015, 27, 4488.
[201] M.-C. Wong, L. Chen, G. Bai, L.-B. Huang, J. Hao, Adv. Mater. 2017, 1701945.
[202] M. Ichiki, R. Maeda, Y. Morikawa, Y. Mabune, T. Nakada, K. Nonaka, Appl. Phys. Lett. 2004, 84, 395.
[203] M. Qin, K. Yao, Y. C. Liang, Appl. Phys. Lett. 2008, 93, 122904.
[204] M. Ichiki, H. Furue, T. Kobayashi, R. Maeda, Y. Morikawa, T. Nakada, K. Nonaka, Appl. Phys. Lett. 2005, 87, 222903.
[205] J. Zhang, X. Su, M. Shen, Z. Dai, L. Zhang, X. He, W. Cheng, M. Cao, G. Zou, Sci. Rep. 2013, 3, 2109.
[206] J. Seidel, D. Fu, S.-Y. Yang, E. Alarcón-Lladó, J. Wu, R. Ramesh, J. W. Ager, Phys. Rev. Lett. 2011, 107, 126805.

[207] M.-M. Yang, A. Bhatnagar, Z.-D. Luo, M. Alexe, Sci. Rep. 2017, 7, 43070.
[208] M. Lejman, G. Vaudel, I. C. Infante, P. Gemeiner, V. E. Gusev, B. Dkhil, P. Ruello, Nat. Commun. 2014, 5, 4301.
[209] D. S. Rana, I. Kawayama, K. Mavani, K. Takahashi, H. Murakami, M. Tonouchi, Adv. Mater. 2009, 21, 2881.
[210] S. D. Stranks, H. J. Snaith, Nat. Nanotechnol. 2015, 10, 391.
[211] C. D. Bailie, M. G. Christoforo, J. P. Mailoa, A. R. Bowring, E. L. Unger, W. H. Nguyen, J. Burschka, N. Pellet, J. Z. Lee, M. Gratzel, R. Noufi, T. Buonassisi, A. Salleo, M. D. McGehee, Energy Environ. Sci. 2015, 8, 956.
[212] O. Ergen, S. M. Gilbert, T. Pham, S. J. Turner, M. T. Z. Tan, M. A. Worsley, A. Zettl, Nat. Mater. 2017, 16, 522.
[213] S. Y. Leblebici, L. Leppert, Y. Li, S. E. Reyes-Lillo, S. Wickenburg, E. Wong, J. Lee, M. Melli, D. Ziegler, D. K. Angell, D. F. Ogletree, Paul D. Ashby, F. M. Toma, J. B. Neaton, I. D. Sharp, A. Weber-Bargioni, Nat. Energy 2016, 1, 16093.
[214] S. S. Shin, E. J. Yeom, W. S. Yang, S. Hur, M. G. Kim, J. Im, J. Seo, J. H. Noh, S. I. Seok, Science 2017, 356, 167.
[215] W. Wei, Y. Zhang, Q. Xu, H. Wei, Y. Fang, Q. Wang, Y. Deng, T. Li, A. Gruverman, L. Cao, J. Huang, Nat. Photon. 2017, 11, 315.
[216] J. Song, J. Li, X. Li, L. Xu, Y. Dong, H. Zeng, Adv. Mater. 2015, 27, 7162; F. Zhang, H. Zhong, C. Chen, X.-g. Wu, X. Hu, H. Huang, J. Han, B. Zou, Y. Dong, ACS Nano 2015, 9, 4533.
[217] L. Zhang, X. Yang, Q. Jiang, P. Wang, Z. Yin, X. Zhang, H. Tan, Y. Yang, M. Wei, B. R. Sutherland, E. H. Sargent, J. You, Nat. Commun. 2017, 8, 15640.
[218] J. Wang, N. Wang, Y. Jin, J. Si, Z.-K. Tan, H. Du, L. Cheng, X. Dai, S. Bai, H. He, Z. Ye, M. L. Lai, R. H. Friend, W. Huang, Adv. Mater. 2015, 27, 2311.
[219] H. Cho, S.-H. Jeong, M.-H. Park, Y.-H. Kim, C. Wolf, C.-L. Lee, J. H. Heo, A. Sadhanala, N. Myoung, S. Yoo, S. H. Im, R. H. Friend, T.-W. Lee, Science 2015, 350, 1222.
[220] Z. Xiao, R. A. Kerner, L. Zhao, N. L. Tran, K. M. Lee, T.-W. Koh, G. D. Scholes, B. P. Rand, Nat. Photon. 2017, 11, 108.
[221] V. Adinolfi, W. Peng, G. Walters, O. M. Bakr, E. H. Sargent, Adv. Mater. 2018, 30, 1700764.
[222] A. M. A. Leguy, J. M. Frost, A. P. McMahon, V. G. Sakai, W. Kockelmann, C. Law, X. Li, F. Foglia, A. Walsh, B. C. O'Regan, J. Nelson, J. T. Cabral, P. R. F. Barnes, Nat. Commun. 2015, 6, 7124.
[223] M. Coll, A. Gomez, E. Mas-Marza, O. Almora, G. Garcia-Belmonte, M. Campoy-Quiles, J. Bisquert, J. Phys. Chem. Lett. 2015, 6, 1408.
[224] H.-S. Kim, S. K. Kim, B. J. Kim, K.-S. Shin, M. K. Gupta, H. S. Jung, S.-W. Kim, N.-G. Park, J. Phys. Chem. Lett. 2015, 6, 1729.
[225] A. Pecchia, D. Gentilini, D. Rossi, M. Auf der Maur, A. Di Carlo, Nano Lett. 2016, 16, 988.
[226] X. Zhang, M. Zhang, G. Lu, J. Phys. Chem. C 2016, 120, 23969.
[227] F. Bi, S. Markov, R. Wang, Y. Kwok, W. Zhou, L. Liu, X. Zheng, G. Chen, C. Yam, J. Phys. Chem. C 2017, 121, 11151.
[228] P. Wang, J. Zhao, L. Wei, Q. Zhu, S. Xie, J. Liu, X. Meng, J. Li, Nanoscale 2017, 9, 3806.
[229] T.-C. Wei, H.-P. Wang, T.-Y. Li, C.-H. Lin, Y.-H. Hsieh, Y.-H. Chu, J.-H. He, Adv. Mater. 2017, 29, 1701789.
[230] W. Jie, Y. Y. Hui, N. Y. Chan, Y. Zhang, S. P. Lau, J. Hao, J. Phys. Chem. C 2013, 117, 13747.
[231] N. Park, H. Kang, J. Park, Y. Lee, Y. Yun, J.-H. Lee, S.-G. Lee, Y. H. Lee, D. Suh, ACS Nano 2015, 9, 10729.

[232] W. Jie, Y. Yu Hui, Y. Zhang, S. Ping Lau, J. Hao, Appl. Phys. Lett. 2013, 102, 223112.
[233] C. Baeumer, S. P. Rogers, R. Xu, L. W. Martin, M. Shim, Nano Lett. 2013, 13, 1693.
[234] G.-X. Ni, Y. Zheng, S. Bae, C. Y. Tan, O. Kahya, J. Wu, B. H. Hong, K. Yao, B. Özyilmaz, ACS Nano 2012, 6, 3935.
[235] Y. Lee, J. Kwon, E. Hwang, C.-H. Ra, W. J. Yoo, J.-H. Ahn, J. H. Park, J. H. Cho, Adv. Mater. 2015, 27, 41.
[236] T. Georgiou, R. Jalil, B. D. Belle, L. Britnell, R. V. Gorbachev, S. V. Morozov, Y.-J. Kim, A. Gholinia, S. J. Haigh, O. Makarovsky, L. Eaves, L. A. Ponomarenko, A. K. Geim, K. S. Novoselov, A. Mishchenko, Nat. Nanotechnol. 2012, 8, 100; W. J. Yu, Z. Li, H. Zhou, Y. Chen, Y. Wang, Y. Huang, X. Duan, Nat. Mater. 2012, 12, 246; Y. Liu, J. Sheng, H. Wu, Q. He, H.-C. Cheng, M. I. Shakir, Y. Huang, X. Duan, Adv. Mater. 2016, 28, 4120; H. Hlaing, C.-H. Kim, F. Carta, C.-Y. Nam, R. A. Barton, N. Petrone, J. Hone, I. Kymissis, Nano Lett. 2015, 15, 69.
[237] L. Britnell, R. V. Gorbachev, R. Jalil, B. D. Belle, F. Schedin, A. Mishchenko, T. Georgiou, M. I. Katsnelson, L. Eaves, S. V. Morozov, N. M. R. Peres, J. Leist, A. K. Geim, K. S. Novoselov, L. A. Ponomarenko, Science 2012, 335, 947; C.-H. Liu, Y.-C. Chang, T. B. Norris, Z. Zhong, Nat. Nanotechnol. 2014, 9, 273.
[238] H. S. Lee, S.-W. Min, M. K. Park, Y. T. Lee, P. J. Jeon, J. H. Kim, S. Ryu, S. Im, Small 2012, 8, 3111.
[239] C. Ko, Y. Lee, Y. Chen, J. Suh, D. Fu, A. Suslu, S. Lee, J. D. Clarkson, H. S. Choe, S. Tongay, R. Ramesh, J. Wu, Adv. Mater. 2016, 28, 2923.
[240] A. Lipatov, P. Sharma, A. Gruverman, A. Sinitskii, ACS Nano 2015, 9, 8089.
[241] W. Wu, L. Wang, R. Yu, Y. Liu, S.-H. Wei, J. Hone, Z. L. Wang, Adv. Mater. 2016, 28, 8463.
[242] Y. Yang., J. You, Nature 2017, 544, 155.

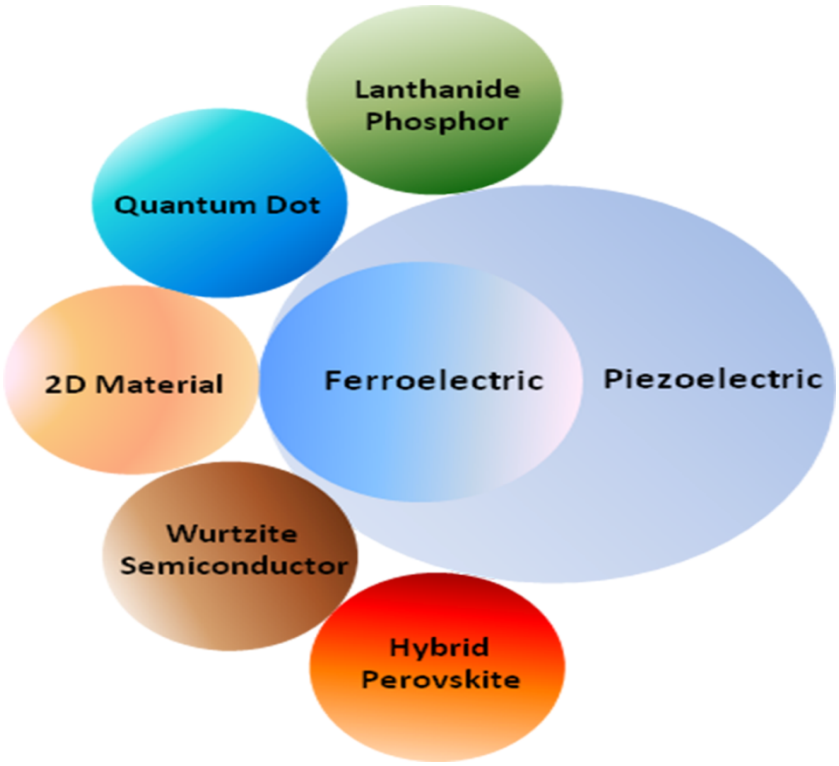

Figure 1. Ferroelectric and piezoelectric effects on advanced optical materials.

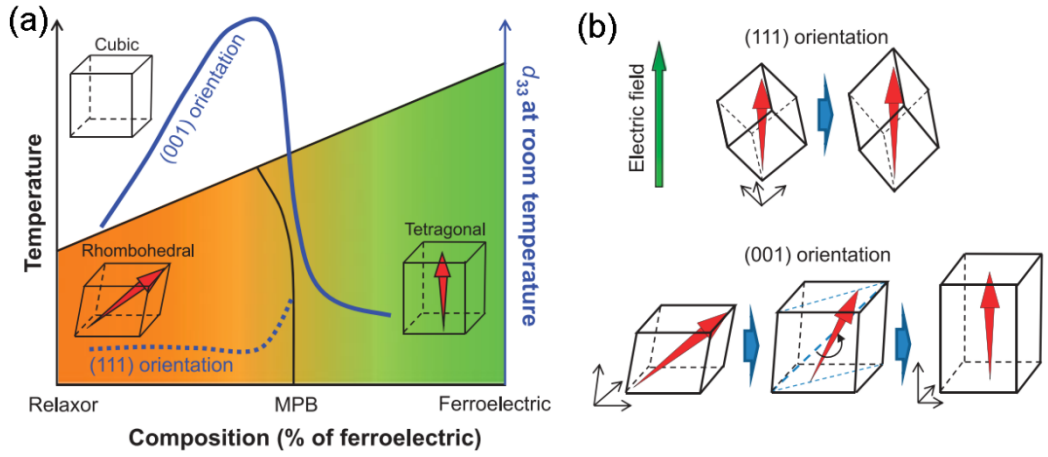

Figure 2. (a) Schematic phase diagram of giant piezoelectric relaxor-ferroelectrics. The solid and dotted blue lines represent the longitudinal piezoelectric coefficients in (001) and (111) relaxor-ferroelectric single crystals, respectively. (b) Schematic illustration of electric-field induced phase transition via polarization rotation from rhombohedral to tetragonal structure as an origin of huge strain level. The red arrow represents the polarization direction. (a) and (b) Reproduced with permission.[34] Copyright 2012, Cambridge University Press.

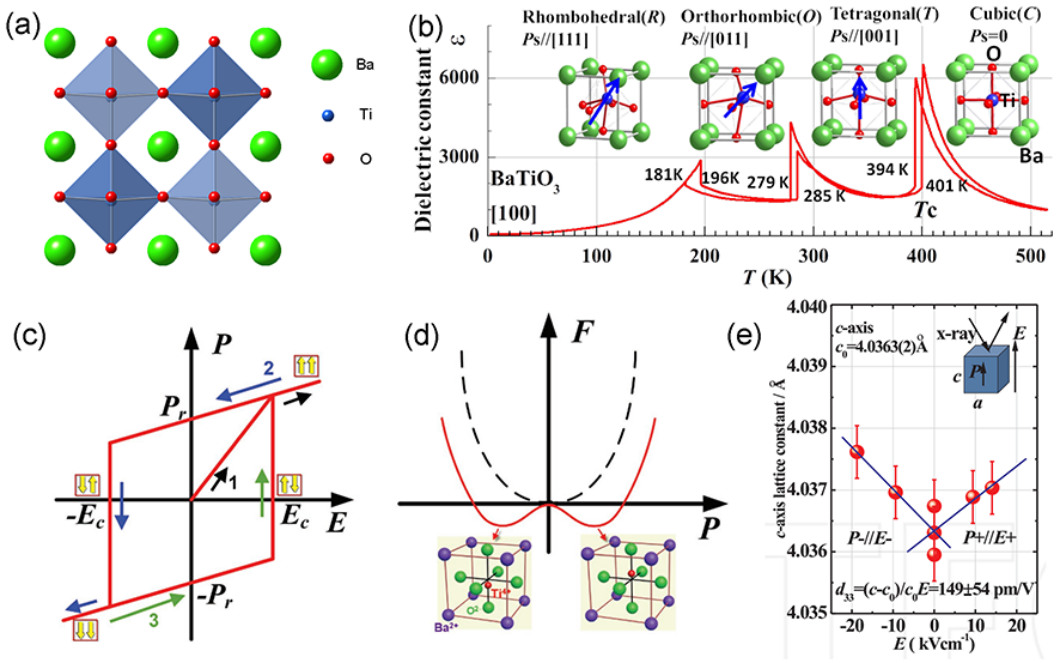

Figure 3. (a) Crystal structure of $BaTiO_3$. (b) Phase transitions of $BaTiO_3$. Reproduced under the term of the CC-BY license.[48] Copyright 2015, Intech. (c) An ideal *P*-*E* loop of ferroelectric materials. P_r and E_c denote the remnant polarization and coercive field, respectively.(d) A qualitative free energy versus polarization curve of $BaTiO_3$. The dashed line illustrates the paraelectric phase materials. (c) and (d) Reproduced with permission.[49] Copyright 2017, Wiley-VCH. (e) Lattice distortion of mono-domain of a $BaTiO_3$ crystal under an electric field. Reproduction with permission.[51] Copyright 2009, IOP Publishing.

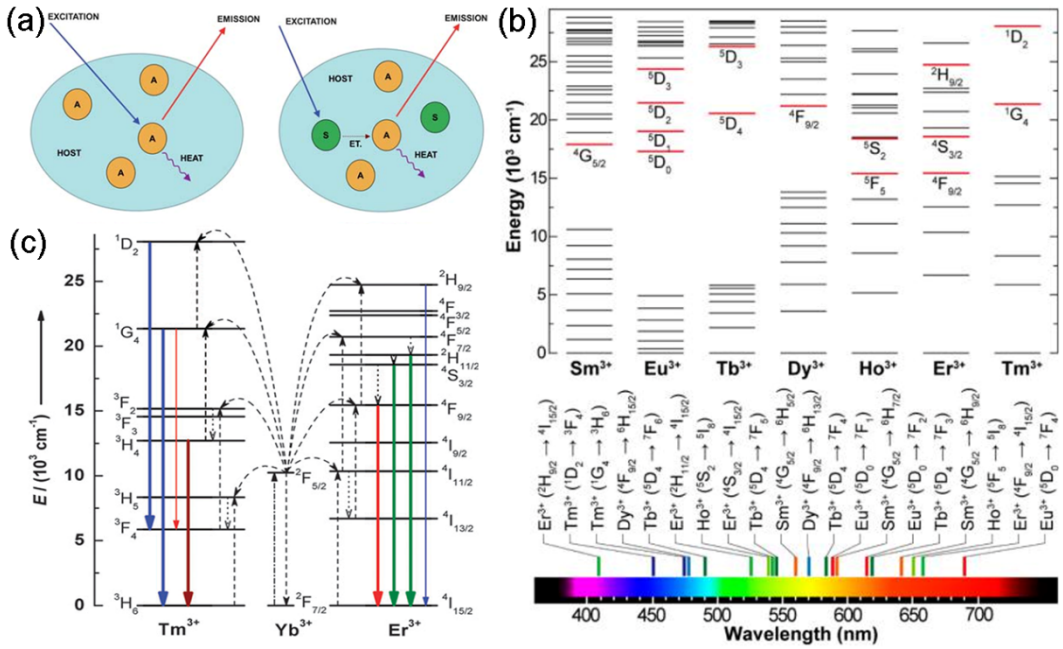

Figure 4. (a) Schematic diagram of metal-ions doped phosphors. Left: activators in the host lattice. Right: energy transfer from a sensitizer to an activator. A: activator; S: sensitizer; ET: energy transfer. Reproduced with permission.[41] Copyright 2013, Royal Society of Chemistry. (b) Energy level diagram of lanthanide ions commonly used. Main luminescent transitions of the lanthaninde ions. Their typical emitting levels are highlighted in red. Reproduced with permission.[55] Copyright 2014, American Chemical Society. (c) Energy transfer mechanisms showing the upconversion processes in Er^{3+}, Tm^{3+}, and Yb^{3+} doped crystals under 980 nm laser excitation. Reproduced with permission.[27] Copyright 2009, Royal Society of Chemistry.

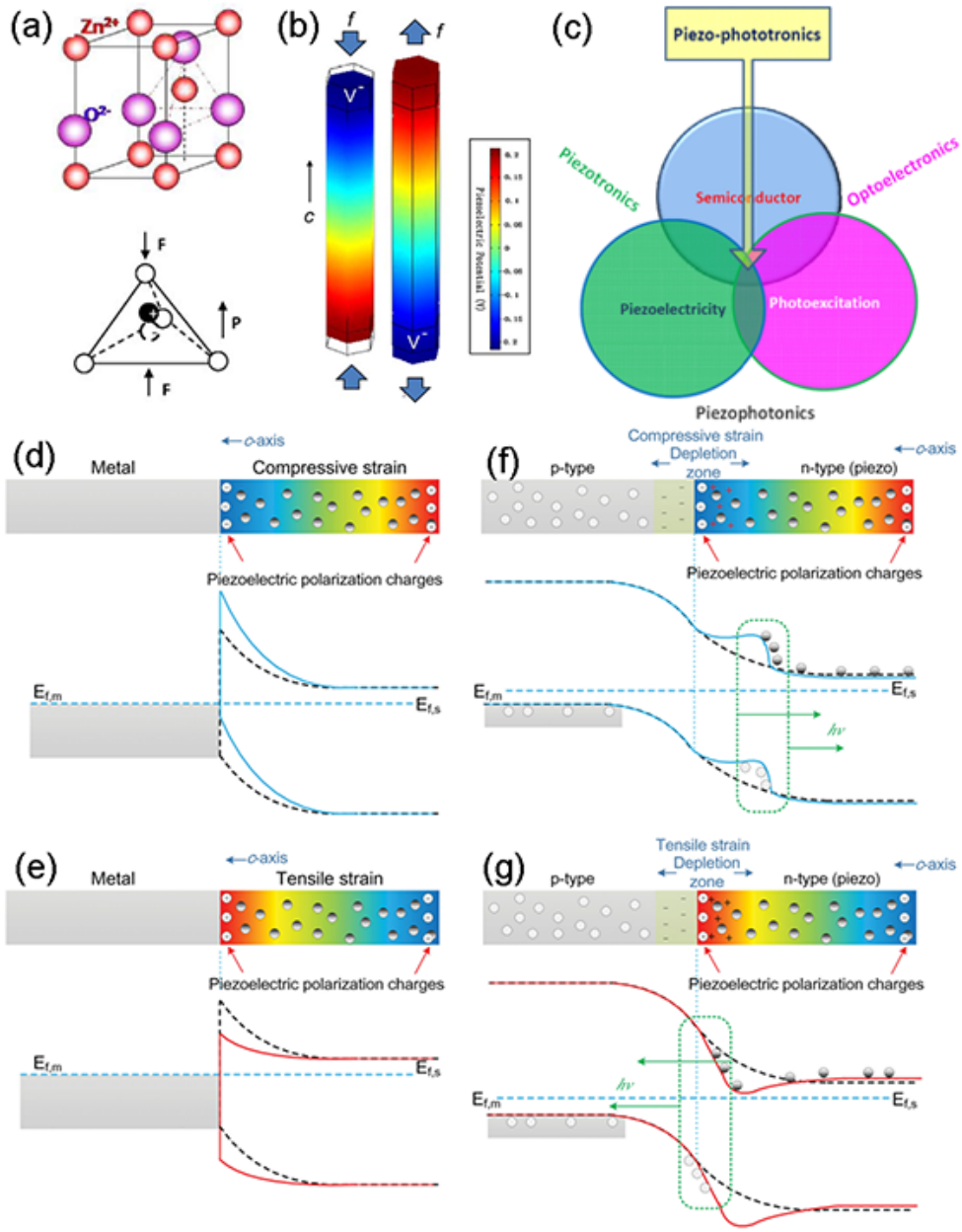

Figure 5. (a) Atomic model of the wurtzite-structured ZnO. (b) Numerical calculation of the piezopotential distribution in a ZnO nanowire under axial strain. The growth direction of the nanowire is *c*-axis. (a) and (b) Reproduced with permission.[149] Copyright 2009, American Institute of Physics. (c) Schematic diagram showing the three-way coupling among piezoelectricity, photoexcitation and semiconductor, which is the basis of piezo-phototronics. Reproduced with permission.[151] Copyright 2010, Elsevier. Schematic of the energy band diagram illustrating the piezo effect on the metal-semiconductor interface and the piezo-phototronic effect on the p-n junction. (d) Negative polarization charges increase the barrier height. (e) Positive polarization charges decrease the barrier height. (f) Negative polarization charges create a bump in the band diagram. (g) Postive polarization charges create a dip in the band diagram. (d)-(g) Reproduced with permission.[150] Copyright 2012, Wiley-VCH.

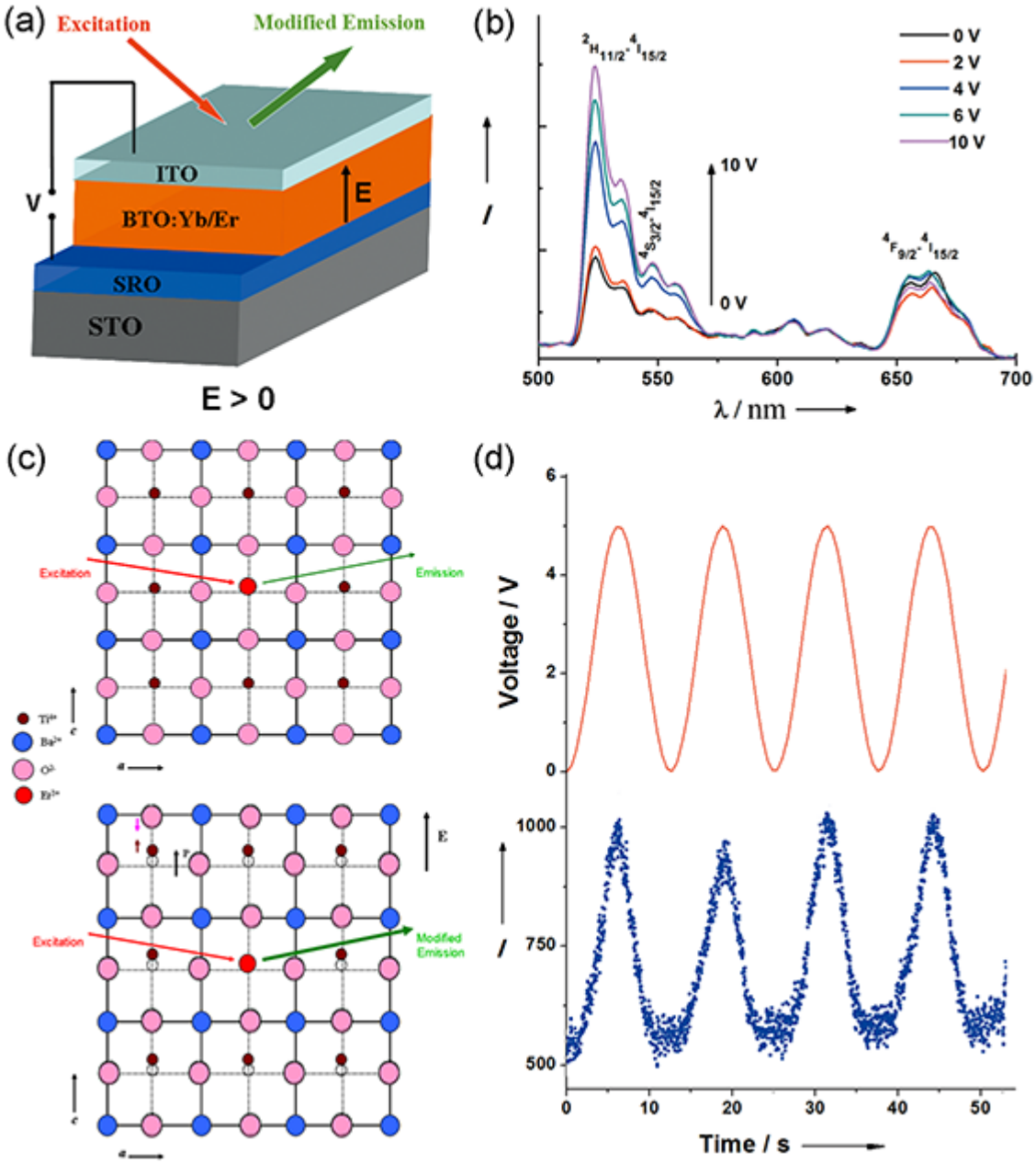

Figure 6. (a) The setup used to measure the upconversion emission of a BTO:Yb/Er thin film under an electric field. (b) The upconversion emission spectra of the BTO:Yb/Er thin film under dc bias voltages ranging from 0 to 10 V. (c) The tetragonal lattice of Er-doped BTO film without and with an external electric field. (d) PL emission at 523 nm as a function of time while the sinusoidal ac electric field is applied to the BTO:Yb/Er film. (a)-(d) Reproduced with permission.[26] Copyright 2011, Wiley-VCH.

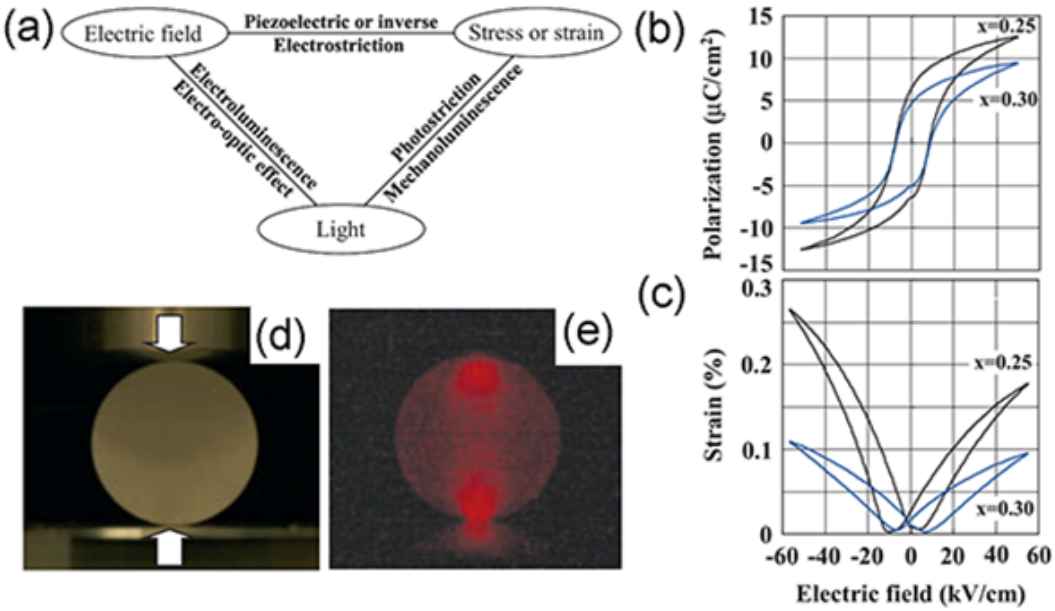

Figure 7. (a) Electro-mechano-optical interation and related effects. (b) Polarization-electric field hysteresis loops and (c) Strain-electric field butterfly curves for samples x = 0.25 and x = 0.30. (d) and (e) Mechanoluminescence images. Red light emission can be observed by naked eyes. (a)-(e) Reproduced with permission.[174] Copyright 2005, Wiley-VCH.

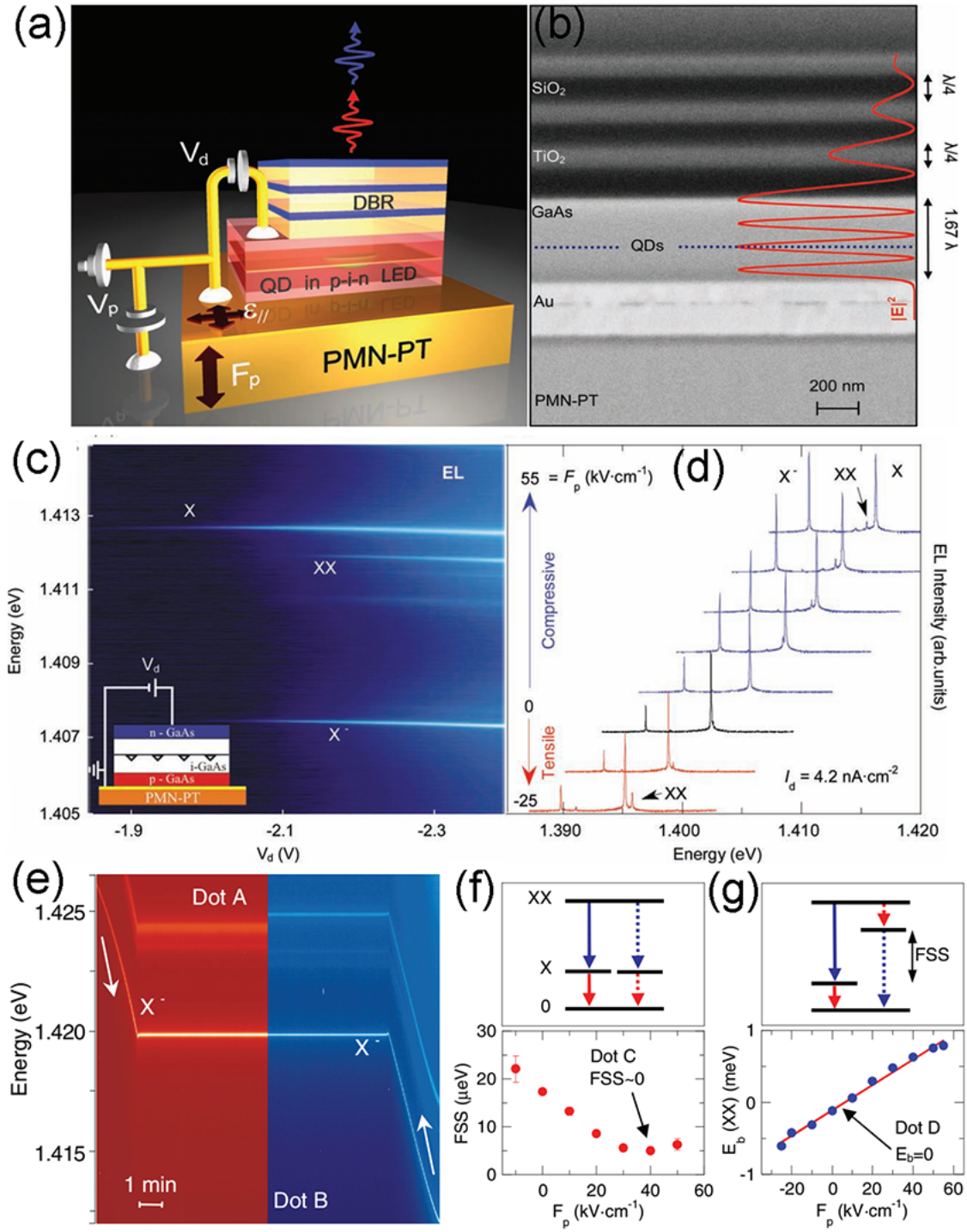

Figure 8. (a) Schematic diagram of a strain-tunable QD resonant-cavity LED. A p-i-n nanomembrane containing QDs is integrated onto PMN-PT, allowing the application of biaxial strain by tuning the voltage V_p. Electrons and holes are electrically injected by setting V_d. The top Distributed Bragg Reflector (DBR) completes a metal-semiconductor-dielectric planar cavity. (b) SEM image of the cross section of the device. (c) Colour-coded micro-electroluminescence (μ-EL) map of a single QD embedded in the tunable-LED at $F_p = 0$ kV/cm. (d) μ-EL spectra of another QD as a function of the electric field on the piezoelectric actuator (F_p), and with a fixed current flowing through the nanomembrane. (e) X^- transitions

from two different QDs are tuned to degeneracy. (f) FSS as a function of F_p for a different QD (Dot C). (g) Biexciton binding energy for another QD (Dot D) as a function of F_p. (a)-(g) Reprodued with permission.[103] Copyright 2012, Wiley-VCH.

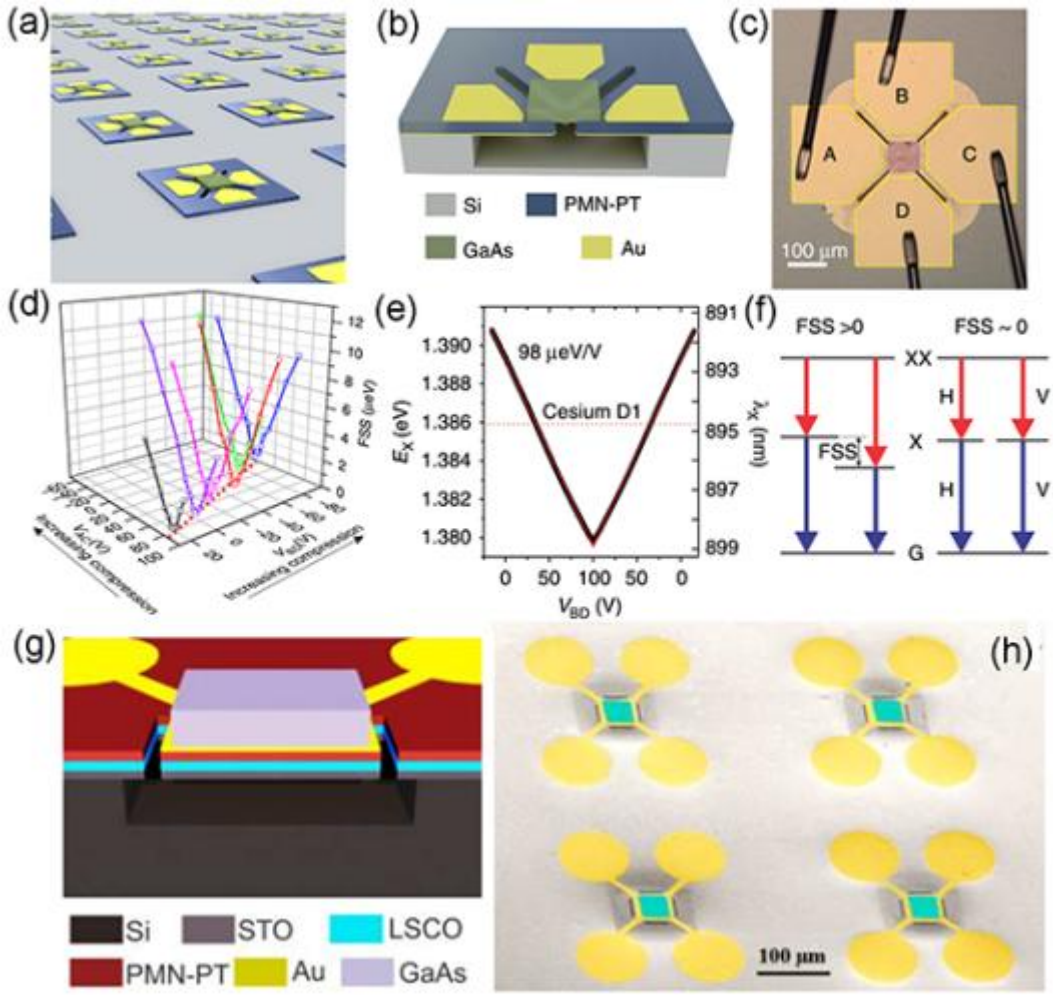

Figure 9. (a) MEMS devices for anisotropic strain engineering of QD-based quantum light source. (b) Schematic of the cross section of a single device. (c) Micrograph showing the zoo-in of a completed device. (d) The changes in the FSS when both V_{BD} and V_{AC} are scanned. (e) Performance of a typical device. The exciton wavelength of a single QD is recorded when the voltage on legs B&D is scanned. The red solid lines show the linear fit. The dashed lines indicate the caesium D_1 absorption line. (f) Illustration of the FSS in a QD. (a)-(f) Reproduced with permission.[106] Copyright 2016, Nature Publishing Group. (g) Schematic of the cross section of a single monolithic MEMS device for the strain engineering of QDs. (h) SEM image of an array of individually addressable PMN-PT microbridge MEMS. The yellow color shows the Au electrodes. The cyan color shows the QD membranes. (g) and (h) Reproduced with permission.[107] Copyright 2016, American Chemical Society.

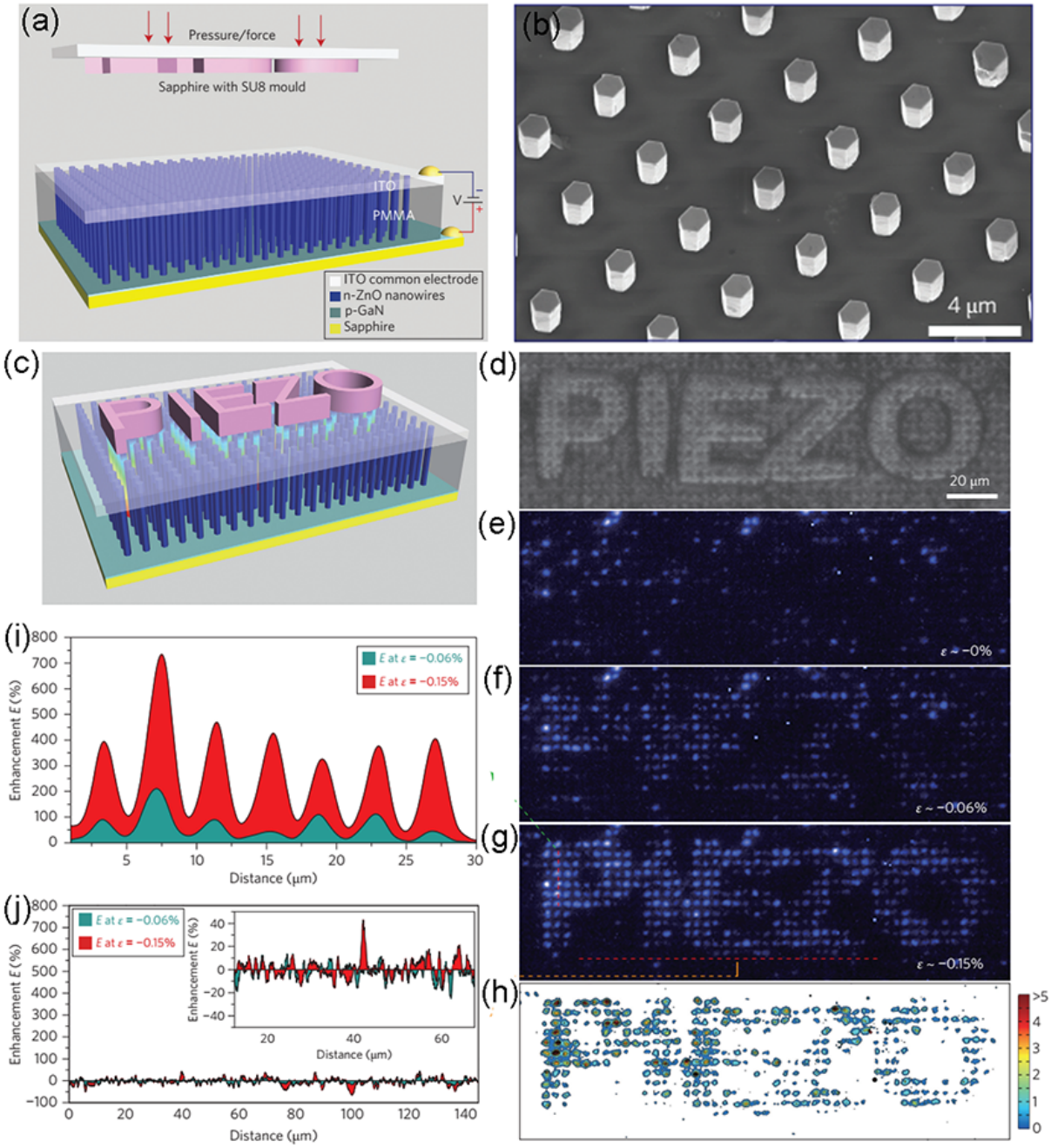

Figure 10. (a) Schematical device design for imaging pressure distribution using the piezo-phototronic effect. (b) SEM image of the as-grown ZnO nanowire arrays on the p-GaN film. (c) Illustration showing the working process of pressure distribution imaging. (d) Optical image of the device with a convex mould on top. (e-g) Electroluminescence images of the device at strains of 0, -0.06% and -0.15%, respectively. (h) Two-dimensional contour map of the enhancement factor *E(x,y)* derived from the LED intensity images shown in e and g. (i-j) Line profile data showing the signal-to-noise ratio of the enhancement factor for typical positions. One on the moulded pattern (vertical pink line, i) and one off the pattern (horizonal

red line, j). (a)-(j) Reproduced with permission.[187] Copyright 2013, Nature Publishing Group.

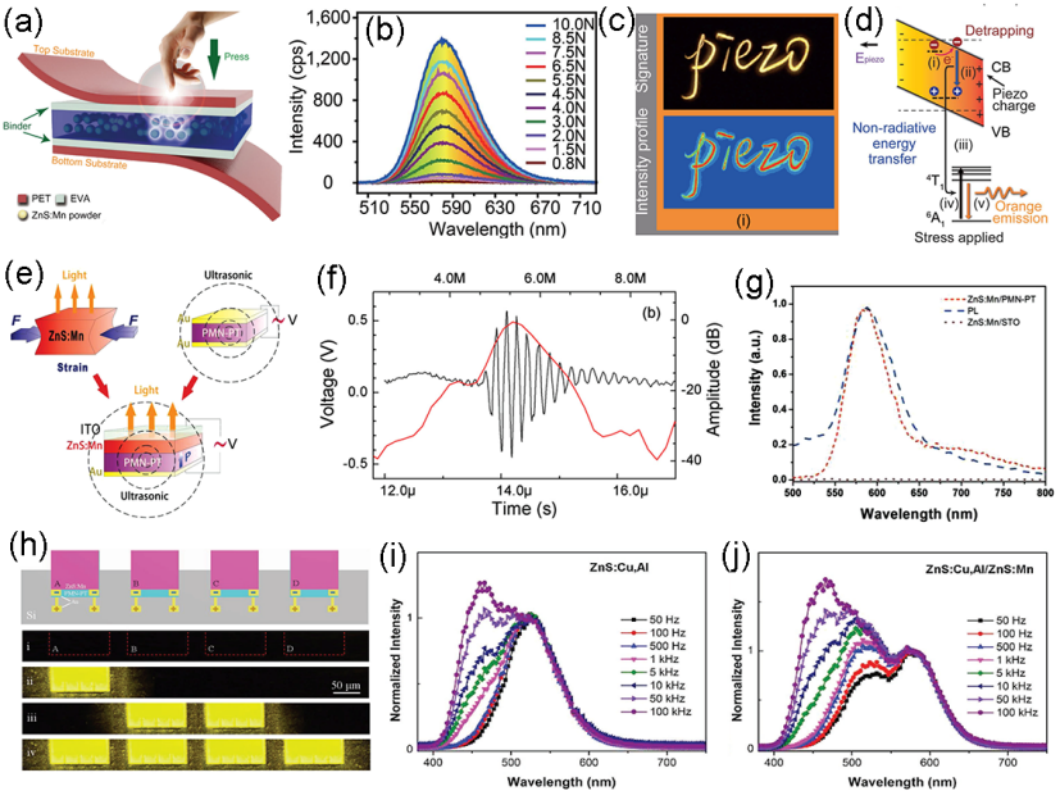

Figure 11. (a) Schematic configuration of pressure-sensor matrix (PSM) for dynamic pressure mapping the ML process. (b) ML spectra under different applied forces. (c) Demonstration of recording the signing habits of signee by PSM devices. (d) The piezophotonic effect initiated the ML process. (a)-(d) Reproduced with permission.[195] Copyright 2015. Wiley-VCH. (e) The setup used to measure the dual-mode light and ultrasound emission of ZnS:Mn/PMN-PT structures. (f) Pulse-echo waveform and frequency spectrum from ZnS:Mn/PMN-PT structures. (g) The luminescence spectra from ZnS:Mn/PMN-PT operating with ac electric field. (e)-(g) Reproduced with permission.[146] Copyright 2012, Wiley-VCH. (h) Visualization of addressable piezophotonic light-emitting devices. Up: Schematic illustration of the prototype device. Low: Demonstration of four representative addressable light emission states. (i) The normalized luminesccence spectra of ZnS:Cu, Al film. (j) The normalized luminescence spectra of ZnS:Cu, Al/ZnS:Mn bilayer film. (h)-(j) Reproduced with permission.[199] Copyright 2017, Wiley-VCH.

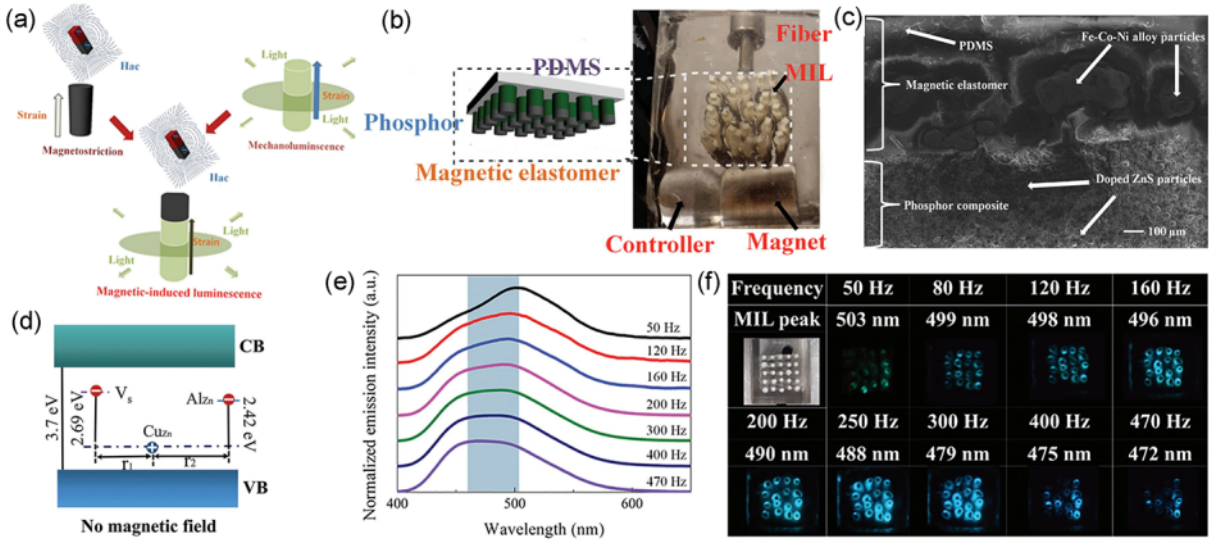

Figure 12. (a) Implementation of magnetic-field-induced luminescence (MIL) effect based strain-mediated magneto-luminescent coupling in two phases of magnetic elastomer and ML phosphors. (b) The setup used for MIL measurements. (c) SEM image taken at the interface of the PDMS composite laminate consisted of Fe-Co-Ni magnetic elastomer and metal-ion-doped ZnS phospors. (a)-(c) Reproduced with permission.[200] Copyright 2015, Wiley-VCH. (d) Illustration of the energy diagram of ZnS:Al,Cu phosphors. (e) Normalized emission intensity of the composite under various magnetic field frequency. (f) Photographs showing from green to blue color variation by changing the modulation frequency. (d)-(f) Reproduced with permission.[201] Copyright 2017, Wiley-VCH.

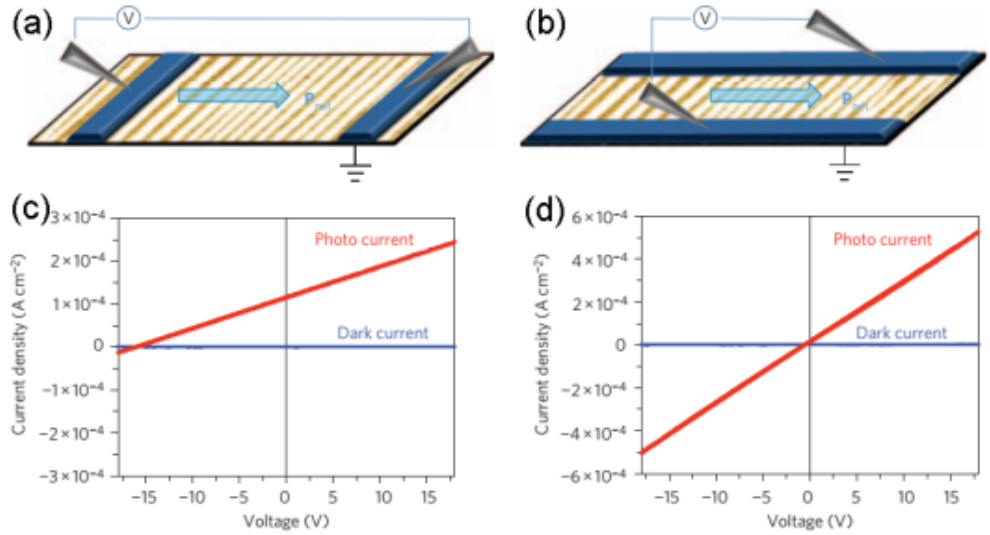

Figure 13. Light and dark I-V measurements. Schematic of the device geometries of the perpendicular (domain wall) (a), and the parallel (domain wall) (b). The corresponding I-V measurements of the devices in (a) and (b) configurations are shown in (c) and (d),

respectively. (a)-(d) Reproduced with permission.[19] Copyright 2010, Nature Publishing Group.

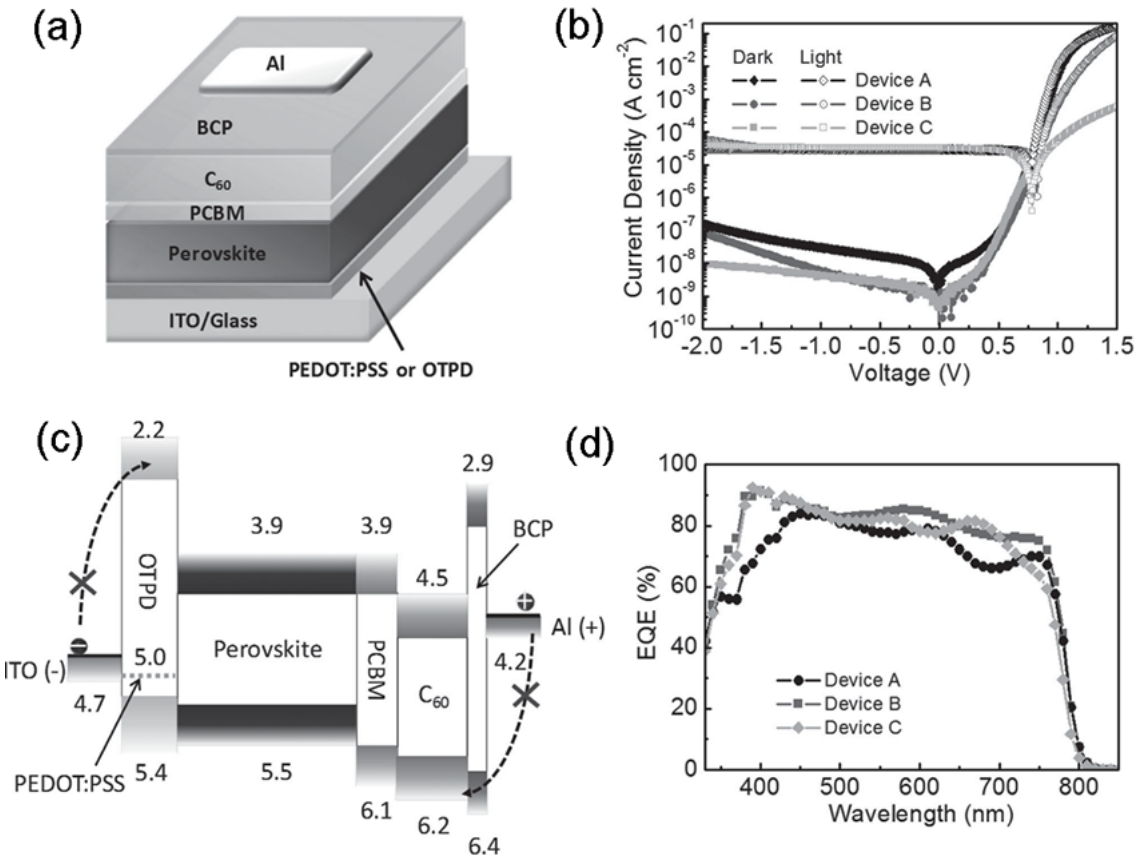

Figure 14. (a) The schematic device structure of perovskite photodetectors. (b) The dark current (solid smbols) and photocurrent density (hollow symbols, under white light ≈ 143 μW cm^{-2}) versus bias curves of various devices. (c) The energy diagram of the perovskite photodetectors. (d) The external quantum efficiency curves of devices at -0.1 V with the incident light modulation frequency of 35 Hz. (a)-(d) Reproduced with permission.[139] Copyright 2015, Wiley-VCH.

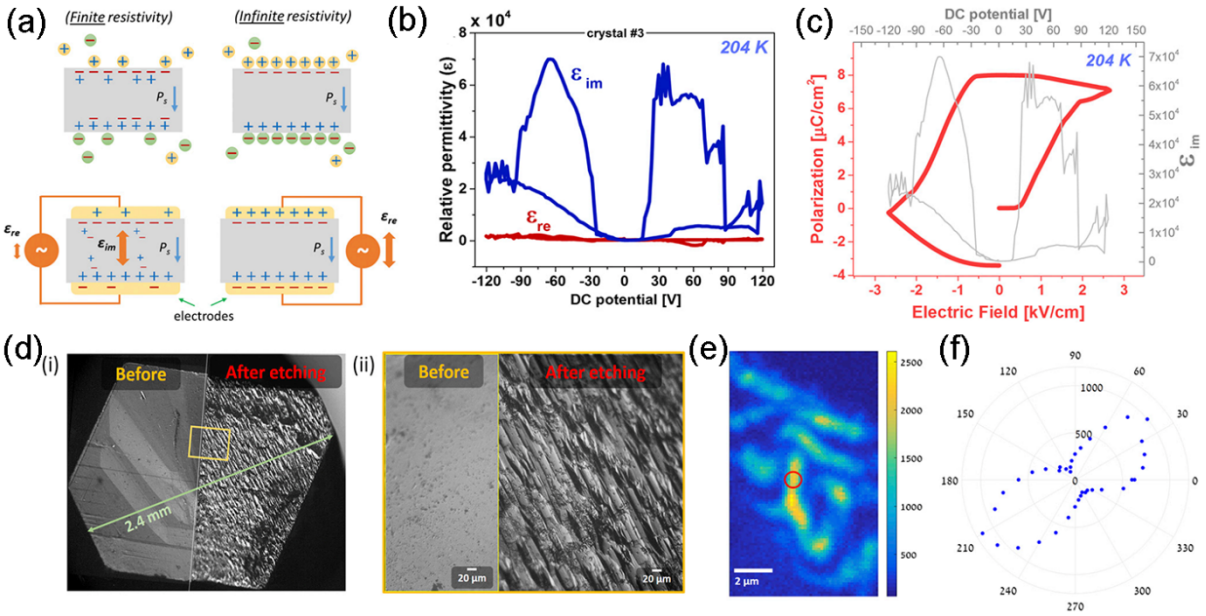

Figure 15. (a) Illustration of a lossy semiconductor and an insulator. Under an applied ac bias, for the lossy semiconductor the dielectric response related to energy dissipation (ε_{im}) will dominate, whereas for the insulator the dielectric response related to energy storage (ε_{re}) will dominate. P_s represents a spontaneous polarization. (b) Dielectric response at 204 K of a $MAPbI_3$ crystal, showing that the imaginary (dissipative) part dominates the dielectric response. (c) *P-E* hysteresis loop obtained from integration of ε_{im} over applied bias electric field. (d) Bright-field image of a $MAPbI_3$ crystal before and after etching. (ii) Magnification of the yellow rectangle marked in (i). (e) A scan of second harmonic generation (SHG) from an area of a crystal fragment. (f) A polar plot of the SHG signal from point in (e). (a)-(f) Reproduced with permission.[25] Copyright 2017, National Academy of Sciences.

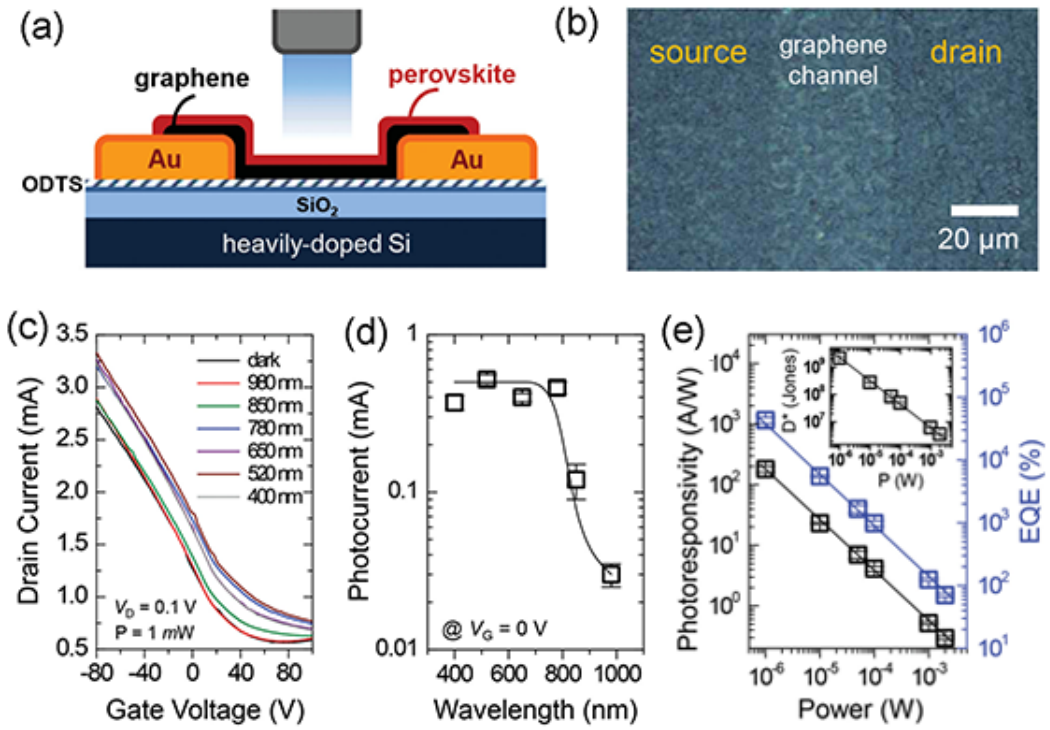

Figure 16. (a) Schematic diagram of the $MAPbI_3$ perovskite-graphene hybrid photodetector. (b) Optical image of the perovskite-graphene hybrid photodetector. (c) Transfer characteristic (V_D = 0.1 V) of the hybrid photodetector under different wavelengths at a fixed incident illumination power of 1 mW. (d) Photocurrents at V_G = 0 V of the hybrid photodetector as a function of the illumination wavelength. (e) Photoresponsivity (R) and effective quantum efficiency (EQE) vs. illumination power. The inset shows the photodetectivity (D*) vs. illumination power. (a)-(e) Reproduced with permission.[235] Copyright 2015, Wiley-VCH.

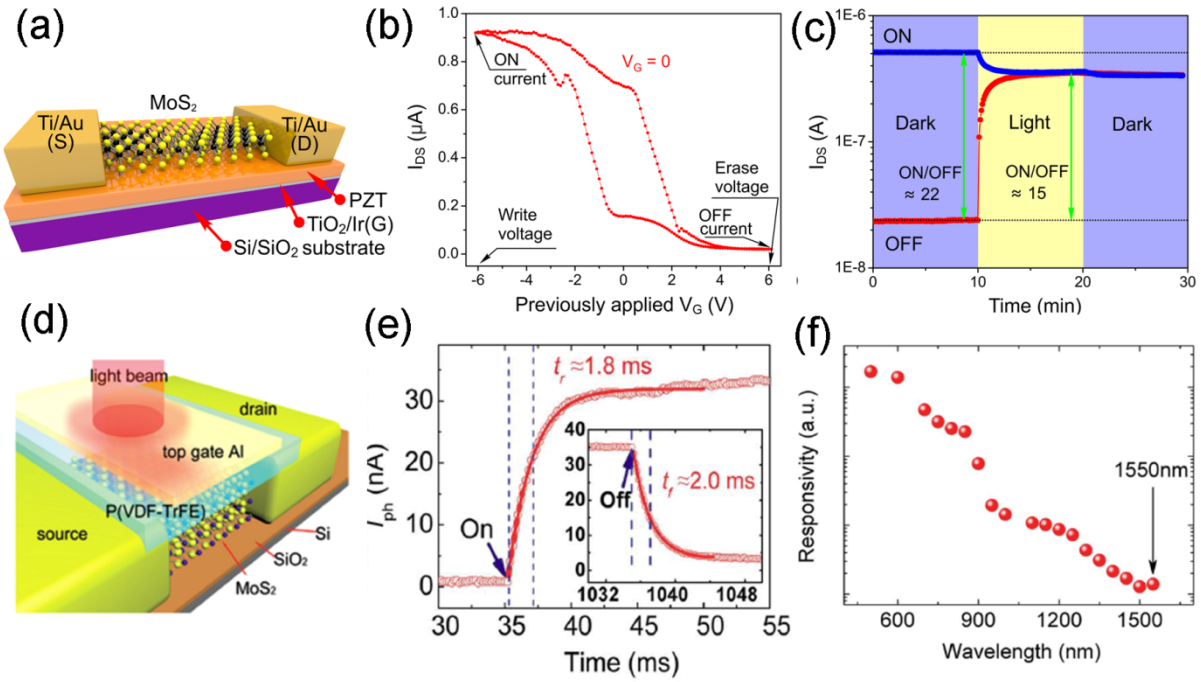

Figure 17. (a) Scheme of a MoS_2-based FeFET. (b) Polarization-dependent hysteresis of electronic transport in a MoS_2-PZT FeFET. (c) Effect of visible light illumination on the data retention characteristics of a MoS_2-PZT FeFET. (a)-(c) Reproduced with permission.[240] Copyright 2015, American Chemical Society. (d) Schematic view of the triple-layer MoS_2 photodetector with monochromatic light beam. (e) The rise and fall of the photocurent and fitted data using exponential functions (recorded by V_{sd} = 100 mV and P = 100 nW). (f) Photoresponsitivity of a polarization-gating triple-layer MoS_2 photodetector as a function of light wavelength from 500 nm to 1550 nm at V_{sd} = 1 V and P = 100 μW under polarization up state. (d)-(f) Reproduced with permission.[14] Copyright 2015, Wiley-VCH.

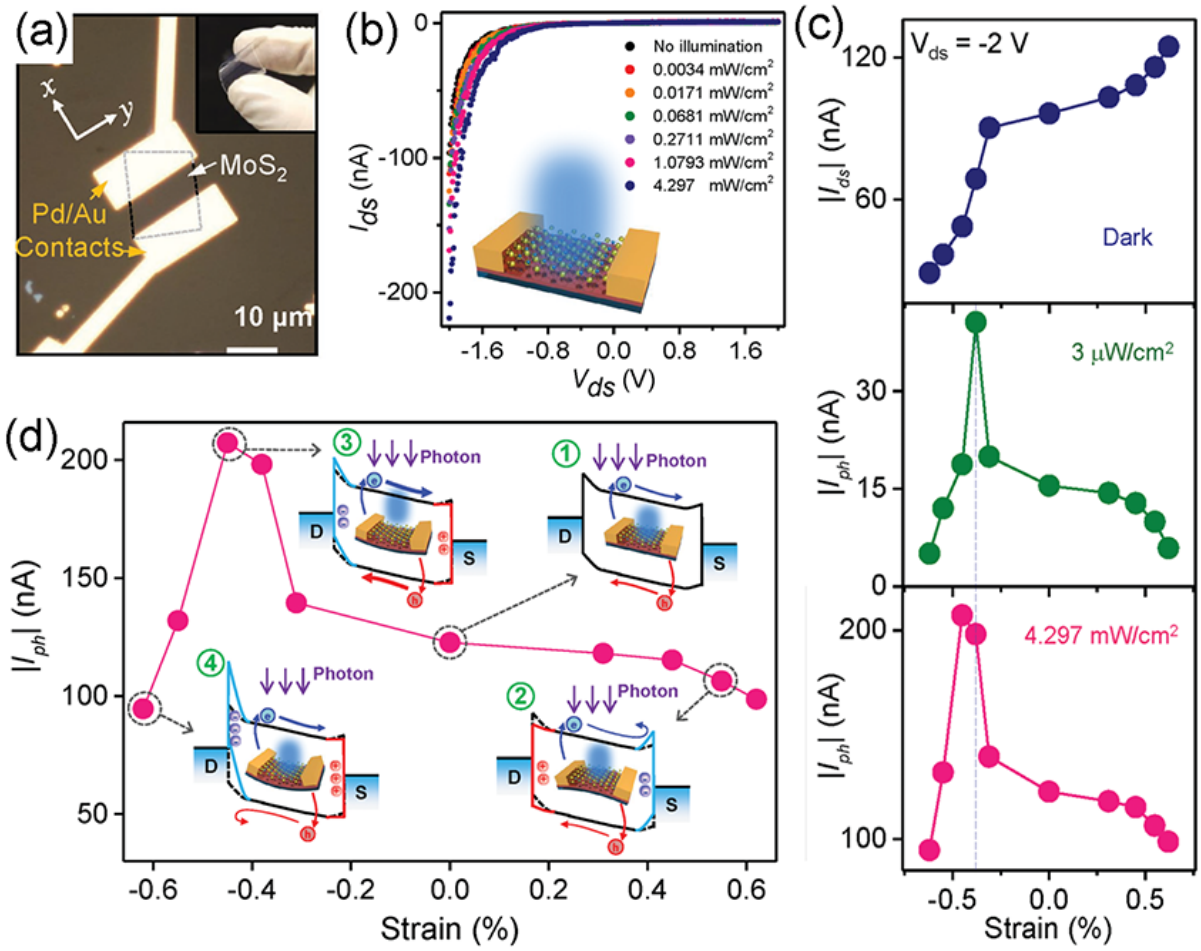

Figure 18. (a) Optical image of the flexible two-terminal single-atomic layer MoS_2 piezo-phototronic photodetector. (b) Electrical transport in single-layer device in the dark and under different illumination intensities (wavelength = 442 nm). (c) Strain dependence of the dark current (top) and photocurrent (middle and bottom) in the device under -2 V drain bias. (d) Working mechanism of piezo-phototronic response in single-layer MoS_2 photodetector. (a)-(d) Reproduced with permission.[241] Copyright 2016, Wiley-VCH.

Yang Zhang obtained his BSc at Huazhong University of Science and Technology (HUST), China. He received his PhD in Applied Physics from the Hong Kong Polytechnic University under the supervision of Prof. Jianhua Hao. He then joined the Leibniz IFW Dresden as an Alexander von Humboldt Fellow. He is currently a Professor of the Institute of Modern Optics in Nankai University. His research interests include luminescent materials for photonic applications, functional thin films and related hybrid devices.

Wenjing Jie obtained her BSc and MSc from University of Electronic Science and Technology of China (UESTC). She received her PhD from the Hong Kong Polytechnic University (PolyU) under the supervision of Prof. Jianhua Hao. Now she works as an associate professor at Sichuan Normal University. Her research interest mainly focuses on 2D materials as well as their electronic and optoelectronic devices.

Jianhua Hao obtained his BSc, MSc and PhD at Huazhong University of Science and Technology, China. After working at Penn State University, USA, University of Guelph, Canada and the University of Hong Kong, Jianhua Hao joined the faculty in the Hong Kong Polytechnic University (PolyU) in 2006. He is currently a Professor and Associate Head of the Department of Applied Physics in PolyU. Jianhua Hao has published about 230 papers indexed by ISI Web of Science. His research interests include metal-ion doped luminescent materials and devices, functional thin-films, two-dimensional materials and heterostructures.

The table of contents entry should be 50–60 words long, and the first phrase should be bold. **Control of the optical processes in emerging materials based on ferroelectric and piezoelectric effects**, has been intensively explored in recent years. These versatile methods can effectively tailor the optical properties of various materials and improve their performance in optoelectronic and photonic devices. Here, an overview of this field, including tuning strategies, mechanisms, and applications is presented.

Keywords ferroelectricity and piezoelectricity, lanthanide-doped phosphors, piezo-phototronics, 2D materials, PMN-PT actuators

Yang Zhang,* Wenjing Jie, Ping Chen, Weiwei Liu, and Jianhua Hao*

Title : Ferroelectric and Piezoelectric Effects on the Optical Process in Advanced Materials and Devices

ToC figure